Structure of Biomolecules Adsorbed at the Hydrophobic Polymer–Solution Interface from Spectroscopic Experiments and Molecular Simulations

by

Shaun Andrew Hall
B.Sc., University of Ottawa, 2006

A dissertation submitted in Partial Fulfillment of the
Requirements for the Degree of

DOCTOR OF PHILOSOPHY

in the Department of Chemistry

University of Victoria

Structure of Biomolecules Adsorbed at the Hydrophobic Polymer–Solution Interface from Spectroscopic Experiments and Molecular Simulations

by

Shaun Andrew Hall
B.Sc., University of Ottawa, 2006

Supervisory Committee

Dr. Dennis K. Hore, Supervisor
(Department of Chemistry)

Dr. Frank van Veggel, Departmental Member
(Department of Chemistry)

Dr. Alexandre G. Brolo, Departmental Member
(Department of Chemistry)

Dr. Andrew Jirasek, Outside Member
(Department of Physics)

Dr. Dennis K. Hore, Supervisor
(Department of Chemistry)

Dr. Frank van Veggel, Departmental Member
(Department of Chemistry)

Dr. Alexandre G. Brolo, Departmental Member
(Department of Chemistry)

Dr. Andrew Jirasek, Outside Member
(Department of Physics)

ABSTRACT

The work herein describes efforts to improve the understanding of the structural and optical properties of molecules adsorbed to polymeric surfaces. The main emphasis was placed upon the determination of molecular orientation of adsorbed molecules by developing methods for extracting structural information from vibrationally-resonant sum frequency generation spectroscopy experiments. Through the comparison of electronic structure calculations to the acquired spectra, orientation distributions were determined for phenylalanine on polystyrene coated fused silica. The initial study was a single example of a method that is applicable to any surface for which the adsorbing species has a completely characterized infrared and Raman spectra. Predicted intensities for the symmetric and antisymmetric CH_2 stretches were compared to their corresponding amplitudes extracted from the acquired spectra. In the second study, the method developed was more general, incorporating the addition of molecular dynamics simulations, which were used to discover various conformations present at the surface, allowing for fits to the acquired spectra to be determined based on the relative populations of these species. This approach was chosen as it is applicable to cases in which the adsorbing species has overlapping spectral features that will not allow for characterization of specific modes. As an example of this, leucine, which possesses highly coupled and overlapping absorptions in its infrared and Raman spectra, adsorption to a polystyrene surface was studied. A high speed Stokes polarimeter based on a dual photoelastic modulator was designed, assembled, and calibrated based on a novel method, capable of measuring the adsorption kinetics of molecules adsorbing to surfaces. The adsorption of bovine serum albumin (BSA) to a polystyrene coated fused silica surface was studied. The configuration of the polarimeter was amenable to the determination of Mueller matrices of equilibrated surfaces with minimal procedural modifications.

Contents

List of Tables

List of Figures

ACKNOWLEDGEMENTS

Dennis Hore – I will be forever grateful that I joined your lab, Doc. There is simply no other person that I have learned more from. Your enthusiasm and passion for your work is just miraculous and I will always seek to emulate that.

Ian and Pauline Hall – You two have seen me through every age and in every light. You loved me as a child, tolerated me as an adolescent, and have respected me as an adult. For this, and so much more, I dedicate this work to you.

Eric Derrah – I love you more than a brother, Dude. I cannot even remember life without a friend like yourself.

Kailash Jena, Paul Covert and Travis Trudeau – The basement can be an unforgiving place, but thanks to labmates such as you it has always been a haven to me.

Jean-Paul Gogniat – That which I can only dream of and draw on paper you cast in metal. It has been a pleasure working with a machinist of your calibre.

Gisella Ramon-Brown – Without knowing you, I would have merely left Victoria with another degree. As it stands, I will leave a more complete man.

NSERC and UVic – Funding

One equal temper of heroic hearts,
Made weak by time and fate, but strong in will
To strive, to seek, to find, and not to yield.

– Tennyson, *Ulysses*

List of Symbols and Definitions

symbol	**definition**	**units**
α	polarizability	C m^2 V^{-1}
$\alpha^{(2)}$	hyperpolarizability	esu
ε	material permittivity	F m^{-1}
ε_0	vacuum permittivity	F m^{-1}
n	real part of complex refractive index	
κ	imaginary part of complex refractive index	
λ	wavelength	m
θ_b	Brewster's angle	deg or rad
χ	electric susceptibility	esu
$\chi^{(2)}$	second order nonlinear susceptibility	esu
ω	angular frequency	rad s^{-1}
Δ	ellipticity	
Ψ	azimuth of polarization ellipse	rad
t	time	s
m	mass	kg
μ	electric dipole moment	C $\cdot$ m
h	Planck's Constant	J $\cdot$ s
Γ	linewidth	cm^{-1}
M	4 x 4 Mueller matrix	
PEM	photo-elastic modulator	
BSA	bovine serum albumin	
BSC	Babinet-Soleil compensator	
SFG	sum frequency generation	
Q	normal mode coordinate	

symbol	**definition**	**units**
MD	molecular dynamics	
D	direction cosine matrix	
PSG	polarization state generator	
PSA	polarization state analyzer	
θ, ϕ, ψ	Euler angles for tilt, azimuth and twist	deg or rad
xyz	actual laboratory coordinate system	
ijk	arbitrary laboratory coordinate system	
abc	actual molecular coordinate system	
lmn	arbitrary molecular coordinate system	
J_n	Bessel function of the nth order	

Chapter 1

Introduction

1.1 Proteins at Surfaces

Protein adsorption to surfaces is, arguably, one of the most important biological processes, impacting upon the initiation of many cellular activities including adhesion, proliferation, differentiation and surface migration [1]. These interactions have been studied heavily over the last 50 years, with the results being compiled in several books [2–4].

In addition to the biological interest in this phenomenon, it is also known that protein adsorption to surfaces affects their physical or chemical properties [5]. What is known is that in addition to the nature of the protein itself, the chemistry and topography of the surface have a great effect upon the adsorbed geometry [6–8]. Ultimately, controlling the surface structure and composition of the interface in any study of protein adsorption is vitally important, as it can affect the hydrophobicity and surface chemistry, and in turn the interactions between the protein and the surface [8].

As can be expected from this information, the interaction between proteins and surfaces is heavily dependent upon the structure and stability of the protein itself, which depends upon the composition of the protein as well as the environment in which it exists [9, 10]. The immediate interfacial region between the solution and the polymer surface is of great interest as the interaction between the protein and the surface groups of the polymer can induce a change in the secondary and tertiary structure of the protein, resulting in a biological response [11]. This change in the overall conformation and chemical properties of the adsorbed protein is directly related to the structure of the protein present at the interface [7]. These changes are generally more pronounced in the case of hydrophobic surfaces where, once a protein has unfolded, it can then maximize hydrophobic interactions with the surface. These conformational changes may result in irreversible protein structural changes (denaturing) [12, 13], or in an unforeseen reaction with their environment. The control of these effects would, therefore, be of great importance to the various growing areas of research that depend upon the control of surface interactions of proteins, their components, or other biomolecules.

Research into these phenomena is driven by the relevance of protein-surface interactions to various medical and industrial processes. From a medical standpoint, the interaction of the human body with various implants is important and it is known that the first step in the biological response to an implant is the formation of a protein layer [6]. The necessity in these systems is that whatever the composition of the implant, in addition to whatever surface modifications may have been made to it, must be haemocompatible [14, 15] and must prevent bacterial adhesion [16]. A very good review outlining the various surface treatments for the improvement of the biocompatibility of polymers has been published [17]. Failure to succeed in creating both haemocompatible and bacteria resistant polymer coatings could result in the body rejecting the implant. As such, a great deal of research has been done into the development of polymer coatings that maximize the biocompatibility of implants [16, 17]. In these studies, focus is placed upon the chemical modification of the polymeric coatings used in implants to reduce bacterial adhesion, thrombogenecity, protein and haemocyte adhesion, while improving chemical inertness, degradation resistance and hardness. A fine review of the general concepts and basic understanding of the biocompatibility of various materials has been created [18]. Generally, the procedures outlined by these reviews for the maximization of the biocompatibilty of polymers involve the incorporation of oligopeptides, saccharide, and oligosaccharide based receptors into the polymer, either by physical or chemical means.

Aside from the previously mentioned medical examples, more general aspects of polymer science are also extremely relevant to these studies, as is evidenced in the study of tailoring the structure of various polymers with the intention of controlling protein adsorption [8]. Certain studies have focused upon the interaction of proteins with polymeric surfaces, and have discovered that conformational changes can be induced upon adsorption to small polymer particles, specifically for human albumin, fibrinogen and immunoglobin [19], that grafted polymer layers can be used to inhibit the adsorption of proteins [20], and that phospholipid containing polymer layers adsorb less proteins from solution than other polymers at the same time as allowing them to maintain their original conformation. Additionally, interesting work regarding the theoretical underpinnings of adsorption to grafted polymer layers has been undertaken [21]. This work focused upon the effect of grafted polymer chain length upon the inhibition of adsorption, noting that the longer the grafts were the greater the effective inhibition. It was postulated that the structure of the layer and its overall deformation upon the adsorption of a protein were the determining factors in inhibiting adsorption.

Related to the study of polymer coatings, the field of chromatography has also heavily influenced the field of protein adsorption, focusing on the separation of protein fractions through the development of various polymeric separation phases [17, 21–26]. A useful process discovered in the development of protein chromatography regarding the purification of proteins involves the addition of amino acids to samples prior to separation. This improves osmotic pressure and certain amino acids, such as arginine, are known to prevent the agglomeration of proteins in the sample, improving activity and thus separation [27]. While a great deal of work has been done in this field, resulting in a wide variety of new packing materials for the separation of proteins [28, 29], and this has, in turn, resulted in the utility of protein chromatography as a useful tool for the study of proteomics [30], the majority of this field is focused upon the efficacy of separation methods and not necessarily the fundamental interactions that are the basis for the protein-surface interaction upon which protein chromatography depends.

One such process of interest to marine industrial processes is that of biofouling, and the corresponding necessity for the study and development of anti-biofouling coatings. Biofouling has been studied primarily from the standpoint of marine organisms, such as molluscs, that require an appropriate attachment to a surface in order to properly function. The necessity for these animals is that they kill any other organisms or remove any previous films that would interfere with their natural ability to do so. The relevance being that many marine industrial processes are themselves hindered by the production of biofilms by various animals. The interaction of various molecules adsorbed at marine surfaces and the disruption of these biofilms present there is therefore of great interest [31].

The control of interactions between proteins and surfaces is also of great importance to the growing research arenas of biosensor development [32–34] and drug delivery systems [35–37]. Specifically, there has been a great deal of focus upon the immobilization of proteins upon surfaces for the purposes of developing these systems [38]. It is necessary to decide upon the most appropriate method of adsorbing proteins, whether it be physical immobilization, such as from electrostatics, or covalent immobilization through a specific side chain of the protein of interest while avoiding nonspecific binding. Once attached at a high enough concentration they can form biochips capable of working as diagnostic tools using a very small sample volume, making it a very attractive developing technology.

What is important to note here is that, while the study of protein adsorption has been underway for the better portion of a century, it has had its roots in the various applications previously outlined, and not necessarily upon the study of the specific causes of protein adsorption. This is, primarily, due to the complicated nature of protein adsorption. In order to simplify the problem at hand, it is often useful to look at systems that can model certain portions of a protein, such as smaller peptides, or of their individual components, amino acids.

1.2 Model Systems for the Study of Proteins at Surfaces

While the study of protein adsorption to surfaces is important unto itself, it is complicated by several factors. Proteins are large biomacromolecules, composed of several regions of considerably different physical and chemical properties. There is an inherent difficulty in analyzing their interactions with surfaces directly, as it is hard to differentiate between protein-surface and protein-solvent interactions. These various interactions are apparent in Figure 1.1, in which one can note the variety of protein-solvent interactions along with the regions of different chemical composition of the protein. Specifically, there are regions of net positive and negative charges along with large hydrophobic regions. The surface with which the protein is interacting also possesses regions of different chemical composition, adding to the complexity of this interaction. The possibility for such varied interactions between a protein and a surface highlights another interesting point regarding protein adsorption: the correlation between their composition and their chemical properties. The advances in the study of the fields mentioned previously have focused upon processes based on protein-surface interactions and not the cause of these interactions. That being said, these studies have led to several advances in our understanding of protein adsorption, but the basic atomic and molecular factors governing the interactions between the proteins and the surfaces are still not well understood.

Proteins are composed of amino acids, polymerically linked through the reaction of the carboxylic acid of one amino acid with the amino group on another. With only twenty common, natural amino acids, the endless variety of proteins that exist in the biosphere can be formed. It is also known that the amino acid composition does affect the protein adsorption [39,40], although the ability to predict adsorption characteristics based on amino acid composition is limited. At an intermediate size range between individual amino acids and complete proteins exist peptides. These oligomers, composed of a small number of individual amino acids, can be used to model a specific region of a protein, such as a binding motif or an active site. As such, it is important to study both the adsorption of

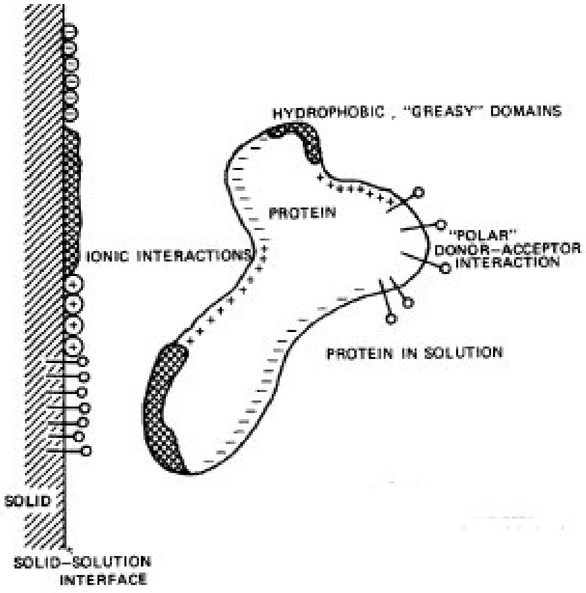

Figure 1.1: Image adapted from Ref 18 depicting a generalized protein adsorbed to a well characterized surface. What is important to note from this image is the variety of chemical and physical interactions present between the protein and the surface, among the different domains of the protein as well as those present between the protein and the solution.

amino acids and peptides to surfaces themselves, as they can yield information relevant to the basic causes of protein adsorption, which in turn would be important to the previously mentioned areas of research dependent upon protein adsorption.

The usefulness of studying peptides as a model for protein systems is apparent upon perusing the literature. They have served very well as model systems, allowing for the study of substrate specificity of binding for various polymers [41], for the formation of peptide coated surfaces [42] for further use in the chemical modification of other adsorbates, and to study the effect of ionic strength upon peptide adsorption [43]. All of these studies can provide insight into similar mechanisms in protein adsorption and the various solvent effects that can alter that process. The most important thing to be noted for peptide studies is that by approaching the problem in a diligent fashion it is still possible to differentiate between the various forces at play, such as those of solvation, peptide-surface interactions and interactions between the individual amino acids [44]. Due to the overall size of proteins, the separation between these effects is normally not possible, making peptides an excellent model system. Another very useful function of their smaller size is the fact that they are amenable to computational studies. Various studies have used this to their advantage [45, 46] to model the various interactions between the peptide and the surfaces of interest.

Taking the simplification of the protein system one step further we come to the study of their basic components: amino acids. Where peptide adsorption normally focuses upon polymeric interfaces, amino acid adsorption has been studied extensively on mineral surfaces, such as quartz [47–51], zeolites [52], titania [53, 54], and graphite [55]. The reason for the emphasis of adsorption of amino acids to common inorganic materials is based upon Bernal's hypothesis, which postulates that surface catalyzed reactions resulted in the formation of prebiotic precursors to proteins and other biomolecules. The research in this field has shown that l-amino acids are more readily adsorbed at these inorganic surfaces than d-amino acids [56], that amino acids adsorb to these surfaces via electrostatic interactions, covalent bond formation, or hydrogen bonding [57] and their adsorption depends upon pH [58]. While research continues in this field, the majority of the interest in protein adsorption is based on their interaction with polymeric surfaces, which have very different properties than inorganic minerals. Frequently, the adsorption of amino acids to polymeric surfaces is studied in order to determine their response to various chromatographic materials such as polystyrene [59] or octadecyl silica [60]. This is logical, as amino acids generally require purification in order to obtain single isomer samples [61].

Throughout this work, emphasis will be placed upon the study of the adsorption of amino acids. Their chemical and spectroscopic simplicity is vital for various reasons that will be explained in detail in Chapters 2 and 3. Through the exploitation of this simplicity it is hoped that more general methods for the determination of the adsorbed surface structure of larger molecules, such as peptides and proteins, can be developed.

1.3 Experimental Methods

In order to study molecules at surfaces, there are a number of requirements for any technique to fulfill. First, the method must be surface specific, focusing exclusively on the interfacial region of interest. Provided that requirement is satisfied, there is a necessity to have some portion of the molecule that can be probed uniquely or some other physical response that can be measured. Specificially for biomolecules, another requirement exists, and that is for the experiment to be performed at pertinent solid-liquid interfaces, thus allowing for comparison to biological systems.

1.3.1 Nonlinear Optical Methods

While other methods provide valuable insight into one or more factors contributing to the adsorption process, they do possess inherent difficulties in achieving enough surface specificity for the *in situ* studies. In order to be uniquely surface specific, it is necessary to utilize a technique that completely ignores the bulk phase and only responds to the interfacial region. To this end, it is necessary to employ certain nonlinear optical techniques. The theory regarding the interaction of light near the boundaries of nonlinear media in basic terms, relating to the solutions to Maxwell's equations, has been explained in detail in the literature [62,63]. The historical development of the use of nonlinear optics for the purposes of studying interactions at surfaces and interfaces has been reviewed [64,65], remarking on the major developments from the development of the ruby laser, followed by the work of the Franken group in 1961, in which they first demonstrated second harmonic and sum frequency generation in quartz crystals [66] to the original work based on the study of surfaces by Bloemenberg [62,67–69].

Aside from the history, however, it is important to discuss the technical aspects of the experiments used in this work and to expand upon the general theory of nonlinear optics and how it relates to the study of molecules at surfaces. In the presence of large electric fields, the proportionality of the induced dipole moment, μ, and the polarization, $\mathbf{P}$, upon the applied electric field breaks down, and higher order terms begin to have an appreciable effect.

$$\mu = \mu_0 + \alpha\mathbf{E} + \alpha^{(2)}\mathbf{E}^2 + \alpha^{(3)}\mathbf{E}^3 + ... \tag{1.1}$$

$$\mathbf{P} = \varepsilon_0 \left(\chi^{(1)}\mathbf{E} + \chi^{(2)}\mathbf{E}^2 + \chi^{(3)}\mathbf{E}^3 + ...\right) \tag{1.2}$$

As can be noted in Equation 1.2, the overall induced polarization involves contributions from higher order susceptibility terms. The second-order nonlinear optical techniques are naturally selective of surface structures since they require a lack of centrosymmetry to produce signal; this symmetry requirement cannot be satisfied by molecules that are tumbling in solution. This useful trait is due to the nature of the second order susceptibility terms. Specifically, the second order susceptibility, $\chi^{(2)}$, is a rank-three tensor, composed of 27 elements that relate the macroscopic induced polarization to the microscopic responses of molecules at the surface. In the case of being in a centrosymmetric environment, it is known that all directions are equivalent and the value of $\chi^{(2)}$ must be the same in both positive and negative directions.

$$\chi^{(2)}_{ijk} = \chi^{(2)}_{-i-j-k} \tag{1.3}$$

In addition to this equality for the second order nonlinear susceptibility it possesses another interesting property. It is due to the fact that it is a third-rank tensor that this changing of all the signs of the indices is also equivalent to reversing the entire axis system, and therefore $\chi^{(2)}$ must reverse its sign, which is expressed as

$$\chi^{(2)}_{ijk} = -\chi^{(2)}_{ijk} \tag{1.4}$$

The only way to simultaneously satisfy Equations 1.3 and 1.4, is for $\chi^{(2)}$ to be equal to 0. Thus, for a centrosymmetric environment, the response of the system to the application of a large electric field is entirely without contribution from terms dependent upon the second order nonlinear susceptibility. Since Equations 1.3 and 1.4 do not hold true for a non centrosymmetric system, such as the interface between two materials, $\chi^{(2)}$ is nonzero, thus allowing for nonlinear methods dependent upon it to focus exclusively upon the interfacial region.

In order to discuss the different methods arising from experiments dependent upon $\chi^{(2)}$, it is necessary to imagine two separate laser beams.

$$\mathbf{E} = \mathbf{E}_1 \cos(\omega_1 t) + \mathbf{E}_2 \cos(\omega_2 t) \tag{1.5}$$

Should these two beams impact upon an interfacial region, wherein $\chi^{(2)}$ is nonzero, coherent in both time and space, they can interact with one another resulting in several different nonlinear optical processes.

$$\mathbf{P}^{(2)} = \varepsilon_0 \chi^{(2)} \left(\mathbf{E}_1 \cos(\omega_1 t) + \mathbf{E}_2 \cos(\omega_2 t)\right)^2 \tag{1.6}$$

If this equation were to be expanded and rearranged so as to collect similar terms, four different processes can be described through the interaction of these two incident electric fields.

$$\mathbf{E}_1^2 + \mathbf{E}_2^2 \tag{1.7}$$

$$\mathbf{E}_1^2 \cos(2\omega_1 t) + \mathbf{E}_2^2 \cos(2\omega_2 t) \tag{1.8}$$

$$\frac{1}{2}\mathbf{E}_1 \mathbf{E}_2 \cos(\omega_1 - \omega_2) \tag{1.9}$$

$$\frac{1}{2}\mathbf{E}_1 \mathbf{E}_2 \cos(\omega_1 + \omega_2) \tag{1.10}$$

We can note a frequency independent or a DC term in Equation 1.7, known as optical rectification, a term in which a doubling of the two frequencies occurs shown in Equation 1.8, second harmonic generation (SHG), another term where the output is a difference of the two frequencies as expressed in Equation 1.9, difference frequency generation (DFG), and a term for which the output is their sum as shown in Equation 1.10, known as sum frequency generation (SFG) [70–72].

The two methods that are most commonly utilized for the analysis of molecules at interfaces are those of second harmonic generation and sum frequency generation. In the case of second harmonic generation, the two frequencies present in Equation 1.6 are identical, and the outcome is a beam oscillating at twice the frequency of the initial radiation. This method has been used to great effect in microscopy, through which it is possible to determine orientation of molecules at a surface. This is possible as the light used for SHG microscopy can be polarized, with different polarizations of input radiation resulting in images with different regions of high and low intensity. The regions of high intensity represent those regions in which molecules are aligned in such a way to maximize the SHG signal while the dark regions are defined by molecules in orientations that would not allowed for SHG to occur. This SHG microscopic technique has been used extensively, being reviewed by Yamada [73] and Salasky [74] wherein they describing the recent developments in second harmonic microscopy and interferometry and describe how these methods are used in the study of molecular structure determination at surfaces. The studies of surface structure generally used some second-harmonic spectroscopic analog of a linear optical experiment, such as the studies involving circular dichroism (SHG-CD), linear dichroism (SHG-LD), and optical rotatory dispersion (SHG-ORD) [75,76], which is particularly useful in the study of the nonlinear optical response of chiral surface systems. As well, if the second harmonic generation experiment involves the generation of SHG at two different points simultaneously, one in a crystal of a known phase and the other at the interface of interest, the difference in phase can be used to determine orientation [77,78]. Another method for determining the absolute phase of nonlinear susceptibility uses second harmonic generation in a total internal reflection geometry. Since this configuration grants an amplification to the second harmonic generation process it is possible to generate two SHG signals at the different interfaces present, one from an applied gold layer and another from an adsorbed layer, in this case an adsorbed gas in a pressure cell. By comparing the phases of these two signals, the absolute phase of the nonlinear susceptibility of the adsorbed gas can be determined [79].

As useful as this technique may be, it is limited in by the fact that a single wavelength is used for each experiment. While experiments can be performed sequentially at different wavelengths [78], they tend to be constrained to the visible region, capable of probing the electronic excitations of molecules, but not their vibrational levels.

As such, among the second-order nonlinear techniques, visible-infrared sum-frequency generation (SFG) spectroscopy is particularly interesting since it probes surface vibrational modes through the use of a tuneable infrared source. The basic theory and utility of this method has been summarized neatly by Bain [71]. In general, sum frequency generation experiments are performed using a visible wavelength laser at a fixed wavelength and a tunable infrared radiation source. As the experiment progresses, and the infrared wavelength range of interest is scanned, the response seen is dependent upon a macroscopic average of the microscopic hyperpolarizability of each individual molecule at the surface.

$$\alpha^{(2)}_{ijk} = \langle R(\psi)R(\theta)R(\phi)\alpha_{lmn}\rangle \tag{1.11}$$

In equation 1.11, the important relationship between $\alpha^{(2)}_{ijk}$, which describes the hyperpolarizability of the molecule in the ijk or laboratory frame to that of α_{lmn}, the hyperpolarizibility of the molecule present in the lmn or molecular frame. These two values are related by $R(\psi)R(\theta)R(\phi)$, which describes the three rotations of an coordinate transformation, as described in general later in this Chapter.

Since the SFG technique depends upon the vibrational excitation of a molecule, it is possible to think of two possible cases during the experiment wherein the infrared radiation is either close to a resonant excitation that is active in the SFG experiment, or not. These two cases are depicted in Figure 1.2. This gives rise to both a resonant SFG polarizability, $\alpha^{(2)}_{ijk,\mathrm{R}}$ and a nonresonant SFG signal, $\alpha^{(2)}_{ijk,\mathrm{NR}}$.The overall second order

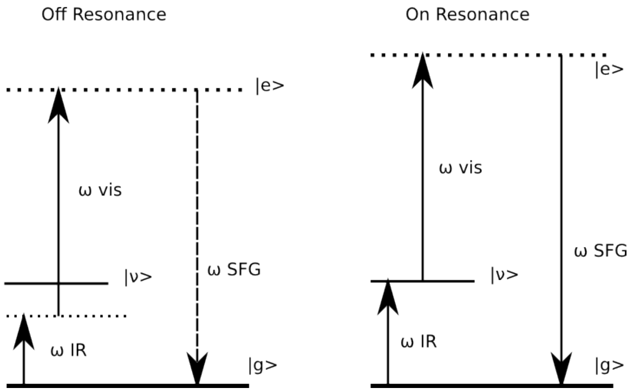

Figure 1.2: Depiction of the SFG three wave mixing process showing instances where the infrared radiation is equal to the vibrational energy of the molecule of interest and where it is not.

nonlinear susceptibility is therefore equal to the sum of these two contributions.

$$\alpha^{(2)}_{ijk} = \alpha^{(2)}_{ijk,\mathrm{R}} + \alpha^{(2)}_{ijk,\mathrm{NR}} \tag{1.12}$$

The value of $\alpha_{ijk,R}$, can be expressed in terms of the Raman, M_{ij} and infrared transitions, A_k, of any given vibrational mode.

$$\alpha_{ijk,R}(\omega_{\mathrm{IR}}) = \frac{1}{2h}\frac{M_{ij}A_k}{\omega_\nu - \omega_{\mathrm{IR}} - i\Gamma} \tag{1.13}$$

As such, one can see that only if a vibrational mode is both infrared and Raman active will it be visible to an SFG experiment. Up until this point we have only described the second order nonlinear response with respect to the molecular hyperpolarizability, $\alpha^{(2)}$. What is actually seen in the experiment as the wavelength range is scanned is not the response from individual molecules being excited vibrationally, but that of a macroscopic average of the molecules adsorbed at the interface. This macroscopic average, analogous to the molecular property $\alpha^{(2)}$, is known as the second order susceptibility, $\chi^{(2)}$, and the two are related as follows.

$$\chi^{(2)}_{ijk,R}(\omega_{\mathrm{IR}}) = \frac{N}{\varepsilon}\frac{<\alpha^{(2)}_{ijk,R}>}{(\omega_\nu - \omega_{\mathrm{IR}} - i\Gamma)} \tag{1.14}$$

Now that it is possible to target vibrational bands, they can be related to specific chemical moieties of the amino acid on the surface, allowing for structural information to be obtained without fluorescent- or radio-labelling. SFG spectroscopy has already proven to be useful in the study of amino acids [53,80–82], peptides [43,83–85], and proteins [86–89] adsorbed at various liquid interfaces. The analysis of protein structure at surfaces relies upon the detection of Amide I signals by SFG and the difference between the position of this signal in solution at the surface in order to detect adsorbed species. This has been used to study competitive adsorption of proteins to surfaces [90], changes in structure as a result of variation of pH [91] and in the determination of polymer ordering at surfaces [92].

However, for more detailed orientational analyses, the SFG experiment is performed using a combination of different beam polarizations, from which it is possible to extract multiple elements of the second-order susceptibility $\chi^{(2)}$ tensor. In addition, if the nonlinear optical properties of the molecule—all elements of its hyperpolarizability tensor $\alpha^{(2)}$—are known, then SFG spectra may be used to deduce the orientation of the functional groups that give rise to the response. There have been several illuminating accounts of this structural analysis in the literature [93–95]. Additionally, several reviews based on specific uses for these techniques, such as the study of adsorption to mineral-water interfaces [96], the air-liquid interface [97], antimicrobial proteins interacting with lipid bilayers [98], and the general mapping of molecular orientation at surfaces [99].

It is appropriate to focus on a small number of specific studies in greater detail, in order to illuminate the procedures used in recent analyses of this kind as well as to provide some further information that will be called upon in later chapters. One such instance is the work done with regards to the orientation of the pendant phenyl groups of polystyrene [100,101]. In these studies, the absolute orientation distribution of polystyrene, specifically the phenyl groups, at the polymer-air interface is determined. By performing the experiment in the SSP and SPS configurations, it was determined through the analysis of the C-H stretching modes that the phenyl rings were in fact ordered, and not rotating symmetrically about

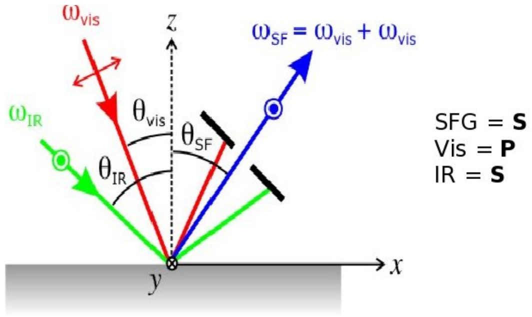

Figure 1.3: Simplified graphical representation of the SFG experiment highlighting the different polarization states of the individual beams in the experiment. This configuration is the SPS experiment shown in the co-propagating geometry. The designation SPS describes the polarization state of the radiation being used in the experiment in decreasing order of energy, with the SFG signal being measured in the S or perpendicularly polarized state, as with the infrared beam, while the visible beam is being used in the P or parallel polarized state.

their bond to the remainder of the polymer. The acquired spectra were fit based on ab-initio calculations with the amplitudes and widths of each of the 5 known phenyl modes being extracted. Finally, the absolute phase of the nonlinear susceptiblity was determined by comparing the phase of the resonant and nonresonant contributions to $\chi^{(2)}$ to a reference material of known phase: a self assembled monolayer of phenylsiloxane on silica. With this knowledge, the orientation was determined by fitting the spectra using three parameters. A narrow distribution of the tilt, θ, and twist, ψ, of the pendant phenyl rings as well as a ratio of the theoretically determined value for the hyperpolarizabilities $\alpha^{(2)}_{zzz}/\alpha^{(2)}_{xxz}$, were used to determine that the phenyl ring was tilted away from the surface normal at 57°. The methods used in this experiment were part of the inspiration for the work of Chapter 2.

Finally, the analysis of the structure of leucine molecules based on their SFG spectra at the air-water interface proved vital for the studies in Chapter 3 [82]. From this study, it was possible to compare mode positions in the SFG spectra of leucine at the solid-liquid interface, and also extract the information regarding the Fermi resonances known to exist in the wavelength region that was studied. The assumption was made in that work, however, that the modes were uncoupled, and their vibrational modes based on symmetry assignments were accurate. These were applied and used in an orientational analysis of the molecule at the air-water interface. This is a simplification for this system that we sought to avoid in our studies, but it did provide a source for their analysis, whereby they used the pendant methyl groups of the leucine molecule and the polarization dependence of their nonlinear susceptibilities to determine. Based on a δ-distribution, another simplification we sought to avoid, they discovered that the molecular orientation of leucine varies as a function of the number density at the surface with their most stable configuration at a tilt of $\theta \approx 40^\circ$ and a twist of $\psi \approx 25^\circ$, relative to the C_2 axis of the -C(CH3)$_2$ region of the molecule. These findings provided a starting point for the work performed in Chapter 3.

1.3.2 Ellipsometry and Polarimetry

The characterization of various surfaces and chemical species at interfaces has long been performed through the aid of optical techniques. These techniques generally rely upon carefully controlled or analyzed radiation interacting with the interface of interest. By determining the change in the polarization state of the radiation caused by the surface, optical and physical properties of the surface can be determined. This is useful as many methods that use carefully characterized radiation are capable of being surface selective, such as sum-frequency generation spectroscopy. However, difficulties arise in the case where the system of interest is anisotropic, inhomogeneous, or depolarizing [102–104]. If this is the case for the sample being studied some methods become unreliable, as they lack the rigourous analysis required to extract specific information regarding the surface of interest from the complex signal.

Several experimental methods have been employed for the analysis of optical systems by ellipsometry, and have been reviewed in books [105, 106] and in the literature reviews [107]. The basic concepts upon which ellipsometry experiments are made are shown in Figure 1.4. This figure shows the radiation incident to the sample being polarized at a known angle, in this case 45° to the plane of incidence, and the induced change in

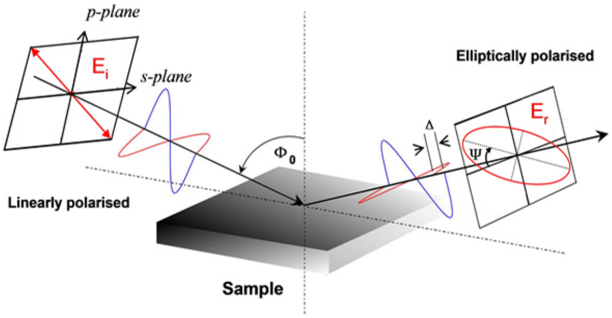

Figure 1.4: Simple description of the ellipsometry experiment. A well known input polarization state, in this case linearly polarised light at $45°$ to the plane of incidence is radiated upon a sample inducing a change in the polarization state, which is measured as being elliptically polarised. The ellipsometric parameters, Ψ and Δ are shown, relating to the azimuth of the elliptically polarised light and the phase shift between the perpendicular (s and p) portions of the output radiation respectively.

polarization that is experienced upon reflection. By relating the polarization state of the reflected light to that of the incident light, it is possible to determine the optical and physical properties of the sample.

Originally, these optical parameters were obtained from simple null-ellipsometers that obtained the ellipsometric parameters Ψ and Δ through the nulling of a signal from a sample, accomplished by rotating the polarizer and compensator before the sample such that the elliptically polarized light incident on the sample is reflected as linearly polarized light that is nulled when incident on an analyzer perpendicular to it. This method, while remarkably accurate, requires time to accurately null the signal, even if this process is automated. Another drawback inherent in this method is that it is only capable of determining these two parameters, and not the full Mueller matrix. At the next level of complexity exists the rotating element ellipsometer. These systems, generally constructed in the form of polarizer-compensator-sample-analyzer or polarizer-sample-compensator-analyzer configurations, provide some modulation in the polarization of the light incident or excident to the sample of interest. As such, a number of pairs of Ψ and Δ are obtained, from which information regarding the sample can be obtained. If performed by hand, individual pairs can be obtained, or if automated a large number of stationary points can be obtained. If the rotating element is present moving with a constant rotation and frequency based detection is employed, Ψ and Δ can be obtained directly and at high speeds. Closely related to this instrument is the rotating compensator ellipsometer, that functions in a similar fashion. These rotating element ellipsometers, while faster than null ellipsometers, contain similar drawbacks. In terms of rotating element based Mueller matrix ellipsometers, there exists examples based upon the employment of dual rotating compensators [108–110]. While effective, these systems require incredibly stable rotation of the compensators with very specific frequency relationships for real-time detection or a stepwise rotation of the compensators in order to produce the waveform followed by mathematical processing in order to determine the Mueller matrix.

In the case of an ideal, non depolarizing surface, the system can be described in terms of four complex reflection coefficients, expressed by the Jones matrix

$$\mathbf{J} = \begin{bmatrix} r_{pp} & r_{ps} \\ r_{sp} & r_{ss} \end{bmatrix} = r_{ss} \begin{bmatrix} \rho & \rho_{ps} \\ \rho_{sp} & 1 \end{bmatrix} = \begin{bmatrix} \tan(\psi)e^{i\Delta} & \tan(\psi_{ps})e^{i\Delta_{ps}} \\ \tan(\psi_{sp})e^{i\Delta_{sp}} & 1 \end{bmatrix}. \tag{1.15}$$

In equation 1.15, the values of r are the complex reflection coefficients, including the cross polarization elements, r_{ps} and r_{sp}, which are equal to zero for isotropic samples, and the two ellipsometric parameters, ψ and Δ which are frequently used to describe isotropic samples in the literature.

As an example, the reflection coefficients for a single interface between two isotropic media can be determined as follows

$$r_{pp} = \frac{n_1 \cos(\phi_0) - n_0 \cos(\phi_1)}{n_1 \cos(\phi_0) + n_0 \cos(\phi_1)} \tag{1.16}$$

$$r_{ss} = \frac{n_0 \cos(\phi_0) - n_1 \cos(\phi_1)}{n_0 \cos(\phi_0) + n_1 \cos(\phi_1)}. \tag{1.17}$$

The values of ϕ_0 and ϕ_1 in Equation 1.16 describe the angle at which the light propagates in either medium while n_0 and n_1 are their complex indices of refraction.

Adding in one more degree of complexity, placing a single isotropic film of thickness d_f and an index of refraction of $\tilde{n_f}$, between two isotropic media, the reflection coefficients are described by the Airy formula

$$r_{ss,pp} = \frac{r_{1,ss,pp} + r_{2,ss,pp}e^{-2ib}}{1 + r_{1,ss,pp}r_{2,ss,pp}e^{-2ib}}$$

where

$$b = \frac{2\pi d_f}{\lambda}\tilde{n_f}\cos(\phi_f) \tag{1.18}$$

and $r_{1,ss,pp}$ and $r_{2,ss,pp}$ are the reflection coefficients for either s or p polarized light at the two interfaces of the film, while λ describes the wavelength used for the experiment. Increasing levels of complexity call for more complete theoretical treatments, but in the absence of depolarizing effects these equations suffice. Additionally, in the absence of depolarizing effects, a study of the optical anisotropy of the sample can be used to determine structural order [111]. In this study, a polarization transfer model is described that relates the change in polarization of the input radiation through the birefringence and dichroism of liquid crystalline polymers. This also works for circular dichroism, and using models for these two sets of parameters allows for an accurate determination of the ordering of the liquid crystalline polymer.

When depolarizing effects do occur though, frequently the best solution involves the invocation of Mueller calculus and the analysis of the Mueller matrix of the sample, which is capable of successfully encoding both the sample information and the depolarization information [104, 112, 113]. Depolarization occurs as a result of the interaction of the incoming radiation with a rough surface. The immediate result of a depolarizing sample is that the output radiation has an overall degree of polarization that is less than the input polarization.

For many interfaces under investigation, structural information is sufficiently decoded from the polarization of the reflected beam. In general however, interfaces comprised of adsorbed proteins are inhomogeneous, rough, and anisotropic [114–117]. Some of the original work in the application of the study of proteins at surfaces was conducted using simple null ellipsometry [118, 119]. These measurements were performed in a simple Polarizer-Compensator-Sample-Analyzer configuration, and through the analysis of the ratio of the reflection coefficients for p- and s-polarized light, the ellipsometry parameters Ψ and Δ can be determined.

$$\frac{r_p}{r_s} = \tan\Psi e^{i\Delta} \tag{1.19}$$

This method is very useful for the determination of adsorption isotherms for proteins, as well as determining their thickness and refractive indices. A slightly more advanced method has been employed in which a total internal reflection geometry is used to provide a greatly improved signal to noise ratio [120]. Finally, the use of spectroscopic ellipsometry, that being ellipsometric experiments performed at multiple wavelengths, has been used to study protein adsorption and the impact of pH [121]. One significant drawback to this though is that spectroscopic ellipsometry requires significantly more complicated experimental procedures.

Real-time Ψ and Δ measurements are most readily determined from high speed polarization modulation. This high speed polarization modulation can be accessed through the use of photelastic modulators as the polarization modulating element. Through various implementations, these PEM based ellipsometers are capable of performing as Stokes polarimeters [122–125] capable of determining Ψ and Δ at fast rates. These photoelastic modulator based systems are also amenable for use as Mueller matrix ellipsometers [126–128]. These Mueller matrix ellipsometers are not without their inherent technical difficulties. These issues involve the complex waveform analysis used in ref 126, which is based on synchronized PEMs performing at kilohertz frequencies. Other systems require data obtained in multiple orientations of the ellipsometric configuration, or the use of up to 8 lock-ins simultaneously synchronized to various sums, multiples, and differences of the PEM operating frequencies. These techniques pose formidable technical challenges, but the precision they are capable of as well as their accuracy, provided they are appropriately calibrated, make them extremely useful.

A simple description of the photoelastic modulator and its function is necessary at this point. While there are many geometries that can be used to form a photoelastic modulator, they are all based upon the application of an external driving force to a normally optically isotropic optical element inducing a time dependent variation in the optical retardation. The optical element, normally a form of quartz, is cut to specific shape and dimensions as its resonant frequency will be defined by its physical structure. The external force is generally applied in the form of a piezoelectric transducer coupled to the quartz. When a photoelastic modulator is coupled to a linear polarizer at $\pm 45°$, the result is a frequency dependent elliptical polarization state dependent upon the instantaneous strain of the optical element. Thus, it is possible to produce a varying polarization states at a high frequency.

While an effort has been made to make the complexities of Mueller matrix ellipsometry known, its benefits are tangible, particularly in the analysis of very complex systems. It has been employed in the study of liquid crystals [129, 130] as well as in the study of protein adsorption to a number of surfaces [119, 120, 131–137]. In these cases, Mueller matrix ellipsometry possesses a unique ability in that it is capable of encoding within a samples Mueller matrix information regarding depolarization and anisotropy effects, as protein layers are commonly rough, anisotropic and depolarizing.

It is important to discuss the direct characterization of a depolarizing surface, as it is performed by measuring elements of the sample's Mueller matrix, $\mathbf{M}$. The 16 elements of this 4×4 matrix relate the incident and measured output Stokes vectors and may be used to determine the optical and geometric properties of these anisotropic systems [128,138–140]

$$\mathbf{S}_{\mathrm{out}} = \mathbf{M}\mathbf{S}_{\mathrm{in}} \tag{1.20}$$

where **M** is represented in normalized form as

$$\mathbf{M} = \begin{bmatrix} 1 & m_{12} & m_{13} & m_{14} \\ m_{21} & m_{22} & m_{23} & m_{24} \\ m_{31} & m_{32} & m_{33} & m_{34} \\ m_{41} & m_{42} & m_{43} & m_{44} \end{bmatrix} \tag{1.21}$$

and the 4 × 1 vectors describing the input and output polarization states, $\mathbf{S}_{\text{in}}$ and $\mathbf{S}_{\text{out}}$ are the input and output Stokes vectors [141], described below.

$$\mathbf{S} = \begin{bmatrix} S_0 \\ S_1 \\ S_2 \\ S_3 \end{bmatrix} = \begin{bmatrix} I_{\text{total}} \\ I_0 - I_{90} \\ I_{+45} - I_{-45} \\ I_{\text{rcp}} - I_{\text{lcp}} \end{bmatrix} \tag{1.22}$$

where S_0 represents the total intensity of the light; S_1 is the excess of horizontally-polarized over vertically-polarized light; S_2 the excess of light polarized at $+45°$ over that at $-45°$; S_3 is the excess of right circular polarization of the two circularly-polarized states. Measurement of the complete Stokes vector also yields the degree of polarization since its elements are related by

$$S_0^2 \leq S_1^2 + S_2^2 + S_3^2 \tag{1.23}$$

Stokes polarimetry is capable of accurately describe the system of interest and with the advent of the photoelastic modulation of light, very precise measurements of the four stokes parameters can be obtained at very fast rates.

In the simple case where the sample is not depolarizing, a direct connection between the Muller matrix and the calculated Jones matrix can be drawn.

$$\mathbf{M} = \mathbf{A}(\mathbf{J} \otimes \mathbf{J}^*)\mathbf{A}^{-1} \tag{1.24}$$

where

$$\mathbf{A} = \begin{bmatrix} 1 & 0 & 0 & 1 \\ 1 & 0 & 0 & -1 \\ 0 & 1 & 1 & 0 \\ 0 & i & -i & 0 \end{bmatrix}$$

In the case that the sample does depolarize light, there is no direct connection between the calculated parameters of the Jones matrix and the elements of the Mueller matrix and it becomes necessary to fit the results of the ellipsometric experiment to a model including depolarization effects. This involves treating the Mueller matrix as it is shown in Equation 1.21.

In order to study these complex systems despite the problems mentioned, it is important to note that the two aforementioned techniques become complementary: Stokes polarimetry providing high speed information on the changing physical and optical constants of the growing monolayer as it forms including the development of depolarization while Mueller matrix ellipsometry can be employed when the adsorbing system reaches a steady state allowing for the extraction of all information specifically pertaining to the adsorbed layer of protein. It is in this cause that a system capable of interchangably performing as high speed and high precision dual-PEM based Stokes polarimeter and an accurate Mueller matrix ellipsometer as well as the necessary calibration procedure has been developed.

This will also give an insight into the overall timeframe of an adsorption process, which is important as our SFG experiments must be conducted at equilibrium. Also, the additional Mueller matrix determination, which can be performed in the same configuration as the dual PEM Stokes polarimeter with a slightly modified procedure, allows for the study of the depolarization effects, anisotropy, adsorbed mass and interfacial thickness. Depolarization can be noted in the case that the overall polarization of the detected beam is no longer equal to the polarization of the input state or, mathematically if the equality in the Equation 1.23 does not hold true. Should this occur, it would be necessary to determine the Mueller matrix of the sample in order to properly defined it.

Both of these sets of information are extremely valuable in providing a more complete view of the overall structure at the interface. As such, the design and calibration of a high speed Stokes polarimeter and methods for the determination of the Mueller matrix based on data obtained in the same configuration as the polarimeter will be an important goal of this work.

1.3.3 Methods not Employed in this Work

Protein adsorption to surfaces has been studied by a variety of *in situ* experimental methods, including fluorescent- and radio-labelling [5], confocal fluorescence microscopy [142], total internal reflection fluorescence [143], and quartz crystal microbalance impedance [144–149].

These methods can be useful, but in the case of fluorescent techniques, they generally require the addition of a label, which can affect the physical or chemical properties of the analyte. Commonly, a rhodamine dye based adduct is used in place of the original molecule of interest. As an example, in a study of the adsorption of bovine serum albumin to a hydrophilic surface under various pH conditions, a tetramethylrhodamine isothiocyaniate bovine serum albumin protein analog was used. Still, with proper calibration of the fluorescent response based on concentration, adsorption isotherms were determined and an analysis of the surface structure of the molecule attempted [5].

Quartz crystal microbalance impedance measurements are exceptional at determining the overall amount of analyte present at the surface, but they provide very little insight into the orientation of adsorbates. The process involved in quartz crystal impedance results in it being a very accurate method for determining the change in mass as a result of adsorption of molecules to the surface. Since quartz is piezoelectrically active, the application of a voltage across an AT-cut piece of quartz causes it to undergo a strain in the shear direction. By varying the polarity of the applied voltage one can change the direction of the strain. Thus, by modifying the amplitude of the voltage accordingly it is possible to induce a standing wave in the crystal. The addition of a film to the quartz crystal will alter the damping of the system or the energy dissipation upon the removal of the applied voltage. It is by the modeling of the decay of the oscillation that the change in mass at the surface can be determined. This method has been used to great effect in probing biomolecular recognition reactions [144], studying the adsorption kinetics of self assembled monolayers [150], and in determining the differences in adsorption of proteins to naked and polymer coated quartz [149].

A great deal of the studies in the literature that can be considered to be *in situ* include some form of infrared absorption techniques. In order to ensure that the studies focus upon the interfacial region they primarily involve total internal reflection, such as in the form of attenuated total reflection infrared spectroscopy [151, 152]. These methods rely upon the production of an evanescent wave that enters the interfacial region, traveling to a depth of d_p as defined by Equation 1.25, produced by the incoming infrared radiation undergoing total internal reflection through a crystal. This penetration depth is defined by the physical characteristics of the two media that are in contact, namely their indices of refraction, n_1 and n_2, as well as the wavelength of the light used in the experiment, λ.

$$d_p = \frac{\lambda}{2\pi n_1 \sqrt{(\sin(\theta)^2 - (\frac{n_2}{n_1})^2)}} \tag{1.25}$$

These evanescent wave extends for a few microns into the region of interest, making it acceptably surface specific. The necessity for total internal reflection in order to generate these evanescent waves has lead to the development of several experimental configurations, such as those shown in Figure 1.5. The crystals used are cut in such a fashion to maximize their contacts with the interface being studied as well as the number of internal reflections that are experienced by the light used in the experiment.

This method has been utilized to study the adsorption of molecules onto these bare crystals as well as crystals that have been coated by other materials, such as polymers, and particulate matter in contact with the crystals [152]. When studying the characteristics of adsorbed proteins using infrared techniques it is common to focus on specific absorption modes, such as those of the amide I and amide II shifts. It is known that upon adsorption of proteins their amide I and II absorptions in their infrared spectra shift in

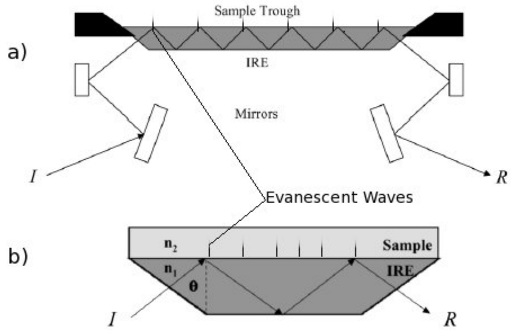

Figure 1.5: Two different attenuated total reflection experimental configurations adapted from Ref 152. Both systems rely upon the induced evanescent wave that propagates into the sample to a depth as described in Equation 1.25. These evanescent wave only interacts with molecules present within that depth, making experiments based on these configurations moderately surface specific

comparison to the solution phase protein [153]. This has also been shown to be useful in determining the secondary and tertiary structure of proteins adsorbed to crystal surfaces coated with polymers. The relationship between the orientation and conformation of the protein and the resultant impact upon the shift of the amide stretches facilitates this [151]. Additionally, attenuated total reflection experiments have been coupled with Fourier Transform techniques allowing for the determination of adsorption kinetics [145].

Another common method for the study of adsorbed proteins would be surfaced enhanced Raman spectroscopy. Again, this method is quite good for the study of adsorbed molecules but specifically applied to silver or gold surfaces. While this is the case, its impact upon the field of studying molecules at surfaces cannot be understated. As a result of the remarkable enhancement of signal from molecules adsorbed at these specific surfaces, it has been used to determine the structure of di- and tri- peptides at silver surfaces [154], as well as for studies of temperature dependent adsorption of proteins to nanopatterned silver surfaces [155], as a tool for the high throughput screening of hemoproteins for adhesion to surfaces [156] and for the study of molecules adsorbed to gold nanoparticles [157].

The other methods involve *ex situ* experimental techniques, such as atomic force microscopy [158–160], electron microscopy [161, 162], neutron scattering [163] and x-ray photoelectron spectroscopy, known in this case as electron spectroscopy for chemical analysis [164–167]. These methods have great analytical strengths, such as the ability to distinguish with great accuracy the different species present at the surface, as in the case of x-ray photoelectron spectroscopy, or in the production of detailed images of molecules at surfaces in the case of the atomic force and electron microscopy techniques. However, these techniques require the sample to be under at least high vacuum conditions (10^{-5} Torr). As such, while these samples can be initially formed from biologically relevant media, they must be removed and placed under vacuum prior to analysis. While they provide insight into the various unknowns involved in molecular adsorption to surfaces, they cannot account for variations between the molecules surface orientation distributions under high vacuum conditions and the orientation distribution it would possesses at the surface when still in contact with solution. Still, AFM has been used to monitor the formation of protein clusters at surfaces and their growth mechanisms [158]. Neutron scattering techniques require low temperatures in order to effectively combat noise in the experiments, typically on the order of 10K, far below biologically relevant temperatures. However, they do provide insight into the geometry of molecules on the surface, capable of determining the surface structure at a resolution down to 1-4 Å [168].

In terms of amino acids, specifically, adsorption of specific amino acids to various surfaces has been studied in a variety of methods, including electron microscopy [162], X-ray diffraction [52], spectrophotometry [55], and chromatography [59, 60].

1.4 Computational Methods for Use in the Study of Molecules at Surfaces

1.4.1 Molecular Dynamics Simulations

While there is a wealth of experimental methodologies that are capable of determining information regarding the interfacial structure of molecules, it is often necessary to employ computational methods to support the conclusions arrived at by experimental procedures. This necessity is compounded by the fact that while the majority of experimental techniques determine information based on an ensemble average of molecules at the surface, computational techniques are capable of studying systems using discrete molecules, making the two techniques complimentary.

However, even with a relatively small number of analyte molecules in a solution interacting with a surface, these calculations can become inhibitively long, requiring great deals of computational time to complete. While these problems are well known and methods to overcome these difficulties have been developed, these techniques still face considerable challenges [169]. As such, many methods have been developed that can reduce the amount of time required to study any system. Molecular mechanics is one such method, that relies upon empiricially parameterized equations that are capable of modeling physical forces in the system of interest. Within the realm of molecular mechanics exist a variety of sub-methodologies, such as Monte Carlo, as well as molecular dynamics, which employs Newtonian motion to study the forces and energy that exist in a system of more than two particles. While steps have been made to perform ab initio molecular dynamics simulations [170–172], which would allow for the study of quantized phenomena such as bonding, for systems such as those studied herein involving thousands of discrete water molecules and a leucine molecule, the computational time required would be astronomical. Luckily, since the interaction between solvent and analyte and the analyte and the surface in this system are purely physical, and as such can be effectively modeled with Newtonian physics. In the literature, there have been considerable computational studies on interfacial regions using molecular dynamics and Monte Carlo techniques [158, 169, 173–176].

This work utilized molecular dynamics simulations. These calculations are based upon the calculation of a potential energy for a given configuation of molecules, with each atom present having a specific force acting upon it. This force is used to determine a displacement, based on a femtosecond timescale, to which the molecules move, followed by another potential energy calculation. This process is repeated until a desire timescale has been studied. It is understood that if a long enough timescale is employed in the experiment, then accurate statistics can be determined. What is of primary interest in this work is the fact that these studies provide a molecular level snapshot of the cartesian coordinates of the molecules in question. Simply put, these simulations provide use with a theoretical orientational analysis for molecules present at the surface, which can then be related to other data to provide a more complete structural analysis of experimental systems. As an example, an image obtained from Ref 45 is shown in Figure 1.6. In the image, a snapshot of an adsorbed peptide at a surface is shown. Along with the positions of each of the atoms in the peptide, the positions of the surrounding water molecules and those of the surface are known as well, allowing for a direct look into the nature of the adsorbed protein and its environment.

The work of Chapter 3 is also based upon studies of this form, performed by previous group members, Travis Trudeau and Kailash Jena [177, 178]. These two studies focused on the study of the adsorption of the amino acid leucine to artificial surfaces of varying hydrophobicity and the analysis of the surface structure of water at a polymer interface as a function of varying the ionic strength of the solution. The first study is of vital interest to the study of the orientational analysis of leucine on polystyrene. The study involved the production of surfaces with varying hydrophobicities, which were produced by varying the Lennard-Jones parameter ε, present in the following equation

$$U(z) = 2\pi\sigma^2\varepsilon\left[\frac{2}{5}\left(\frac{\sigma}{z}\right)^{10} - \left(\frac{\sigma}{z}\right)^{4}\right]. \tag{1.26}$$

Through the variation of ε present in 1.26, which describes the depth of the potential

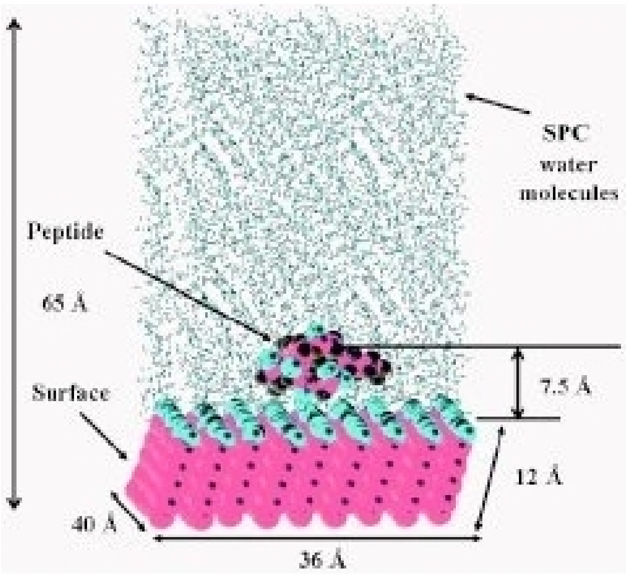

Figure 1.6: An example of peptide-surface adsorption in an MD simulation obtained from Ref 45. The information accessible from this type of analysis is obvious, with the placement of all surrounding water molecules and exact positions of the adsorbed peptide, in the case of this paper a nonamer of the form G_4-X-G_4, are known.

well near the surface, it was possible to produce surfaces with different contact angles with water. Within the simulation, it was noted that leucine adsorbed to the surface in two different configurations, adopting an orientation either perpendicular or parallel to the surface. These two orientations, dubbed standing and laying, were present in different quantities on the different surfaces, having a greater portion of standing molecules overall, but with a greater proportion of laying molecules at lower contact angles (more hydrophobic) surfaces. The differences between these two populations provided the impetus to study the SFG spectra of leucine at a polymer surface with a contact angle within the range studied (84–156°) using the difference in surface conformer populations.

Utilizing these computational methods, in concert with the SFG experiment, this work seeks to describe not only the orientation of amino acids present at surfaces but to develop scalable methodologies that can be used at will in further studies.

1.4.2 Electronic Structure Calculations

Since molecular dynamics can be used to model molecules at surfaces, it has been utilized to determine orientation distributions at surfaces and these, in turn, can be used to predict SFG spectra [179, 180]. However, great difficulties still exist in performing this task, specifically in defining the relationship between ab initio data required for spectral simulation and the orientation of the molecule at the surface.

To this end, it is necessary to obtain an expression for the second order nonlinear polarizability for the vibrational modes of interest. In simple cases, local symmetry may be considered to arrive at analytical expressions for $\alpha^{(2)}$ elements using bond-additivity models for the dipole and polarizability response [181–183]. However, often the normal modes are strongly-coupled or depolarization effects exist that cannot be described by these models, making analysis difficult. In such cases, quantum mechanical calculations may be used to yield estimates of $\alpha^{(2)}$ [100, 179, 184–186].

$$\alpha^{(2)}_{abc,R}(\omega_{\mathrm{IR}}) \approx \sum_{\nu} \left(\frac{\partial \alpha^{(1)}_{ab}}{\partial Q_a}\right) \left(\frac{\partial \mu_c}{\partial Q_a}\right) \frac{1}{\omega_\nu - \omega_{\mathrm{IR}} - i\Gamma} \tag{1.27}$$

In Equation 1.27, the value of $\alpha^{(2)}$ is determined by calculating the product of the derivatives of the polarizability and dipole moment, applying a Lorentzian lineshape. This approximation is determined through the use of ab initio calculations [187], from which the direction of atoms for each mode of interest can be determined. By stepping along normal mode coordinate and performing discrete calculations for the dipole and polarizability of the molecule at each point, the derivatives can be determined, and thus an approximation for $\alpha^{(2)}$ found by determining the slope at the zero or equilibrium point along the modes vibration.

Molecular dynamics studies have focused extensively upon the prediction of the SFG spectra of water [179, 180]. Aside from the obvious interest in this experiment, the reason for this is based upon the fact that water is relatively simple to model and, thus, amenable to computational simulations. This work, by the group of Akihiro Morita, has focused on improving the accuracy of the prediction of SFG spectra of water through the use of the time-dependent formalism. This is in contrast to the earlier method used, which relied on the modeling of the frequency dependent hyperpolarizability through quantum chemical calculations and sampling the surface structures using molecular dynamics, similar to the method employed in Chapter 3 of this work. The time dependent approach employs a time based correlation function for the evaluation of the hyperpolarizability. In essence, this method performs a molecular dynamics simulation using a very small time step, thus allowing for the determination of the physical parameters of the system during the vibrations of the molecule. This allows for the determination of a number of factors that cannot be calculated using the quantum calculations, such as the dielectric constant corrections, vibrational dephasing, vibrational coupling, and requires fewer empirical corrections. While it would have been ideal to use this method in our study, the application of this method to more complicated systems than simply pure water, for which it works very well, is quite difficult.

1.5 General Description of Coordinate Transformations

It is frequently of necessity in any orientation analysis to project physical quantities from one coordinate system to another. This can be facilitated through the use of appropriate coordinate transformations based on Euler angle rotations, a mathematical procedure known to relate frames of reference through the application of three consecutive rotation steps. This procedure is described in complete detail in various books [188, 189], and is used for a variety of procedures, primarily in the realm of computer graphics manipulation. Specifically for the purposes of this thesis, this was utilized to transform physical properties between a molecular based frame, defined by three perpendicular vectors lmn, and the laboratory frame, generally defined by three perpendicular vectors, ijk.

Prior to delving into the actual mathematics involved in this deceptively simple concept, it is useful to go through the procedure visually. This example will involve the

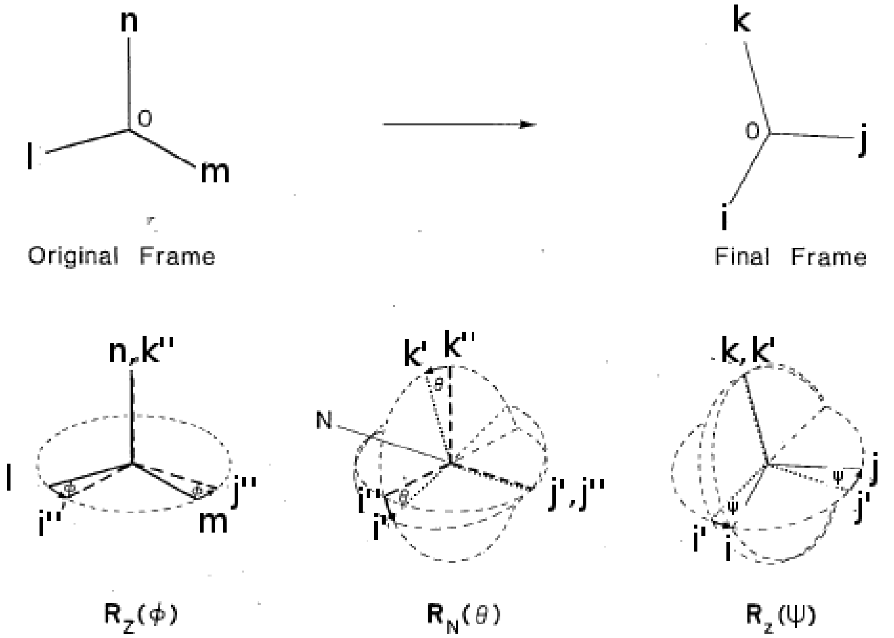

Figure 1.7: General rotation of one Cartesian coordinate system into another through the application of an Euler transformation. ijk is referred to as the laboratory frame while lmn defines the molecular frame. Adapted from Ref 188

transformation from the molecular frame, lmn, to the laboratory frame, ijk.

As stated previously, this procedure can be broken down into three steps: initially the molecular frame undergoes a counterclockwise rotation about the n axis of the magnitude of ϕ degrees, followed by a counterclockwise rotation about the intermediary y' axis, otherwise known as N, the line of nodes, and finally to bring it completely into the laboratory frame, a counterclockwise rotation about the k axis of the newly formed laboratory frame. The result, as seen pictorially in Figure 1.7, is the transformation of one coordinate system into another. Now it is necessary to describe this operation mathematically.

The vast majority of the time it is being utilized during this work it is found in matrix form, as each of the three steps described before can be written in terms of a rotation matrix. Thus, it is necessary to define what is known as the direction cosine matrix or

DCM. If we consider two independent vectors, each present in their respective coordinate systems, defined as $v_{lmn} = (v_l, v_m, v_n)$ and $v_{ijk} = (v_i, v_j, v_k)$, we can express the DCM as relating the two in the form of

$$v_{ijk} = \sum_{l,m,n} \Phi_{M,L}(\phi, \theta, \psi) v_{lmn} \tag{1.28}$$

$$v_{lmn} = \sum_{i,j,k} \Phi_{L,M}(\phi, \theta, \psi) v_{ijk} \tag{1.29}$$

where Φ is the direction cosine matrix and the subscripts L and M stand for laboratory and molecule based coordinate systems. As stated earlier, this DCM can be defined as the product of three consecutive rotations, this time in matrix form.

$$\Phi(\phi, \theta, \psi) = \mathrm{R}(\psi)\mathrm{R}(\theta)\mathrm{R}(\phi) \tag{1.30}$$

Since these three operations are known, specifically as rotations about a 'z' axis of the coordinate system in the cases of $\mathrm{R}(\psi)$ and $\mathrm{R}(\phi)$ as well as one rotation about a 'y' in the case of $\mathrm{R}(\theta)$, these three rotation matrices are well established.

Here, the transformation of the laboratory frame, ijk, into the molecular frame lmn, through the intermediate frames $l''m''n''$ and $l'm'n'$ will be described in terms of the three aforementioned rotations in matrix form:

$$\begin{bmatrix} l'' \\ m'' \\ n'' \end{bmatrix} = \mathrm{R}(\phi) \begin{bmatrix} i \\ j \\ k \end{bmatrix} = \begin{bmatrix} \cos\phi & \sin\phi & 0 \\ -\sin\phi & \cos\phi & 0 \\ 0 & 0 & 1 \end{bmatrix} \begin{bmatrix} i \\ j \\ k \end{bmatrix} \tag{1.31}$$

$$\begin{bmatrix} l' \\ m' \\ n' \end{bmatrix} = \mathrm{R}(\theta) \begin{bmatrix} l'' \\ m'' \\ n'' \end{bmatrix} = \begin{bmatrix} \cos\theta & 0 & -\sin\theta \\ 0 & 1 & 0 \\ \sin\theta & 0 & \cos\theta \end{bmatrix} \begin{bmatrix} l'' \\ m'' \\ n'' \end{bmatrix} \tag{1.32}$$

$$\begin{bmatrix} l \\ m \\ n \end{bmatrix} = \mathrm{R}(\psi) \begin{bmatrix} l' \\ m' \\ n' \end{bmatrix} = \begin{bmatrix} \cos\psi & \sin\psi & 0 \\ -\sin\psi & \cos\psi & 0 \\ 0 & 0 & 1 \end{bmatrix} \begin{bmatrix} l' \\ m' \\ n' \end{bmatrix} \tag{1.33}$$

Finally, we possess the overall transformation in terms of three individual rotation matrices, which we can then multiply through to obtain the overall direction cosine matrix.

$$\begin{bmatrix} l \\ m \\ n \end{bmatrix} = \mathrm{R}(\psi)\mathrm{R}(\theta)\mathrm{R}(\phi) \begin{bmatrix} i \\ j \\ k \end{bmatrix} \tag{1.34}$$

$$D = \begin{bmatrix} \cos\phi\cos\phi\cos\psi - \sin\phi\sin\psi & \sin\phi\cos\theta\cos\psi + \cos\phi\sin\psi & -\sin\theta\cos\phi \\ -\cos\phi\cos\theta\sin\psi - \sin\phi\cos\psi & -\sin\phi\sin\theta\sin\psi + \cos\phi\cos\psi & \sin\phi\sin\theta \\ -\sin\theta\cos\psi & \sin\theta\sin\psi & \cos\theta \end{bmatrix} \tag{1.35}$$

$$\begin{bmatrix} l \\ m \\ n \end{bmatrix} = D \begin{bmatrix} i \\ j \\ k \end{bmatrix}. \tag{1.36}$$

Now, a complete, single matrix for the purposes of transforming physical quantities from one coordinate system into another is possessed. However, there is one more interesting piece of information remaining. While the matrix in Equation 1.36 describes the transformation from ijk to lmn it is in fact a unitary transformation matrix, and as such its inverse is equivalent to the DCM for the rotation from lmn into ijk.

$$\begin{bmatrix} i \\ j \\ k \end{bmatrix} = D^{-1} \begin{bmatrix} l \\ m \\ n \end{bmatrix} \tag{1.37}$$

where the inverse DCM is defined as

$$D^{-1} = \begin{bmatrix} \cos\phi\cos\psi - \sin\phi\sin\psi & -\cos\phi\cos\theta\sin\psi - \sin\phi\cos\psi & \cos\phi\sin\theta \\ \sin\phi\cos\theta\sin\psi + \cos\phi\sin\psi & -\sin\phi\cos\theta\sin\psi + \cos\phi\cos\psi & -\sin\theta\cos\psi \\ -sin\theta\cos\psi & \sin\theta\sin\psi & \cos\theta \end{bmatrix} \tag{1.38}$$

These powerful transformations allow for the analysis of information gathered from multiple sources within a single frame, allowing for the information to be compared and, eventually, for the extraction of orientation information. There are, however, several caveats present in this method. It is vitally important to maintain a self consistent procedure for each transformation, using identical definitions for the laboratory and molecular frames as well as adhering to sign conventions for all angles used in the specific rotations. In order to further elucidate the application of these transformations so as to permit the extraction of orientation information, the complete methods for determining α and μ derivatives for phenylalanine and leucine in the laboratory frame will be described in full detail in Chapter 2.

1.6 Objectives

The general objectives of this work are twofold; (1) to develop analytical methodologies capable of determining the surface structure of molecules adsorbed to hydrophobic dielectric surfaces of interest and (2) to develop an instrument capable of monitoring the kinetics of the adsorption process as well as to determing the physico-optical properties of the adsorbed layers. For the purposes of the former, the combination of sum frequency generation experiments and computational methods, including quantum chemical calculations and molecular dynamics simulations, was employed as described in Chapters 2 and 3. For the latter, a high speed Stokes polarimeter was developed and proven capable of studying the kinetics of the adsorption processes and was readily converted to a Mueller matrix ellipsometer, satisfying the requirement for the determination of the systems optical properties.

Two different methods were developed for the determination of the molecular orientation of molecules adsorbed to surfaces from sum frequency generation experiments. In the case where an SFG active normal mode can be assigned with confidence, the direct connection between the intensity of a sum frequency generation active normal mode with its orientation with respect to the surface normal can be exploited. By performing quantum chemical calculations on the molecule of interest and carefully approximating the response of the normal mode to the sum frequency generation experiment it is possible to generate equations for their amplitudes based on their orientation through the use of an orientation distribution function. By comparing these theoretically determined amplitudes to those obtained from the sum frequency generation spectra themselves it is possible to determine the orientations that provide amplitudes that model the spectra accurately, and in turn determine the orientation of the molecule at the surface. While this method is extremely useful, as exhibited in the study of phenylalanine on polystyrene presented in Chapter 2, it is not entirely general as it requires knowledge of the normal mode assignments prior to the orientation analysis. For this reason, it has be named the “Top Down” approach, as it is possible to determine the surface orientation only if certain high level information is known about the molecule of interest prior to the study.

As alluded to previously, the “Top Down” method is not entirely general as it requires the exact knowledge of the normal mode assignments. As a second requirement it also requires that the modes are not coupled with one another and thus spread around different parts of the molecule. This is due to the fact that the “Top Down” method requires the definition of a plane containing the atomic motions of the vibrations of interest, and based on this it is capable of determining the orientation of that plane with respect to the surface and thus the molecule itself. There are, of course, many instances where there would either be many active vibrational modes in the region of interest, such as for any molecule with a large number of similar chemical groups in its structure, or with heavily coupled modes, resulting from there being a large number of vibrations with similar energies. This would be the case for most large biomacromolecules, such as proteins. Since these molecules can possess many regions with similar chemical properties, it is likely that they will produce congested sum frequency generation spectra and that their computationally-determined normal mode analyses would show coupling between modes. Thus, another method is needed to study the orientation of molecules such as these, and for this we turn to molecular dynamics simulations. Provided a sufficiently long molecular dynamics simulation is performed on the analyte in the solvent of interest that it is allowed to adsorb to a surface that accurately models the system studied in the sum frequency generation experiment, it is possible to determine a distribution of the analytes surface orientation. What is required is a definition of some parameters that will define the overall structure of the analyte, such as interatomic distances, dihedral angles, vectors based on chemical moieties, or some combination of these. Upon analysing the trajectory based on these parameters, it is possible to obtain a collection of different surface orientations that are populated throughout the simulation. Provided these different conformations of the analyte at the surface are sufficiently different with regards to their electronic structure, they will provide different theoretical responses to the sum frequency generation as determined through quantum chemical calculations. Once this is done, one could simply choose the conformation that provides the theoretical sum frequency generation spectrum that most closely matches the one obtained from experiments or one could fit the spectra using different ratios of the various conformations defined based on the molecular dynamics data. In this case, it would be possible to determine relative populations of the different conformations and thus provide a distribution of orientations of the analyte at the surface. This is the method that will be described in full using the example of leucine on polystyrene in Chapter 3. This system is perfect for this as it satisfies neither of the requirements necessary to perform the "Top Down" approach: there are many modes present in the spectra in the spectral region of interest and through an analysis of the atomic motions of each of the vibrations it is obvious that the modes are heavily coupled. The fact that this complicated system was still possible to be analyzed and an orientational distribution obtained caused this method to be named the "Bottom Up" approach, based on its more general applications.

Finally, to further the overall understanding of the systems that are being studied, it is necessary to focus not on the orientation of the individual molecules at the surface but upon the adsorbed layer of analyte molecules as a whole. These adsorbed layers have their own physical and optical properties and it is therefore necessary to determine these parameters. However, there is one more aspect of the adsorption of molecules to surfaces that one must study in order to obtain a more complete picture, specifically the kinetics of adsorption. To accomplish these goals, a method should be developed that is at once capable of taking high speed measurements resulting from the growing layer of adsorbed molecules and, once the adsorption process has reached equilibrium, determine the optical properties of the adsorbed film. To this end, a high speed Stokes polarimeter, capable of determining the changing Stokes parameters from a growing film would satisfy the initial requirement. In order to build this, it would be necessary to use photoelastic modulators that would allow for the determination of the Stokes parameters on a sub-second timescale. Additionally, since the chosen configuration for this system would involve two of these photoelastic modulators, it could be possible to function in another fashion as a Mueller matrix ellipsometer. This dual functionality would provide access to the complimentary information needed to support that which was obtained from sum frequency generation experiments and the aforementioned methods for determining surface orientation.

Chapter 2

Amino acid structure at a hydrophobic surface from nonlinear vibrational spectroscopy and electronic structure calculations [1]

2.1 Overview

Active research into the production of biocompatible polymers, anti-biofouling coatings, and biodegradable polymers as well as into the development of chromatographic systems capable of removing proteins from solution has spurred interest in the study of the interaction of proteins and peptides with polymer surfaces [17, 21–26, 38]. While these goals have have led to several advances in our understanding of protein adsorption, the basic atomic and molecular factors governing the interactions between the proteins and the surfaces are still not well understood. What is known, however, is that in addition to the nature of the protein itself, the chemistry and topography of the surface have a great effect upon the adsorbed geometry [6–8]. The immediate interfacial region between the solution and the polymer surface is of great interest as the interaction between the protein and the surface groups of the polymer can induce a change in the secondary and tertiary structure of the protein, resulting in a biological response [11]. These changes are generally more

---

[1] Reproduced in part with permission from Hall, S.; Hickey, A.; Hore, D. K. *J. Phys. Chem. C* **2010**, *114*, 9748–9757. Copyright 2010 American Chemical Society

pronounced in the case of hydrophobic surfaces where, once a protein has unfolded, it can then maximize hydrophobic interactions with the surface. These conformational changes may result in irreversible protein structural changes (denaturing) [12], or in an unforeseen reaction with their environment. The control of these effects would therefore be of great importance to the growing research arenas of biosensor development [32–34] and drug delivery systems [35–37].

While the study of protein adsorption to surfaces has been underway for several decades, it is made difficult by the complex nature of the proteins themselves. They are, inherently, large biomacromolecules composed of various regions with different chemical and physical properties that can undergo changes based on their environment. As a result, it is interesting to study the adsorption behaviour of engineered peptides and individual amino acids. Such studies remove a great deal of the complicating influence of the higher order structure of proteins, while still focusing on specific parts of the protein that can aid in explaining some basic interactions with surfaces during adsorption events. Amino acids therefore serve as structural markers for local adsorption sites in larger peptides and proteins. Adsorption of specific amino acids to various surfaces has been studied in a variety of methods, including electron microscopy [162], X-ray diffraction [52], spectrophotometry [55], and chromatography [59, 60].

While these methods provide valuable insight into one or more factors contributing to the adsorption process, they do possess inherent difficulties in achieving enough surface specificity for the *in situ* studies. Even-order nonlinear optical techniques are naturally selective of surface structures since they require a lack of centrosymmetry to produce signal; this symmetry requirement cannot be satisfied by molecules that are tumbling in solution. Among the second-order nonlinear techniques, visible-infrared sum-frequency generation (SFG) spectroscopy is particularly interesting since it probes surface vibrational modes. If one can target vibrational bands that can be related to specific chemical moieties of the amino acid on the surface, then structural information can be obtained without fluorescent- or radio-labelling. SFG spectroscopy has already proven to be useful in the study of amino acids [53, 80, 81], peptides [43, 83–85], and proteins [86–89] adsorbed at various liquid interfaces. If the experiment is performed using a combination of different beam polarizations, is it possible to extract multiple elements of the second-order susceptibility $\chi^{(2)}$ tensor. In addition, if the nonlinear optical properties of the molecule—all elements of its hyperpolarizability tensor $\alpha^{(2)}$—are known, then SFG spectra may be used to deduce the orientation of the functional groups that give rise to the response. There have been several illuminating accounts of this structural analysis in the literature [93–95].

While the route from measured spectra to deduced structure may seem straightforward, from a practical standpoint there are many obstacles which prevent this procedure from being carried out routinely for arbitrary molecules of interest. The heart of the SFG experiment that enables all subsequent quantitative analysis is obtaining spectra under different beam polarizations. The calibration involved in this procedure is nontrivial, and is paramount for structural analysis. Once the calibrated spectra are obtained, the next challenge involves fitting them to the correctly identified, participating vibrational modes, and extracting the associated amplitudes of the response. Establishing the width of the peaks is critical in this analysis, if the amplitudes are to be taken as a measure of the interfacial susceptibility. As a result of the coherent nature of SFG, the contribution of each vibrational mode can be positive or negative, and the resulting interferences often lead to misleading appearances of resonances in the spectra. Standard fitting routines are generally unreliable in such circumstances. As such it was necessary to work diligently to produce a fitting procedure that would be entirely uninfluenced by the initial parameters used and thus capable of always locating the global minimum within our parameter space. This was accomplished by the coupling of an error calculations based on randomly generated sets of parameters and a smart fitting routine that was applied only to a preselected number of the best sets of randomly generated parameters. Over a large enough number of runs, the trapped values converge to the global minimum. Finally, it remains a challenge to accurately describe the molecular response by estimating or evaluating the hyperpolarizability tensor elements associated with a particular vibrational mode. In simple cases, local symmetry may be considered to arrive at analytical expressions for $\alpha^{(2)}$ elements using bond-additivity models for the dipole and polarizability response [181–183]. However, often bond addivity models are insufficient to accurately describe the normal modes present. In such cases, quantum mechanical calculations may be used to yield estimates of $\alpha^{(2)}$ [100, 179, 184–186]. It was necessary to perform ab-initio calculations in an effective solvent model in order to predict these values as accurately as possible. In the present study, we investigate the interaction between L-phenylalanine (Phe) and polystyrene (PS). This system is of particular interest as it provides a situation wherein a relatively non-polar, aromatic amino acid adsorbs onto a hydrophobic surface. We illustrate approaches for fitting polarized SFG spectra, calculating molecular hyperpolarizabilities, and then relating microscopic to macroscopic quantities to arrive at the structure of Phe on PS. In the end, our results provide significant insight into the Phe-PS interaction. We have determined the Phe molecules to be in relatively narrow tilt and twist distributions, surprising since there is no immobilization through covalent or ionic interactions. We propose that this structure is due to the phenyl ring of Phe possibly being intercalated into the PS surface. Our evidence comes from our determination of the Phe phenyl ring tilt angle with respect to the previously-reported structure of phenyl rings at the aqueous-PS interface [190], together with our observed blue-shifts of the Phe CH_2 stretching modes.

2.2 Materials and Methods

Our visible-infrared SFG system (Ekspla, Lithuania) is based on a 10 Hz 30 ps Nd:YAG laser (Ekspla PL2241A). The visible beam in our experiment (fundamental 1064 nm frequency-doubled to 532 nm) has a diameter of 1 mm at the sample and an energy of 110 μJ/pulse. Infrared light tunable from 2700–3200 cm^{-1} (0.5 mm diameter at the sample,

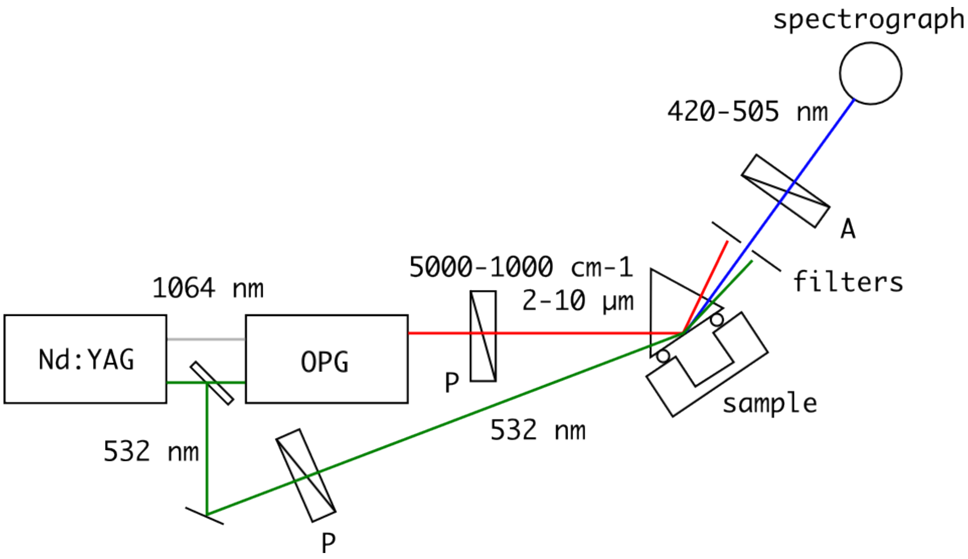

Figure 2.1: Schematic of SFG system used in all experiments.

200 μJ/pulse at 3000 cm^{-1}) is produced by difference frequency generation in $AgGaS_2$ by a parametric generator (Ekspla PG501). Beams approach the sample interface through a 68° CaF_2 dove prism (Del Mar Photonics, CA), incident at 66° visible and 64° infrared with respect to the prism-polymer interface. A schematic of our experimental SFG configuration is shown in Figure 2.1.

Prior to use, the prism was cleaned by dipping in a solution of 0.1 v/v% nitric acid in sulfuric acid, followed by copious rinsing in 18 MΩ deionized water (Nanopure, Barnstead Thermo). The three prism surfaces of interest were lightly polished using a 3 μm polycrystalline diamond suspension (Buehler Metadi supreme), followed by 0.05 μm silica suspension (Buehler Masterprep) and again rinsed with deionized water. Prior to assembling the sample cell, a deuterated d_8-polystyrene (MW 270 500 g/mol, PDI 1.25 from Polymer Source, QC) film was applied to the backside of the prism by spin coating (Model G3-8, Specialty Coating Systems, IN) from a 3 w/w% chloroform solution for 90 s at 1500 rpm, then drying covered overnight covered at room temperature. The polystyrene side of the prism was then pressed against a teflon cell with a fluoropolymer O-ring (Marco

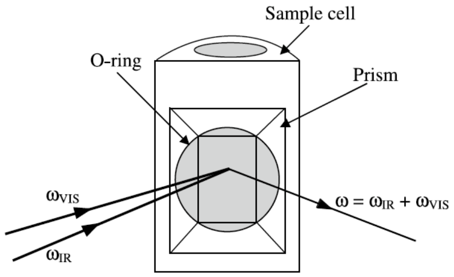

Figure 2.2: Schematic of our sample cell holder including a sample prism. Note that this shows the three beams involved in our experiment in the co-propagating SFG configuration

Rubber, NH). We have ensured that the cell and sample surface were clean by filling the cell with D_2O (Cambridge Isotope Labs) and acquiring SFG spectra from 2700–3200 cm^{-1}; no C-H stretching modes were observed. The liquid was then replaced with a 6.28 mg/mL solution of L-phenylalanine (Aldrich) in D_2O. A schematic diagram of our sample cell holder, including a prism as well as the input and output beams, is shown in Figure 2.2.

Spectra were acquired from 2700–3200 cm^{-1} with an ω_{IR} step size of 2 cm^{-1}, averaging 100 pulses at each step. We have performed the experiment in three polarization schemes, considering s- and p-polarized beams: ssp (SFG, visible, IR), sps, and ppp. Since our aim is to make quantitative comparisons between spectral features observed in these different polarization schemes, we have carefully calibrated the response of our system in different polarizations of the input and detected beams [191]. This procedure is performed for a variety of reasons, specifically the possible polarization biases of the various detectors present in the SFG system, the shape of the infrared radiation produced by the optical parametric generator, and the relationship between the response of the SFG system (represented by counts from a photomultiplier tube) and the actual energy of each of the beams present. The initial step in calibrating the system involves sending p- and s-polarized visible and infrared radiation through the system. These polarization states are initially calibrated by sending these beams to the sample holder and reflecting from a prism at Brewster's angle. Once s and p polarizations are known for these two beams it

wavelength /nm	polarization	energy /μ J	detector signal /counts
SFG	p	5.19	2050
532	s	6.45	3400
Vis	p	49.8	52
532	s	46.7	55
IR	p	203.5	210
3571	s	50.2	425
IR	p	206.8	215
3448	s	77.1	650
IR	p	203.9	200
3333	s	109.6	850
IR	p	206.4	210
3226	s	143.1	1150
IR	p	179.6	170
3125	s	141.2	1150

Table 2.1: Calibration data for various beams involved in the SFG system for the normalization of all detector counts with respect to the energy of the incident beams

is necessary to measure the number of counts detected by the SFG system with respect to the energy, measured by an energy meter (Coherent FieldmaxII). By comparing these two values we can determine the response, and preference if any exists, of the system to the individual polarization states and correct for it. Finally, for the calibration of the SFG radiation, it is necessary to leak in a small amount of green light from the 532 nm beam through the monochromator in order to obtain a certain number of counts from the photomultiplier tube. Similar to the IR and visible beams, the energy is measured just prior to the entry point of the monochromator in s and p polarizations. With these data it is possible to relate data obtained in different polarization states of the 3 beams without bias.

The values for the IR correction were determined using an average value over the range of interest. Finally, all amplitude values obtained from fitting the various spectra were corrected before being compared to values obtained from ab initio calculations. As an example for the ppp spectrum:

$$\mathrm{ppp_{corr}} = \frac{\mathrm{SFG_{p,J}}}{\mathrm{SFG_{p,D}}} \frac{\mathrm{vis_{p,J}}}{\mathrm{vis_{p,D}}} \frac{\mathrm{IR_{p,J}}}{\mathrm{IR_{p,D}}} \tag{2.1}$$

$$\mathrm{ppp}_{\mathrm{amp,corrected}} = \mathrm{ppp}_{\mathrm{corr}} \times \mathrm{ppp}_{\mathrm{amp}} \tag{2.2}$$

The ssp and sps values are corrected in a similar fashion. As a final point, a 532 nm half wave plate it placed just before the monochromator. This is to ensure that the light incident upon it are always at least somewhat p polarized. When the incident SFG beam is s polarized, the half wave plate is at 45° to the beam and if p-polarized it is at 0° in order to not affect the polarization. This is simply a result of the monochromator grating being designed for p-polarized light. Once all of these calibration procedures are completed it is necessary to obtain data from the spectra themselves in order to determine information regarding the orientation of the analyte at the surface.

2.3 Spectral Fitting

The intensity of the SFG signal is proportional to the product of the effective second order susceptibility $\chi^{(2)}_{\mathrm{eff}}$ and its complex conjugate.

$$I_{\mathrm{SFG}} \propto \chi^{(2)}_{\mathrm{eff}} \chi^{(2)*}_{\mathrm{eff}} = |\chi^{(2)}_{\mathrm{eff}}|^2 \tag{2.3}$$

The effective susceptibility is related to the actual susceptibility of the interface, $\chi^{(2)}$, by local field corrections, as will be described in more detail in the orientation analysis below. If we assume that these field corrections are dominated by the two bulk phases adjacent to the interface, then for the case of D_2O and d-PS we can neglect the dispersion of these corrections from 2700–3200 cm^{-1} since the refractive indices of D_2O and d-PS are essentially flat over this spectral region. As we tune the infrared beam from 2700–3200 cm^{-1}, individual elements of the $\chi^{(2)}$ tensor vary according to

$$\chi^{(2)}_{ijk}(\omega_{\mathrm{IR}}) = \chi^{(2)}_{\mathrm{NR},ijk} + \sum_{\nu} \frac{A_{\nu,ijk} e^{i\phi_\nu}}{\omega_\nu - \omega_{\mathrm{IR}} - i\Gamma_\nu} \tag{2.4}$$

where i, j, k are any of the laboratory x, y, z coordinates, with z normal to the interface and the beams incident along the positive x direction. $\chi^{(2)}_{\mathrm{NR}}$ is a non-resonant contribution;

the resonant terms arise from each vibrational normal mode ν that is excited during the ω_{IR} scan. We consider that each mode has a resonance frequency ω_ν, Lorentzian width Γ_ν, amplitude A_ν and possibly an additional phase contribution ϕ_ν. In the case of ssp and sps polarized spectra, we assume that the relative phase of the the modes is completely accounted for with $\phi_\nu = 0°$ or $180°$. To improve the efficiency of our fitting procedure we therefore simplify the numerator of the resonant terms in Equation 2.4 as $\pm A_{\nu,ijk}$. However, in the case of ppp polarization, our subsequent analysis (Equation 2.35) will reveal that this assumption no longer holds, and we must allow for an arbitrary phase between modes as written in Equation 2.4. This is because, even though the field corrections are without dispersion in the range 2700–3200 cm^{-1}, our total internal reflection geometry makes them complex. Since we do not know the relative contributions of all participating $\chi^{(2)}$ elements ahead of time, we cannot factor out the phase in a manner similar to ssp and sps.

Inspection of Equation 2.4 reveals some of the challenges associated with fitting the SFG line shape. Since this is a coherent spectroscopy, we must sum the contribution from all modes before evaluating the intensity using Equation 3.1. SFG spectra of phenylalanine adsorbed at the D_2O-perdeuterated polystyrene interface acquired under three polarization schemes are shown in Figure 2.3. Three resonances are immediately evident in the region 2800–3000 cm^{-1}. In order of decreasing energy, these are assigned to the CH_2 antisymmetric stretch (ν_{as}), CH_2 Fermi resonance and/or CH stretch, and CH_2 symmetric stretch (ν_{ss}). In general, optimization algorithms are subject to a trade-off between accuracy and efficiency: either they are exhaustive in their search over the whole parameter space (prohibitively slow for more than a few parameters), or they are 'smart', making decisions on how to crawl within this space (at the expense of falling into local minima). We are interested in determining the amplitude, position, and width of each of the resonances described above, in addition to the nonresonant amplitude. After attempting the fitting, we realized the necessity of including an extra contribution at 2750 cm^{-1} since the tail of the highest energy antisymmetric D_2O stretch protrudes into our region of interest. We

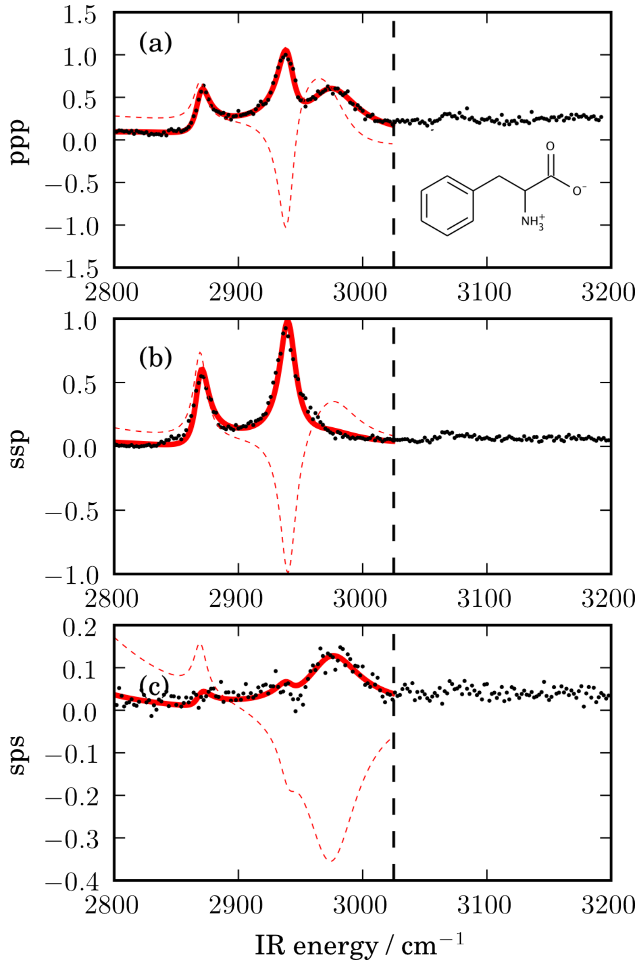

Figure 2.3: SFG spectra of phenylalanine adsorbed at the D_2O-perdeuterated polystyrene interface. (a) ppp, (b) ssp and (c) sps spectra (black points), together with fits to Equation 2.4 (solid red lines). Imaginary components of the line shape (shown with dashed red lines) most clearly indicate the relative phase between vibrational modes.

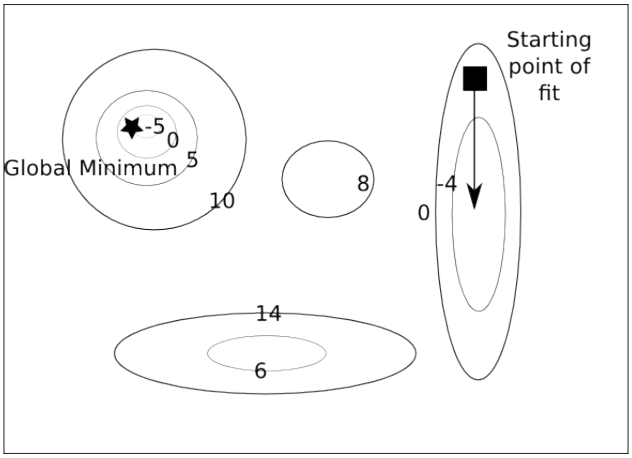

Figure 2.4: 2 dimensional example of a complex error space. This example demonstrates the pitfalls that exist in utilizing a “smart” fitting routine that is dependent upon the initial starting point for the fit. While this example shows a trapped minimum, it is a local minimum.

therefore have to determine at least 13 parameters from each spectrum: a nonresonant amplitude plus 3 parameters/mode × 4 modes. We now revisit the challenge associated with the phase of the numerator in Equation 2.4. In the ppp spectrum, we must also fit ϕ_ν which brings us to 4 parameters/mode and therefore 17 parameters in total. As can be seen in the graphical example in only 2 dimensions, Figure 2.4, starting in the incorrect initial position with a method that favours steepest descent will result in the incorrect minimum being determined.

We wish to explain that for ssp and sps spectra, although the simplification we have described ($A_\nu \exp(i\phi_\nu) \equiv \pm A_\nu$) reduces the number of parameters that must be determined in the fitting, it does not readily enable smart algorithms to arrive at the global minimum. A simple explanation considers progress in the fitting where the current trial amplitude for a given peak is, say, positive. An iterative procedure varies the position and width of this peak, along with all other parameters for the other peaks to arrive at the ‘best’ fit. The difference in R^2 between this solution and one where the amplitude for this peak is instead negative is often very small, especially considering the signal-to-noise ratio in SFG spectra without electronic resonance. In the case of ppp where there is an additional phase term, the situation is even worse, and most standard algorithms are generally unreliable. If there were only one or two resonances, a solution would be to repeat the fitting by selecting all possible combinations of phases as starting points in the parameter space. However, even for relatively simple spectra such those in Figure 2.3, this is not practical. We have developed a procedure to overcome this difficulty that may be applied to spectra with multiple peaks.

We begin by defining a parameter space bounded by maximum and minimum values for each amplitude, position, and width. The estimation of these boundaries for the positions can be inferred from the position of the peaks noted in the spectra themselves. This is true for the widths, but to a lesser extent, as the convolution of nearby peaks can cause either broadening or thinning of peaks as a result of constructive or destructive interference. Values for the boundaries of the amplitudes are determined by performing extremely rough error calculations and utilizing the results as a guide for the center of the boundary conditions. For the phase, no other knowledge than the normal boundaries of $-\pi$ and π of the phase parameter is needed. For ssp and sps spectra, each amplitude range spans positive and negative values. For ppp spectra, the amplitudes are restricted to positive numbers, and additional ranges are defined for $0^\circ < \phi_\nu < 360^\circ$. This is due to the fact that the actual response seen for ppp spectra is determined from not only the zzz element of the $\chi^{(2)}$ tensor, but from the xxz, xzx, and zxx elements as well. Since these values are multiplied by different, complex Fresnel coefficients, it is impossible to factor the phase term out and by doing so represent it simply as a sign. We then use a random number generator to pick a starting location in our parameter space and then determine the error based on these parameters. The resultant error is compared to a list of errors, and if it is lower than the greatest error on the list both it and its associated parameters are stored. Finally, after many runs the best parameters are sent to a final minimization using a bounded, constrained L-BFGS-B algorithm [192, 193]. The returned fitting parameters and

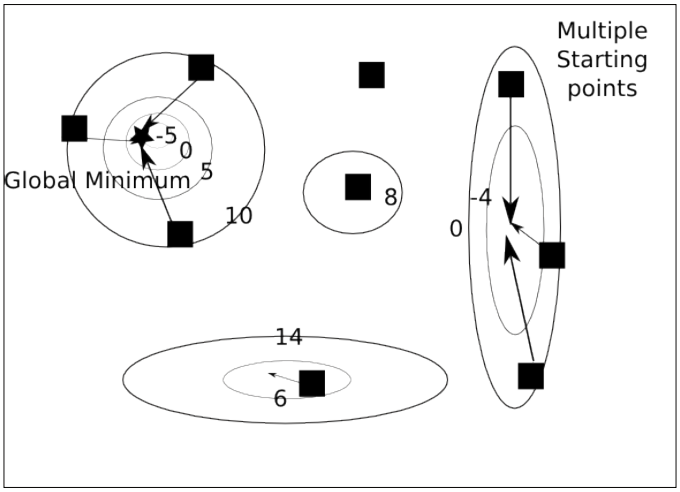

Figure 2.5: 2 dimensional example of a complex error space that has been studied by a complementary random approach to determining the initial parameters for a fitting search coupled with a "smart" fitting routine. While several starting points have trapped local minima, analysis of the output of this fitting routine would show, conclusively, the existence of the global minimum.

R^2 are stored, and the search is repeated using a new random location. The total number of iterations depends on the number of resonances in the spectrum; we have run a total of 10 000 times for each polarization scheme. At the end, the returned parameter list is sorted according to R^2 value and the best 10 solutions are inspected. Returning to the two dimensional example, Figure 2.5 shows visually the effect of using the random starting positions and trapping multiple minima. With these minimum values and their associated fit parameters stored, it would be obvious which runs had trapped the global minimum and which had not.

At this point, the parameters can be compared to the initial search parameters, and if any parameter in the space being analyzed has found a solution too close to one of the boundaries initially determined to be appropriate, the system is then rerun with a wider or shifted set of boundary conditions. This is vital to determining the true minimum solutions and not a solution that is still on a descending path through the parameter space and simply limited by the constraints. The entire fitting procedure is described graphically in 2.6. It

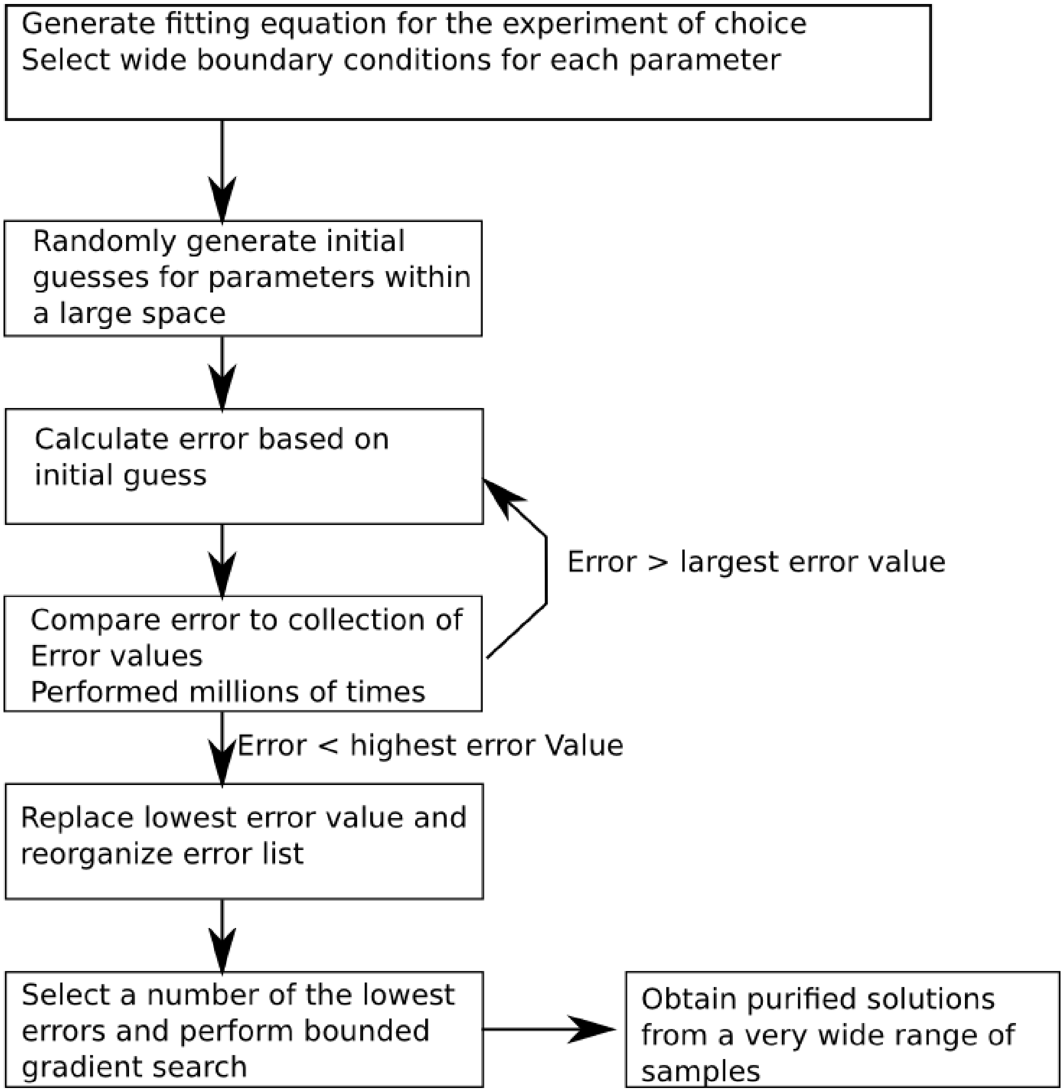

Figure 2.6: Graphical description of the fitting routine used to obtain spectral parameters. The use of random numbers to generate initial guesses within the parameter space results in a wide sampling of an appropriate range of values so as to avoid local minima. A bounded, smart fitting routine is then applied to the best solutions from the random starting points. The result is a collection of parameters that are reliably placed in the global minimum.

	Lower Bound	Upper Bound
NR Amplitude	-1	1
D_2O Amplitude	0	30
D_2O Position[1] /cm^{-1}	2750	2750
D_2O Width /cm^{-1}	0	200
D_2O Phase /rad	$-\pi$	π
CH_2 Symmetric Amplitude	0	30
CH_2 Symmetric Position /cm^{-1}	2860	2880
CH_2 Symmetric Width /cm^{-1}	0	25
CH_2 Symmetric Phase[2] /rad	0	0
Fermi Amplitude	0	30
Fermi Position /cm^{-1}	2930	2950
Fermi Width /cm-1	0	25
Fermi Phase /rad	$-\pi$	π
CH_2 Antisymmetric Amplitude	0	30
CH_2 Antisymmetric Position /cm^{-1}	2960	2980
CH_2 Antisymmetric Width /cm^{-1}	0	25
CH_2 Antisymmetric Phase /rad	$-\pi$	π

Table 2.2: Initial boundaries for the fitting of the ppp spectrum. [1] The position of the D_2O peak is set at its known position. [2] Since all phase is relative it is necessary to define the phase of a single peak, selected here to be the CH_2 Symmetric stretch

was most prudent to acquire fit parameters for the ppp spectrum first. This is due to the fact that in only that spectrum are all peaks present, those being the CH_2 symmetric and antisymmetric stretches as well as the Fermi/CH resonance. Specifically, if adequate fit parameters could be obtained for the ppp spectrum, it would be possible to fix several parameters in the fitting procedures for the ssp and sps spectra. Since the positions of the peaks and their widths are shared between the spectra, the only requirement would be to fit the nonresonant amplitude, the amplitude of the water peak at 2750 cm^{-1} and the amplitudes of each of the resonant peaks. As an example of the size of the ranges required for the initial search, the boundaries used in the initial fitting of the ppp spectrum are shown in Table 2.2. Since our spectra are relatively straightforward, these 10 solutions were all identical.[2] Values of the fitting parameters are displayed in Table 2.2.

---

[2] If fewer starting configurations are chosen, then the best 10 solutions will no longer be identical, and some will clearly have lower R^2 values than others.

	NR	D_2O	ν_{ss}	FR/CH	ν_{as}
ω_0 / cm^{-1}		2750	2869	2940	2974
Γ / cm^{-1}		67.5	6.4	8.0	25.8
$A_{ppp}/a.u.$	0.179	18.163	2.982	12.890	20.230
ϕ_{ppp} / rad		0.47	0.0	3.47	0.87
A_{ssp} / a.u.	0.057	14.174	4.331	-9.275	10.017
A_{sps} / a.u.	-0.097	18.699	0.724	-0.630	-9.657

Table 2.3: Parameters returned from fitting Equation 2.4 to the data presented in Figure 2.3. a.u. are arbitrary units.

Once the fit parameters for the ppp spectrum are obtained and the values of the positions and widths are set for the sps and ssp spectra, they can be calculated much faster. The only necessity is to alter the ranges for the latter two spectra to allow for positive and negative amplitudes prior to fitting. Once all of this has been performed, all necessary parameters from the spectra are obtained as presented in Table 2.3 in which fits to Equation 2.4 are indicated as solid lines in Figure 2.3.

2.4 Electronic structure calculations

In order to make the connection between the spectra and the orientation of the phenylalanine molecules, we require information about the molecular response (hyperpolarizability) of the observed CH_2 symmetric and antisymmetric stretching modes. Since the CH_2 Fermi resonance is expected to occur at the same frequency as the single C-H stretch, we assign these resonances as a single peak in the fitting, but do not use this peak for any quantitative analysis. We can explicitly state the dependence of the hyperpolarizability $\alpha^{(2)}$ on the infrared beam energy as

$$\alpha^{(2)}_{lmn}(\omega_{\rm IR}) = \alpha^{(2)}_{{\rm NR},lmn} + \sum_{\nu} \frac{a_{\nu,lmn}}{\omega_\nu - \omega_{\rm IR} - i\Gamma_\nu} \tag{2.5}$$

summing over all normal modes ν. Here we use l, m, and n as placeholders for any of the cartesian coordinates a, b, or c in the molecular frame. Figure 2.8 illustrates how the molecular coordinates are defined.

The numerator of each resonant term a_{lmn} is the product of the anti-Stokes Raman transition polarizability and the infrared transition dipole moment. Under the harmonic oscillator approximation, we can write these as derivatives of the linear polarizability $\alpha^{(1)}_{lm}$ and dipole moment μ_n with respect to the normal mode coordinate Q.

$$a_{lmn} \approx \frac{1}{2m\omega} \frac{\mathrm{d}\alpha^{(1)}_{lm}}{\mathrm{d}Q} \frac{\mathrm{d}\mu_n}{\mathrm{d}Q} \tag{2.6}$$

where ω is the frequency and m is the reduced mass of the normal mode under consideration. This provides a facile route for calculation; we use Equation 2.6 to determine all 27 elements of $\alpha^{(2)}$ for the CH_2 ν_{ss} and ν_{as} modes.

All calculations were performed at the B3LYP/6-31G(d,p) level. This functional and basis set has been demonstrated to reproduce gas-phase phenylalanine IR absorption spectra [194]. We begin with a geometry optimization of the zwitterionic form of phenylalanine. For use in predicting solvated properties, we perform our calculations with a polarizable continuum model (PCM) to approximate an aqueous environment. The GAMESS quantum chemistry package [187] was deployed on an Intel Xeon cluster. The optimized geometry was then used as input for a Hessian calculation. Inspecting the resulting normal modes, together with a frequency scaling factor of 0.9614 [195], we have identified our CH_2 stretching modes of interest. The eigenvectors of the Hessian provide the transformation from cartesian to normal mode coordinates. We have applied these transformations to all phenylalanine atoms to create 7 geometries for ν_{ss} and 7 geometries for ν_{as}. These correspond to 3 extensions along the corresponding normal mode coordinate ($Q = +1, +2, +3$), 3 compressions ($Q = -1, -2, -3$), and a geometry with equilibrium bond lengths ($Q = 0$). For each of these geometries, we have calculated all 9 elements of the polarizability tensor $\alpha^{(1)}_{lm}$ and 3 elements of the dipole moment vector μ_n. Figure 2.7 shows that these values are related by displacements along the normal mode, so the slope of the curves at $Q = 0$ then provides the derivatives required in Equation 2.6. Results of these calculations are plotted with points in Figure 2.7; solid lines indicate fits to a second-order

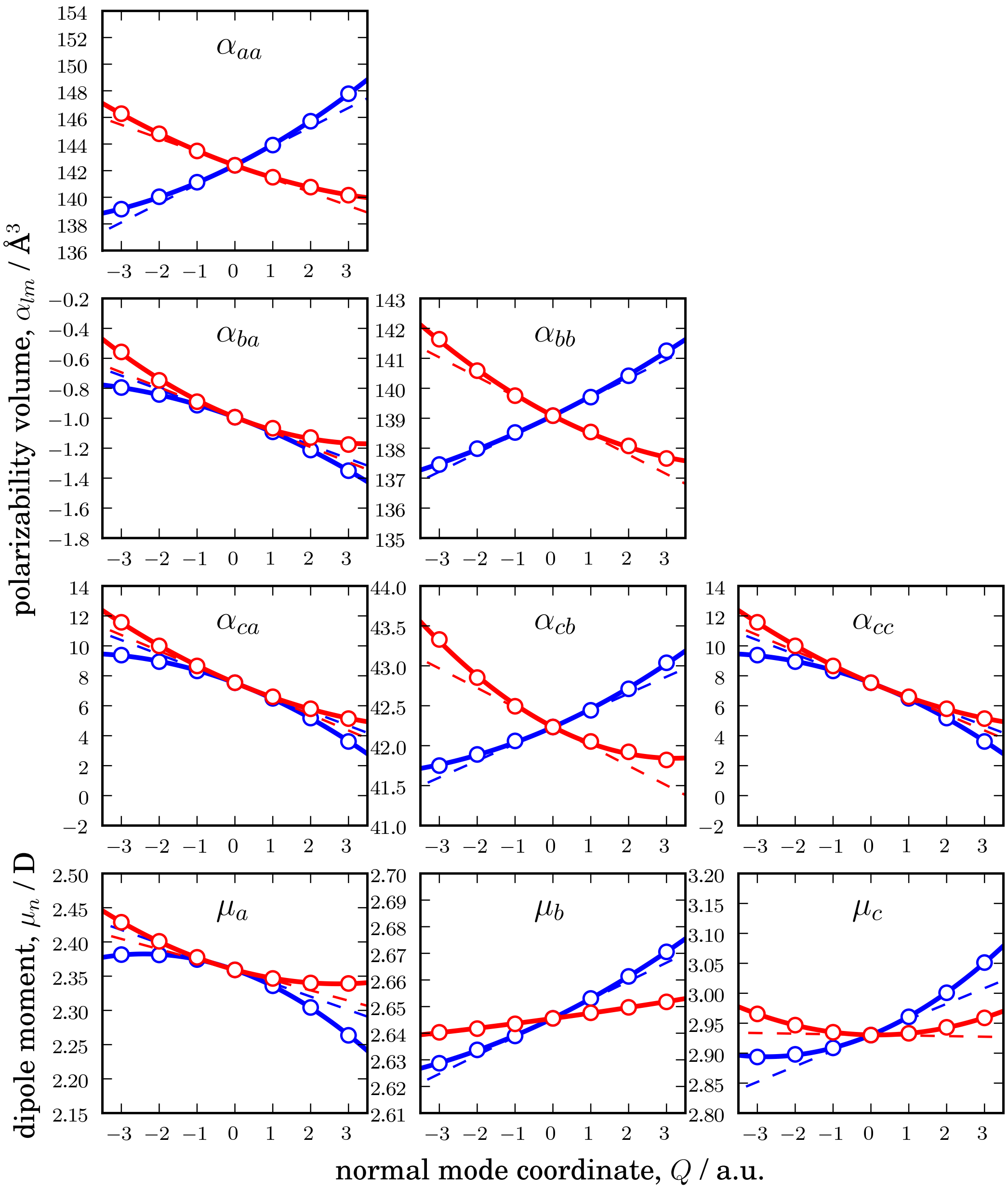

Figure 2.7: Elements of the polarizability tensor $\alpha_{lm}^{(1)}$ and dipole moment vector μ_n for the phenylalanine CH_2 symmetric stretch (blue) and anti-symmetric stretch (red) as a function of the normal mode coordinate, Q (a.u. are arbitrary units). The lmn coordinate system for the CH_2 moiety is illustrated in Figure 2.8. Since we are off-resonance for the Raman excitation, the polarizability tensor is symmetric and so only the lower triangular 6 elements are shown. Data plotted with circles are obtained from our calculation; solid lines indicate fits to a second-order polynomial; dashed lines are the derivatives about $Q = 0$.

$\partial/\partial Q$	ν_{ss}	ν_{as}
α_{aa}	1.4323	-1.0128
$\alpha_{ba}=\alpha_{ab}$	-0.0923	-0.0999
α_{bb}	0.6230	-0.6493
$\alpha_{ca}=\alpha_{ac}$	-0.9524	-1.0624
$\alpha_{cb}=\alpha_{bc}$	0.2103	-0.2438
α_{cc}	1.8221	-1.1865
μ_a	-0.01948	-0.01503
μ_b	0.00696	0.00194
μ_c	0.02609	-0.00103

Table 2.4: CH_2 polarizability and dipole moment derivatives (arbitrary units) obtained from the slopes in Figure 2.7.

polynomial; dashed lines are the derivatives about $Q = 0$. Results for ν_{ss} are shown in blue, and those for ν_{as} in red. Values of the derivatives are summarized in Table 2.4.

2.5 Implementation of Coordinate Transformation in the Phenylalanine Orientation Analysis

In order to determine the orientation distribution of phenylalanine adsorbed to the surface of polystyrene, it is necessary to compare theoretically determined parameters from ab initio calculations with the physical data, in this case the SFG spectra obtained. As stated previously, the derivatives of α and μ can be used to determine an approximation for the hyperpolarizability of a molecule undergoing a certain vibration, in turn allowing for a calculation of the value of $\chi^{(2)}$. In this case, the CH_2 and phenyl ring C—H stretching modes were studied. There is an obvious necessity to obtain that information in the same frame as that in which the SFG spectra were obtained, specifically the laboratory frame. The ab-initio calculations, performed in GAMESS, are done so in an arbitrary, frame of reference defined by the input data for the molecule in the calculation. While these calculations are extremely useful, this does make the information obtained not directly relevant to the SFG spectra. As an initial example, the transformation of the α and μ

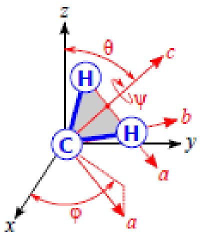

Figure 2.8: Definition of a coordinate system based entirely upon the CH_2 region of phenylalanine. Euler angles show the rotations about their respective axes relating the specific molecular frame, abc, to the laboratory frame, xyz.

derivatives for the CH_2 modes from the arbitrary initial frame to the laboratory frame will be described. It is therefore necessary to define a coordinate system based upon the CH_2 moiety.

As can be seen in Figure 2.8, the plane defined exclusively for the CH_2 modes, that can be understood as existing in an arbitrary three dimensional reference frame known to as abc. The physical properties found in this plane, specifically the α and μ derivatives for the symmetric and antisymmetric CH_2 stretches, can be related to the laboratory frame xyz in the same fashion as previously stated described. The three orthogonal vectors are defined as follows: a is defined as the vector traveling from one hydrogen through the other. This selection is arbitrary, but must be maintained throughout all calculations for self-consistency. The vector c is defined as emanating from the origin, defined by our carbon atom, and through the bisector of the two hydrogen atoms. The final vector, b is determined from the cross product of these two vectors.

What is necessary in this case is that the information originally in an arbitrary frame be encoded in the abc frame, so as to maintain homogeneity between all of our calculated values. This is done through the application of a “forward” DCM transformation, in which the initial ijk frame defined by the molecular input to the GAMESS program is rotated into the molecular frame, abc through Equation 1.36. Similarly, an “inverse” DCM transformation will be one in which an lmn frame is transformed into an ijk, or laboratory,

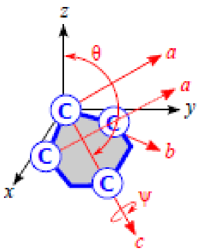

Figure 2.9: Definition of a coordinate system based entirely upon the phenyl region of phenlalanine. Euler angles show the rotations about their respective axes relating abc to xyz

frame.

Now that all of the necessary information is in a known frame, defined by the CH_2 region, it is possible to relate these theoretical data to our experimental data. This is done by performing the opposite "inverse" DCM transformation on the calculated derivatives. In fact, for the two Euler angles that are being used to relate the orientation of these modes to the SFG spectra, ψ and θ or the twist and tilt of the CH_2 plane respectively. The projected values of the derivatives were calculated at all possible values of ψ and θ, thus allowing for the determination of the values of ψ and θ that would result in spectra that matched those obtained through SFG measurements.

This procedure is repeated during the determination of the plausible structures of phenylalanine at the surface of polystyrene using the C—H modes resident upon the phenyl ring of phenylalanine, for which the abc frame was defined as follows:

In this case, the vector a is defined as traveling from one $meta$ carbon to the other. Much like in the case of the a vector for CH_2, this selection is arbitrary but must be maintained through all subsequent calculations. The c vector is defined as traveling from the origin, selected as the $ipso$ carbon, to the $para$ carbon. Finally, b is determined from the cross product of a and c. All ab-initio information is first transformed via "forward" DCM into the phenyl plane and then calculated in the lab from an "inverse" transformation. In this case, however, only the tilt value, θ was analyzed.

As an example of the application of this coordinate transformation, let us begin with the assumption that the α and μ derivatives are known in the desired molecular frame abc and we wish to project them into the lab frame, xyz, in order to calculate predicted SFG spectra. From the six vectors definine the two frames of reference, a, b and c as well as x, y and z, one can construct the DCM for the region of the molecule selected. This is possible since we know that the lab frame unit vectors are $x = [1, 0, 0]$, $y = [0, 1, 0]$, and $z = [0, 0, 1]$. We can calculate the direction cosine elements D_{qr} as the cosine of the angle between any two vectors q and r. In the case that these two vectors are a and x we have

$$\cos\theta_{ax} = \frac{a \cdot x}{|a||x|} = a \cdot x = x_1a_1 + x_2a_2 + x_3a_3. \tag{2.7}$$

Since x is a unit vector, we obtain $x \cdot a = a_1$. If we perform this operation for all 9 possible combinations of vectors between these two frames, we can determine all elements of the direction cosine matrix, D.

$$D = \begin{bmatrix} a_1 & b_1 & c_1 \\ a_2 & b_2 & c_2 \\ a_3 & b_3 & c_3 \end{bmatrix} \tag{2.8}$$

What is to be noted, however, is that the matrix defined in Equation 2.8 is equivalent to the “forward” direction cosine transformation matrix. Explicitly, this means that the multiplication of this matrix by any data of interest in the laboratory frame, xyz will return the data transformed into the molecular frame, abc. Since we desire the reverse transformation, it is necessary to use the inverted form of this matrix, or the “inverse” DCM.

$$D^{-1} = \begin{bmatrix} a_1 & a_2 & a_3 \\ b_1 & b_2 & b_3 \\ c_1 & c_2 & c_3 \end{bmatrix} \tag{2.9}$$

As an example the transformation of the dipole derivatives from a molecular frame in which they are known to the desired laboratory frame will be shown.

$$\begin{bmatrix} \partial\mu_x/\partial Q \\ \partial\mu_y/\partial Q \\ \partial\mu_z/\partial Q \end{bmatrix} = \begin{bmatrix} a_1 & a_2 & a_3 \\ b_1 & b_2 & b_3 \\ c_1 & c_2 & c_3 \end{bmatrix} \begin{bmatrix} \partial\mu_a/\partial Q \\ \partial\mu_b/\partial Q \\ \partial\mu_c/\partial Q \end{bmatrix} \tag{2.10}$$

As a specific example, the value of the dipole derivative in the x direction is determined through

$$\frac{\partial\mu_x}{\partial Q} = \sum_{k}^{a,b,c} D^{-1}_{xk} \frac{\partial\mu_k}{\partial Q} \tag{2.11}$$

for the all values of a, b, and c.

The transformation of the polarizability derivatives is slightly more complex, based on the fact that the information encoded in them relates information based upon two different axes, as represented by the 3×3 matrix the information is presented in. For this it is necessary to perform the following calculation for each element of the alpha matrix. This is shown in Equation 2.12 using Einstein notation for the correct multiplication of the matrix of α derivatives by the DCM. Einstein notation is a simple representation of summations for which each index is summed over the values defined by a, b, and c. Ultimately, 9 elements of the matrix of α derivatives are transformed to the molecular abc frame from the laboratory xyz frame.

$$\frac{\partial\alpha_{xy}}{\partial Q} = \sum_{l}^{a,b,c} \sum_{m}^{a,b,c} D^{-1}_{xl} D^{-1}_{ym} \frac{\partial\alpha_{lm}}{\partial Q} \tag{2.12}$$

Following this transformation, which leaves the information in the laboratory frame, it is possible to use the α and μ derivatives to predict SFG spectral responses. Specifically regarding rank 2 tensors, such as the matrix of α derivatives, it is possible to apply another method to transform these values from one coordinate system to another, as defined in [179]. What is necessary is the multply the transpose of the DCM as defined per the desired transformation (forward or inverse) multipied by the matrix of α derivatives and finally multiplied by the DCM. In this case, the DCM used to transform the values of the α derivatives from the molecular frame to the laboratory frame is the inverse DCM.

$$\begin{bmatrix} \partial\alpha_{xx}/\partial Q & \partial\alpha_{xy}/\partial Q & \partial\alpha_{xz}/\partial Q \\ \partial\alpha_{yz}/\partial Q & \partial\alpha_{yy}/\partial Q & \partial\alpha_{yz}/\partial Q \\ \partial\alpha_{zx}/\partial Q & \partial\alpha_{zy}/\partial Q & \partial\alpha_{zz}/\partial Q \end{bmatrix} = D^T \begin{bmatrix} \partial\alpha_{aa}/\partial Q & \partial\alpha_{ab}/\partial Q & \partial\alpha_{ac}/\partial Q \\ \partial\alpha_{ba}/\partial Q & \partial\alpha_{bb}/\partial Q & \partial\alpha_{bc}/\partial Q \\ \partial\alpha_{ca}/\partial Q & \partial\alpha_{cb}/\partial Q & \partial\alpha_{cc}/\partial Q \end{bmatrix} D \tag{2.13}$$

In this case, the inverse transformation includes an orientational distribution function, which is discussed later in this chapter. Conversely, should the information originally be known in the laboratory frame, the application of a "forward" coordinate transformation using D should be applied in a similar fashion. These definitions of D, "forward", D^{-1}, "inverse" transformations are used throughout Chapters 2 and 3.

2.6 CH_2 Plane Orientation Analysis

Now that the information regarding the molecular response has been calculated, in terms of the approximated hyperpolarizability, it is necessary to determine how this can be related to the spectra that were obtained. It is therefore necessary to rotate the hyperpolarizabilities from the molecular frame into the laboratory frame. As can be seen in Figures 2.8 and 2.9, the CH_2 and phenyl rings define coordinate systems that must be rotated through an Euler transformation in order to be assessed in the laboratory frame.

A second necessity exists, now that the hyperpolarizabilities are available in the laboratory coordinate system, for their values to be related to that which actually determines the responses of the individual modes seen in the spectra obtained. This macroscopic response, or the macroscopic second-order susceptibility $\chi^{(2)}$ is related to the microscopic second-order polarizability (hyperpolarizability) $\alpha^{(2)}$ through

$$\chi^{(2)}_{ijk} = \frac{N}{\epsilon_0}\langle \alpha^{(2)}_{lmn} \rangle. \tag{2.14}$$

where N is the surface number density, ε_0 is the vacuum permittivity, and the angular brackets denote an average over all molecular orientations present at the interface. Now that we have determined the ensemble amplitudes A_{ijk} in Equation 2.4 from fitting the SFG spectra, and the molecular amplitudes a_{lmn} in Equation 2.14 from calculation, we are ready the relate these quantities and thereby arrive at the orientation distribution for phenylalanine adsorbed at the aqueous–polystyrene interface. Equation 2.14 may be simplified by considering these amplitudes directly

$$A_{ijk} = \frac{N}{\varepsilon} \langle a_{ijk}(\theta, \phi, \psi) \rangle \tag{2.15}$$

for each vibrational mode under consideration, where A_{ijk} and a_{ijk} are defined in eqs 2.4 and 3.3. A prerequisite is the projection of the microscopic response a_{lmn} into the laboratory ijk frame. This is accomplished by a coordinate transformation, thereby introducing the Euler angles θ for the tilt of the CH$_2$ c-axis with respect to the surface normal, ϕ for the azimuthal orientation, and ψ for the twist of the CH$_2$ plane about the molecular c axis. These angles are illustrated in Figure 2.8. We project into the laboratory frame via

$$a_{ijk}(\theta, \phi, \psi) = \sum_{l,m,n} D^{-1}_{il}(\theta, \phi, \psi) D^{-1}_{jm}(\theta, \phi, \psi) D^{-1}_{kn}(\theta, \phi, \psi) a_{lmn} \tag{2.16}$$

where D^{-1} is the inverse direction cosine matrix.

We now represent the ensemble average by an orientation distribution function. For generality, we choose a function that describes a uniform distribution in ϕ, and Gaussian distribution in both θ and ψ.

$$f^{\mathrm{CH2}}_{\mathrm{ODF}} = \exp\left[-\frac{(\theta - \theta_0^{\mathrm{CH2}})^2}{2(\sigma_\theta^{\mathrm{CH2}})^2} - \frac{(\psi - \psi_0^{\mathrm{CH2}})^2}{2(\sigma_\psi^{\mathrm{CH2}})^2} \right]. \tag{2.17}$$

A uniform ϕ distribution is reasonable since our polymer-water interface is isotropic with respect to azimuthal rotation (no macroscopic ordering in the xy plane). We therefore describe our orientation distribution with four parameters: the mean tilt θ_0^{CH2} and twist ψ_0^{CH2} of phenylalanine's CH$_2$ plane, and the corresponding widths ($\sigma_\theta^{\mathrm{CH2}}$, $\sigma_\psi^{\mathrm{CH2}}$) of the tilt and twist distributions. Our final expression of Equation 2.15 is now

$$\begin{aligned} A_{ijk}(\theta_0^{\mathrm{CH2}}, \sigma_\theta^{\mathrm{CH2}}, \psi_0^{\mathrm{CH2}}, \sigma_\psi^{\mathrm{CH2}}) =& \frac{N}{C\varepsilon} \int_0^{2\pi} \int_0^{2\pi} \int_0^{\pi} f^{\mathrm{CH2}}_{\mathrm{ODF}}(\theta, \psi; \theta_0^{\mathrm{CH2}}, \sigma_\theta^{\mathrm{CH2}}, \psi_0^{\mathrm{CH2}}, \sigma_\psi^{\mathrm{CH2}}) \\ & \times a_{ijk}(\theta, \phi, \psi)\ \sin\theta \ \mathrm{d}\theta \ \mathrm{d}\phi \ \mathrm{d}\psi \end{aligned} \tag{2.18}$$

where C is a normalization constant

$$C = \int_0^{2\pi}\int_0^{2\pi}\int_0^{\pi} f_{\mathrm{ODF}}^{\mathrm{CH2}}(\theta, \psi; \theta_0^{\mathrm{CH2}}, \sigma_\theta^{\mathrm{CH2}}, \psi_0^{\mathrm{CH2}}, \sigma_\psi^{\mathrm{CH2}})\ \sin\theta\ \mathrm{d}\theta\ \mathrm{d}\phi\ \mathrm{d}\psi. \tag{2.19}$$

We are now ready to make the connection to our experimental measurements. For direct comparison with the results of fitting SFG spectra acquired under different beam polarizations, we can construct effective peak amplitudes corresponding to a specific polarization scheme. For a trial set of $(\sigma_\theta^{\mathrm{CH2}}, \sigma_\psi^{\mathrm{CH2}})$, the ssp amplitude is given by

$$A_{\mathrm{ssp}}(\theta_0^{\mathrm{CH2}}, \psi_0^{\mathrm{CH2}}) = L_y A_{yyz}(\theta_0^{\mathrm{CH2}}, \psi_0^{\mathrm{CH2}}) K_y K_z \tag{2.20}$$

where the K and L factors are the linear and nonlinear macroscopic field corrections defined in Ref 70. Specifically the K factors relate the electric field vectors at the surface, as opposed to those moving through a vacuum. The relationship between these two fields are described as

$$E_x = E_x\hat{x} = \pm E_p^I \cos\theta_I (1 - r_p)\hat{x} = K_x E_p^I \hat{x} \tag{2.21}$$

$$E_y = E_y\hat{y} = (1 + r_s)E_s^I \hat{y} = K_y E_s^I \hat{y} \tag{2.22}$$

$$E_z = E_z\hat{z} = \pm E_p^I \sin\theta_I (1 + r_p)\hat{x} = K_z E_p^I \hat{z} \tag{2.23}$$

where

$$K_x = \pm\cos\theta_{\mathrm{I}}(1 - r_p) = \pm\frac{2n_{\mathrm{I}}\cos\theta_{\mathrm{I}}\cos\theta_{\mathrm{T}}}{n_{\mathrm{I}}\cos\theta_{\mathrm{T}} + n_{\mathrm{T}}\cos\theta_{\mathrm{T}}} \tag{2.24}$$

$$K_y = (1 + r_s) = \frac{2n_{\mathrm{I}}\cos\theta_{\mathrm{I}}}{n_{\mathrm{I}}\cos\theta_{\mathrm{I}} + n_{\mathrm{T}}\cos\theta_{\mathrm{T}}} \tag{2.25}$$

$$K_z = \sin\theta_{\mathrm{I}}(1 + r_p) = \frac{2n_{\mathrm{I}}\sin\theta_{\mathrm{I}}\cos\theta_{\mathrm{I}}}{n_{\mathrm{I}}\cos\theta_{\mathrm{T}} + n_{\mathrm{T}}\cos\theta_{\mathrm{I}}}. \tag{2.26}$$

While the K factors account for variations between the electric fields at the surface and those traveling through space, the L factors account for the generation of sum-frequency electric fields from the induced polarization at the surface. The non-linear induced polarization generates these surface based electric fields from which the emitted light exits at a specific angle in order to satisfy phase matching conditions. Ultimately these factors are required to accurately describe the relationship between the electric field of the excident sum-frequency beam and that of the induced polarization at the surface.

$$\mathbf{E_{i,SF}} = \mathbf{L_i P^{(2)}_{i,SFG}} \tag{2.27}$$

There are 6 of these L factors, three for reflection and transmission

$$L_x^R = -\frac{\mathrm{i}\omega_{\mathrm{SF}}}{c\varepsilon_0} \frac{\cos\theta_{\mathrm{SF}}^{\mathrm{T}}}{n_{\mathrm{T}}\cos\theta_{\mathrm{SF}}^{\mathrm{I}} + n_{\mathrm{I}}\cos\theta_{\mathrm{SF}}^{\mathrm{T}}} \tag{2.28}$$

$$L_y^R = \frac{\mathrm{i}\omega_{\mathrm{SF}}}{c\varepsilon_0} \frac{1}{n_{\mathrm{I}}\cos\theta_{\mathrm{SF}}^{\mathrm{I}} + n_{\mathrm{T}}\cos\theta_{\mathrm{SF}}^{\mathrm{T}}} \tag{2.29}$$

$$L_z^R = \frac{\mathrm{i}\omega_{\mathrm{SF}}}{c\varepsilon_0} \frac{n_{\mathrm{T}} n_{\mathrm{layer}} \sin\theta_{\mathrm{SF}}^{\mathrm{T}}}{n_{\mathrm{I}}\cos\theta_{\mathrm{SF}}^{\mathrm{T}} + n_{\mathrm{T}}\cos\theta_{\mathrm{SF}}^{\mathrm{I}}} \tag{2.30}$$

$$L_x^T = \frac{\mathrm{i}\omega_{\mathrm{SF}}}{c\varepsilon_0} \frac{\cos\theta_{\mathrm{SF}}^{\mathrm{I}}}{n_{\mathrm{T}}\cos\theta_{\mathrm{SF}}^{\mathrm{I}} + n_{\mathrm{I}}\cos\theta_{\mathrm{SF}}^{\mathrm{T}}} \tag{2.31}$$

$$L_y^T = \frac{\mathrm{i}\omega_{\mathrm{SF}}}{c\varepsilon_0} \frac{1}{n_{\mathrm{I}}\cos\theta_{\mathrm{SF}}^{\mathrm{I}} + n_{\mathrm{T}}\cos\theta_{\mathrm{SF}}^{\mathrm{T}}} \tag{2.32}$$

$$L_z^T = \frac{\mathrm{i}\omega_{\mathrm{SF}}}{c\varepsilon_0} \frac{n_{\mathrm{T}} n_{\mathrm{layer}} \sin\theta_{\mathrm{SF}}^{\mathrm{T}}}{n_{\mathrm{I}}\cos\theta_{\mathrm{SF}}^{\mathrm{T}} + n_{\mathrm{T}}\cos\theta_{\mathrm{SF}}^{\mathrm{I}}}. \tag{2.33}$$

From these factors and incident electric fields, the intensity of the SF signal can be determined.

Unit polarization vectors are contained in these definitions of K and L. Similarly, for a given $(\sigma_\theta^{\mathrm{CH2}}, \sigma_\psi^{\mathrm{CH2}})$, we have for our cases, those being sps, ssp, and ppp

$$A_{\mathrm{sps}}(\theta_0^{\mathrm{CH2}}, \psi_0^{\mathrm{CH2}}) = L_y A_{yzy}(\theta_0^{\mathrm{CH2}}, \psi_0^{\mathrm{CH2}}) K_z K_y \tag{2.34}$$

and

$$\begin{aligned} A_{\mathrm{ppp}}(\theta_0^{\mathrm{CH2}}, \psi_0^{\mathrm{CH2}}) &= L_x A_{xxz}(\theta_0^{\mathrm{CH2}}, \psi_0^{\mathrm{CH2}}) K_x K_z + L_x A_{xzx}(\theta_0^{\mathrm{CH2}}, \psi_0^{\mathrm{CH2}}) K_z K_x \\ &+ L_z A_{zxx}(\theta_0^{\mathrm{CH2}}, \psi_0^{\mathrm{CH2}}) K_x K_x + L_z A_{zzz}(\theta_0^{\mathrm{CH2}}, \psi_0^{\mathrm{CH2}}) K_z K_z. \end{aligned} \tag{2.35}$$

Starting by considering a narrow distribution in tilt and twist, with $\sigma_\theta = \sigma_\psi = 2°$. It is then necessary to calculate the ssp, sps, and ppp amplitudes for the CH_2 symmetric stretch as a function of θ_0^{CH2} and ψ_0^{CH2} according to eqs 2.20–2.35. The calculated amplitude of the CH_2 symmetric stretch is projected into the lab frame according to all possible combinations of mean tilt θ_0^{CH2} and twist ψ_0^{CH2} angles for this Gaussian distribution in the lab frame. From these amplitudes we apply the macroscopic local field corrections and determine the corresponding amplitudes that would be observed upon fitting spectra obtained in each of the three polarization schemes. This is the reason we have performed such a careful calibration of our intensity when the polarization of the beams are changed in our experiment. We have repeated the above steps for the CH_2 antisymmetric stretch, and have then determined the ratios $(A_{\mathrm{ssp}}/A_{\mathrm{ppp}})_{\mathrm{ss}}$, $(A_{\mathrm{ssp}}/A_{\mathrm{ppp}})_{\mathrm{as}}$, and $(A_{\mathrm{sps}}/A_{\mathrm{ppp}})_{\mathrm{as}}$. These ratios were chosen based on the signal-to-noise level in the corresponding experimental spectra. This entire procedure was then repeated for widths of the tilt and twist distribution, with $\sigma_\theta^{\mathrm{CH2}}$ and $\sigma_\psi^{\mathrm{CH2}}$ each ranging from 2–70° in steps of 2°. A representative map of these ratios as a function of θ_0^{CH2} and ψ_0^{CH2} appears in Figure 2.10. The green highlighted regions indicate the intersection of the contours with the experimental amplitude ratios. Although the individual maps contain a large number of $(\theta_0^{\mathrm{CH2}}, \psi_0^{\mathrm{CH2}})$ possibilities consistent with the experimental data, the intersection of results from all maps returns a limited set of possibilities, indicated by the red dots in Figure 2.10. Our Gaussian width parameter space is shown in Figure 2.11. The grey and black regions indicate widths for which there was a solution $(\theta_0^{\mathrm{CH2}}, \psi_0^{\mathrm{CH2}})$ in agreement with the experimental CH_2 amplitude ratios, *ie.* intersections between the green contours in all such version of Figure 2.10 for the various combinations of ODF$^{\mathrm{CH2}}$ widths. In Figure 2.12 we visualize all the solutions of $(\theta_0^{\mathrm{CH2}}, \psi_0^{\mathrm{CH2}})$ that result from the shaded regions of Figure 2.11. The grey and black colors indicate solutions from the corresponding grey and black regions of Figure 2.11.

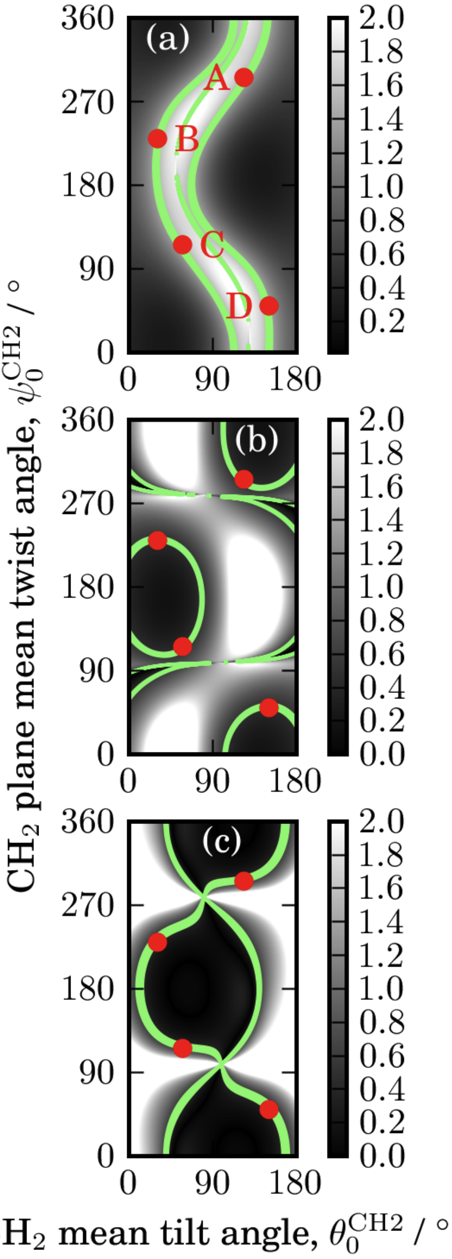

Figure 2.10: These maps show the expected ratio of amplitudes corresponding to (a) $A_{\mathrm{ssp}}/A_{\mathrm{ppp}}$ for ν_{ss}, (b) $A_{\mathrm{ssp}}/A_{\mathrm{ppp}}$ for ν_{as}, (c) $A_{\mathrm{sps}}/A_{\mathrm{ppp}}$ for ν_{as} for the case of $(\sigma_\theta^{\mathrm{CH2}} = 10^\circ, \sigma_\psi^{\mathrm{CH2}} = 8^\circ)$ about the mean values θ_0^{CH2} and ψ_0^{CH2}. Contours highlighted in green correspond to experimentally-determined ratios obtained from fitting the spectra. Red points indicate the tilt and twist angles for which intersection occur between all three maps. Such maps were constructed for all distribution widths in order to search for intersection with experimental values.

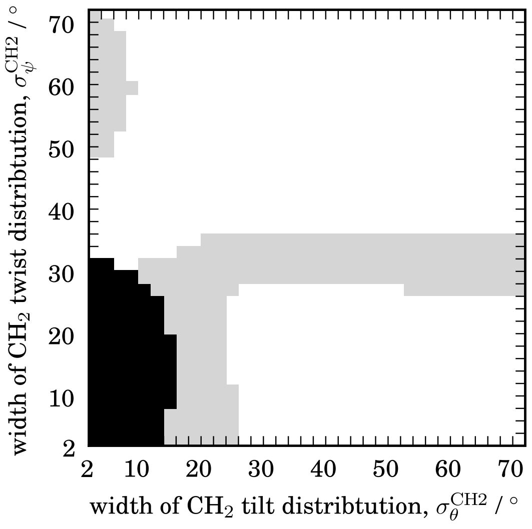

Figure 2.11: Values of the CH$_2$ tilt distribution *width* and twist distribution *width* for which there is an orientation distribution in agreement with amplitudes of CH$_2$ modes in experimental spectra (grey and black together). White regions indicate that no solution is possible. The subset of black points indicates those solutions that are also consistent with the experimentally-observed aromatic C–H stretching mode intensities, as discussed in Section 2.7.

This distinction between these two regions will be discussed in Section 2.7. The four representative points as identified in Figure 2.10 are highlighted, their values are listed in Table 2.5, and their orientations are depicted in Figure 2.13.

2.7 Phenyl Ring Orientation Analysis

Figure 2.3 reveals that the intensity of the aromatic C-H stretching region (3000–3200 cm^{-1}) is very low compared to the aliphatic modes. In addition, the aromatic region

structure	θ_0^{CH2} /°	ψ_0^{CH2} /°	θ_0^{Ph} /°
A	123	296	159
B	30	230	78
C	57	116	21
D	150	50	102

Table 2.5: Values of the CH$_2$ tilt (θ_0^{CH2}) and twist (ψ_0^{CH2}) angles, and the corresponding ring tilt angle (θ_0^{Ph}) for each of the representative structures identified in Figure 2.10.

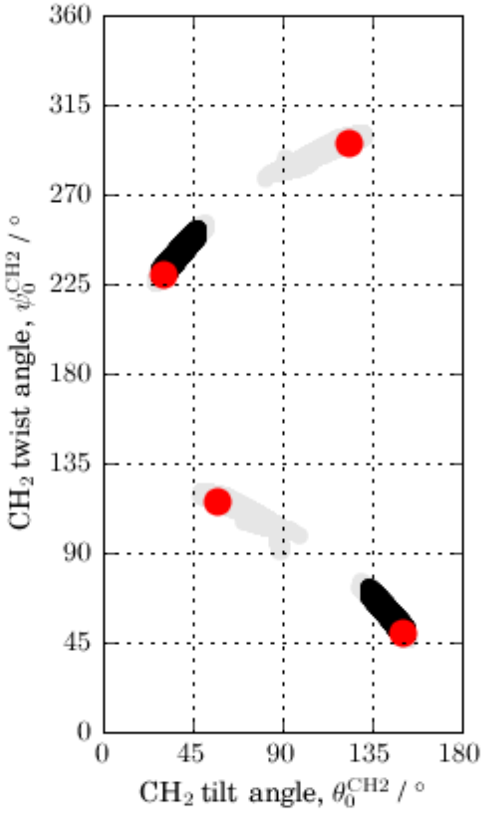

Figure 2.12: Values of the CH$_2$ mean tilt θ_0^{CH2} and twist ψ_0^{CH2} angles that are in agreement with experimental data, obtained by considering all orientation distribution widths in the range $2^\circ < (\sigma_\theta^{\mathrm{CH2}}, \sigma_\psi^{\mathrm{CH2}}) < 70^\circ$. Together, grey and black solutions are in agreement with the experimental CH$_2$ amplitudes; the subset of black solutions are additionally in agreement with the experimental aromatic C–H stretching amplitudes.

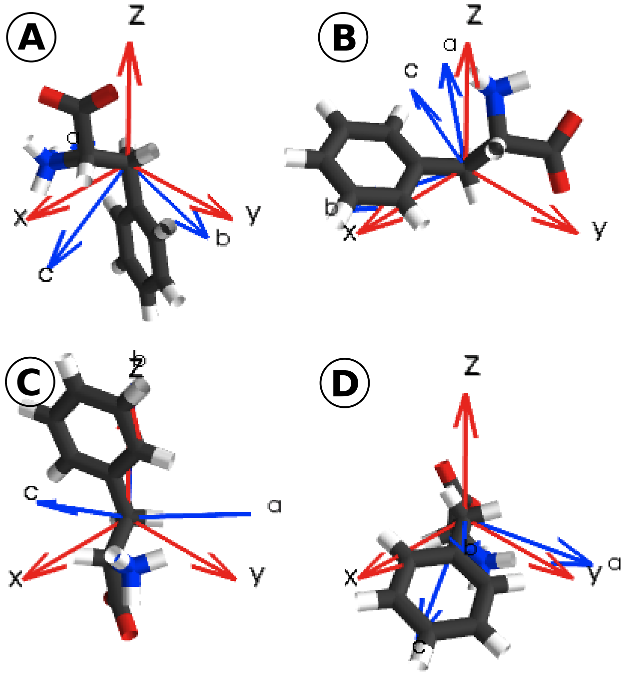

Figure 2.13: Representative orientations of phenylalanine adsorbed at the aqueous–polystyrene interface that are consistent with the CH_2 modes in experimental spectra. Structures are labelled according to their designation in Figure 2.10 and Table 2.5. Lab frame xyz unit vectors are drawn in red; molecular CH_2 frame abc unit vectors are drawn in blue.

$\partial/\partial Q$	ν_{20a}	ν_{7a}	ν_{7b}	ν_{20b}	ν_2
α_{aa}	0.9975	2.8050	-1.2987	-0.6904	-3.0919
$\alpha_{ba} = \alpha_{ab}$	-0.0396	-0.0738	-0.0170	-0.0685	-0.0757
α_{bb}	0.0563	0.0844	-0.1008	0.0373	-0.1796
$\alpha_{ca} = \alpha_{ac}$	1.4950	-0.6222	1.7851	0.0872	-0.7348
$\alpha_{cb} = \alpha_{bc}$	-0.0181	0.0495	0.0464	0.0273	-0.0297
α_{cc}	0.4573	-0.1614	-1.5186	2.3733	-2.408
μ_a	-0.01645	-0.02683	0.00311	-0.02230	-0.02313
μ_b	0.00084	0.00104	-0.00030	-0.00044	-0.00130
μ_c	-0.02051	-0.00061	0.00717	0.02789	-0.01831

Table 2.6: Aromatic polarizability and dipole moment derivatives (arbitrary units) obtained from the slopes in Figure 2.14.

is relatively featureless, preventing us from fitting distinct peaks. However, we know from isotropic infrared and Raman spectra that there are five aromatic C–H stretching modes with relatively strong intensity. These are ν_{20a} expected at 3063 cm^{-1}, ν_{7a} at 3003 cm^{-1}, ν_{7b} at 3030 cm^{-1}, ν_{20b} at 3029 cm^{-1}, and ν_2 at 3055 cm^{-1}, and have been observed in SFG studies of other aromatic molecules [186, 190, 196]. This low aromatic C–H stretching intensity must therefore be due to the orientation that Phe adopts on the PS surface. We aim to utilize this information to possibly narrow down the range of solutions presented in Figures 2.11 and 2.12. We start by defining our aromatic coordinate system as shown in Figure 2.9, with the c axis running from the ipso carbon to the para carbon; a perpendicular to this axis and going through two phenyl carbon atoms. The phenyl ring is therefore in the ac-plane. The local b axis points out the plane of the ring. In this coordinate system, we then calculate 9 elements of the polarizability tensor derivative $\partial\alpha^{(1)}_{lm}/\partial Q$ and 3 elements of the dipole moment derivative $\partial\mu_n/\partial Q$ for each of the five aromatic C-H ring modes. This determination is illustrated in Figure 2.14; results are summarized in Table 2.6.

Since we cannot robustly fit any of these peaks to proceed as in the previous section, we instead work back to simulate the amplitude of the 5 aromatic modes with respect to CH$_2$ ν_{ss} in each experimental polarization scheme. For this we have assumed no preference for

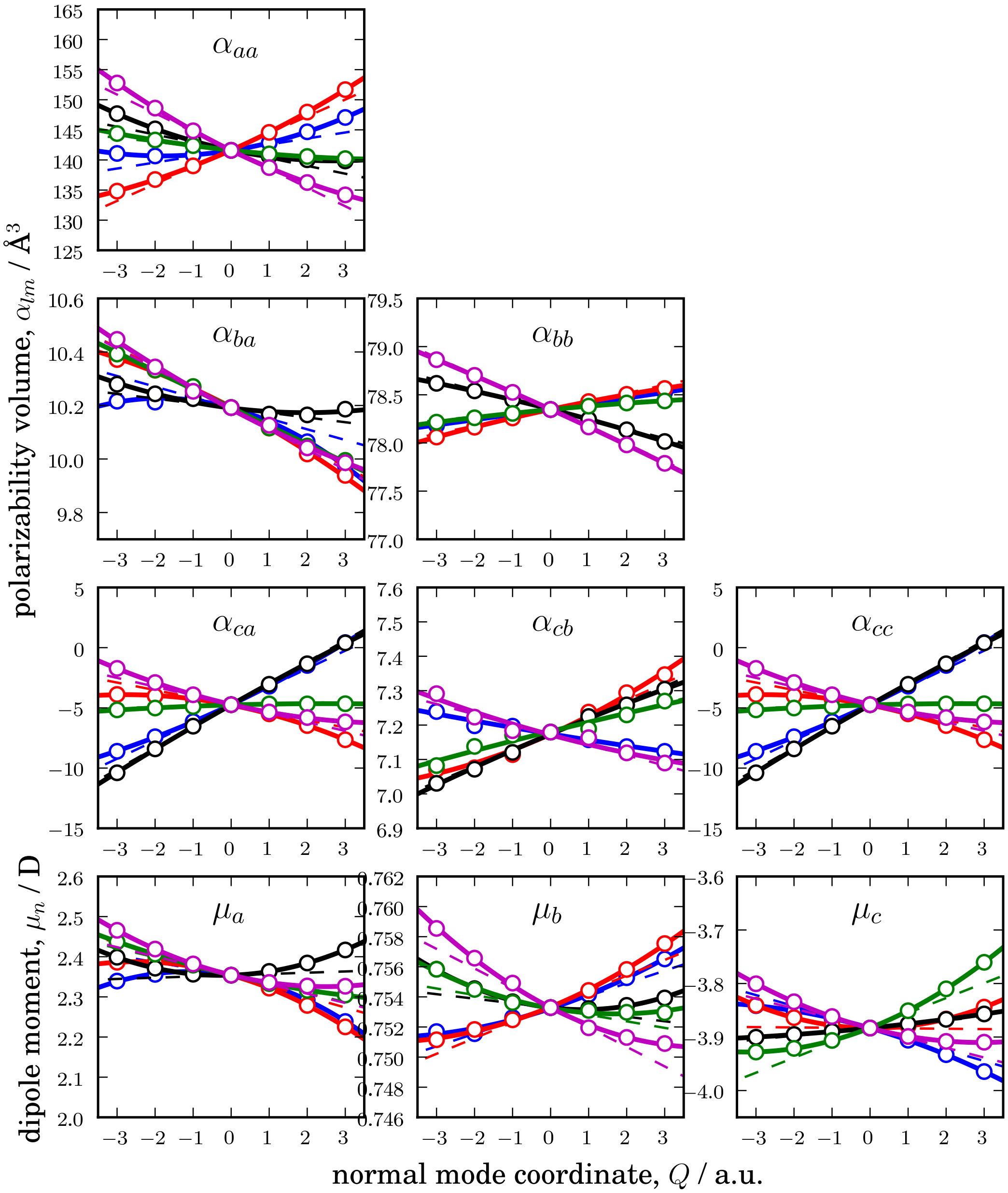

Figure 2.14: Elements of the polarizability tensor $\alpha_{lm}^{(1)}$ and dipole moment vector μ_n for the five phenylalanine aromatic C-H stretching modes: $\nu_{20\mathrm{a}}$ (blue), $\nu_{7\mathrm{a}}$ (red), $\nu_{7\mathrm{b}}$ (black), $\nu_{20\mathrm{b}}$ (green), and ν_2 (magenta). The lmn coordinate system for the phenyl ring is illustrated in Figure 2.9. Points, lines, and coordinates are as described in Figure 2.7 and in the text. The normal mode coordinate Q appears in arbitrary units.

a twist about the phenyl ring ψ_0^{Ph}, and a Gaussian distribution of phenyl tilt angles

$$f_{\mathrm{ODF}}^{\mathrm{Ph}} = \exp\left[-\frac{(\theta - \theta_0^{\mathrm{Ph}})^2}{2(\sigma_\theta^{\mathrm{Ph}})^2}\right]. \tag{2.36}$$

For each solution of $(\theta_0^{\mathrm{CH2}}, \sigma_\theta^{\mathrm{CH2}}, \psi_0^{\mathrm{CH2}}, \sigma_\psi^{\mathrm{CH2}})$ consistent with experimental methylene amplitude ratios, we have determined θ_0^{Ph} based on the lab frame projection of the CH_2-phenyl bond angle. The width of the phenyl tilt distribution $\sigma_\theta^{\mathrm{Ph}}$ was estimated by projecting 200 geometries covering the two-dimensional parameter space $\theta_0^{\mathrm{CH2}} \pm \sigma_\theta^{\mathrm{CH2}}$ and $\psi_0^{\mathrm{CH2}} \pm \sigma_\psi^{\mathrm{CH2}}$, and then determining the resulting spread in θ_0^{Ph} values. From this $\sigma_\theta^{\mathrm{Ph}}$ was chosen so as to reproduce this distribution.

From Figure 2.3a we note that the ppp intensity of CH_2 ν_{ss} is ≈ 2 times that of any of the subtle features in the aromatic region. Since the intensity is proportional to the square of the peak amplitude, that means that aromatic amplitudes must all be less than $2^{-1/2} \approx 0.7$ of the CH_2 amplitude. Cutoff values based on similar considerations were applied to the ssp and sps polarization schemes. As a result, if we apply these constraints to each of the solutions identified in Figure 2.12, we end up with only the black points in that figure. These surviving solutions originate from widths of the methylene tilt and twist distribution as indicated by the corresponding black region in Figure 2.11. Therefore, of the four adsorbed Phe orientations identified in the relatively narrow neighbourhoods A–D (Figure 2.13), only structures in regions B and D will be considered further.

2.8 Discussion

We point out that sets of solutions arise since our experiment reveals only relative phase information between vibrational modes. Without knowledge of the absolute phase, one will always obtain a solution set related by $\theta_1 + \theta_2 = 180°$ and $\psi_1 - \psi_2 = 180°$. Previous studies of the polystyrene–water interface have determined that polystyrene phenyl groups are ordered at the surface, with a mean tilt angle of $70°$ when using a δ tilt angle distribution [190]. It is interesting to note that, in the case of structure D, this provides a geometry

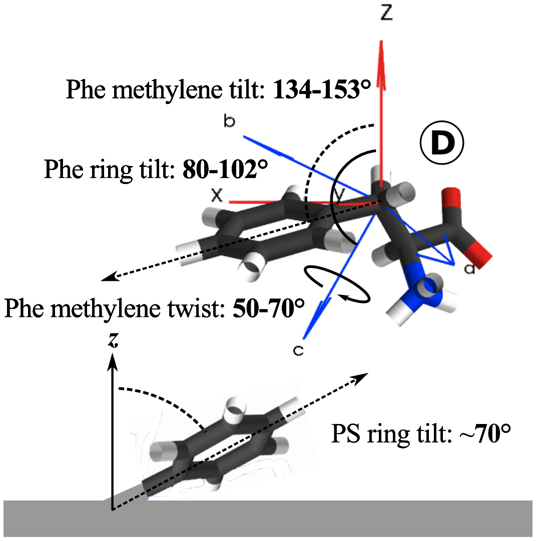

Figure 2.15: Proposed orientation of Phe (Structure D from Figure 2.13) on the PS surface. The tilt and twist angle of the CH_2 plane and the tilt of the Phe phenyl ring are indicated. The orientation of Phe with respect to the PS phenyl rings is also shown.

that maximizes π–π interactions upon insertion of the phenylalanine phenyl ring into the polymer surface phenyl rings (Figure 2.15). We believe that this is responsible for relatively narrow distribution of CH_2 tilt and twist angles that we have determined. We are also intrigued by our observed (fit) positions of ν_{ss} at 2870 cm^{-1}, and ν_{as} at 2974 cm^{-1}. The typical resonance frequencies of interfacial CH_2 modes are ν_{ss} in the range 2845–2870 cm^{-1}, and ν_{as} around 2885–2935 cm^{-1} [71,148,197–202]. In our case, ν_{ss} is therefore blue-shifted by about 12 cm^{-1}, and ν_{as} by about 40 cm^{-1} compared to Phe CH_2 modes in other SFG spectra [80, 203, 204]. While this effect may be unusual, it is certainly not uncommon. It is known that the formation of H-bonding pairs between CH and O groups result in the reduction of the C–H bond length, and subsequently, a blue shift of the resonance frequency [205–207]. This can also be seen, albeit to a lesser degree, if the CH group is placed near a proton acceptor group, such as a ketone [206]. This effect is commonly studied with regard to its impact upon protein folding, wherein intramolecular interactions between groups can result in specific folding patterns. However, in our case, Phe does not have its carboxylate groups in the correct relative orientation, so this must be an intermolecular interaction. We propose that the appropriate geometry for intermolecular oxygen π-CH$_2$ interaction may occur when our phenylalanine structure D is on the PS surface, with a methylene group of one Phe molecule directed at an adjacent Phe oxygen atom.

While structure D does correspond remarkably well with what is known about the surface tilt angle of the phenyl ring present in phenylalanine, it does not necessarily preclude the viability of B as an acceptable solution. Specifically, it is of interest that B presents its charged groups, the ammonium and carboxylate groups, more towards the solution than does D. While this does not necessarily explain the relatively narrow distribution of angles that satisfy all the requirements for this solution, it would be energetically favourable as it would allow for these charged groups to be more solvated and in a less sterically congested fashion than D would. Unfortunately, further work must be done in order to differentiate between these two structures.

Elements of the hyperpolarizability tensors are, in general, difficult to obtain, especially in the infrared region corresponding to specific normal modes at resonance conditions. Our approach for calculating $\alpha^{(2)}$ elements is a rather crude one; we have attempted to approximate the local environment of the Phe molecules by using a polarizable continuum model in our calculations. In reality, spectroscopic evidence often suggests that the electronic environment at the surface may be appreciably different from bulk environments such as gas phase or even solution. In order to make continued progress in this area, more sophisticated techniques for calculating surface vibrational hyperpolarizabilities will have to be established. A promising method may be to perform quantum molecular dynamics simulations with atomically-detailed surfaces in explicit solvent. At this time, however, the computational expense associated with such techniques prohibits the simulation of trajectories longer than tens of picosecond timescales. While such methods are progressing in solution, the techniques available for accurate computation of surface properties are at an earlier stage of development, often empirical in nature. Collecting quantitative spectroscopic data is probably the single most valuable contribution that can be made to promote the advancement and success of these techniques. Finally, our study showed that once all surface and molecular properties are known, there is still the issue of choosing a suitable orientation distribution function and evaluating its parameters. In many cases, the approximation of a Gaussian distribution is informative enough, since information on the widths of the angular distribution is as revealing of the surface structure as the mean angles. However, in the case of azimuthally-isotropic surfaces, there are only three unique elements of $\chi^{(2)}$ for each vibrational mode. In order to avoid errors associated with calibrating the $\chi^{(2)}$ and $\alpha^{(2)}$ scales to absolute units, we take ratios of quantities. Note that this comes at the expense of losing one known parameter in our orientation analysis. In the case of the CH_2 plane, we are fortunate to have two vibrational modes that are defined by the same local coordinate system (Figure 2.8). We therefore have redundant information that we are able to use to narrow the range of possibilities in our orientation analysis. In the case of the phenyl ring, five vibrational modes are defined by the same local ring coordinate system (Figure 2.9). If even a few of these modes were observed, one would have enough information to support a multi-parameter orientation distribution function, and/or redundant information to validate a particular simple orientation distribution.

2.9 Conclusions

There is increasing interest in the immobilization of proteins and peptides on surfaces, especially in the area of biosensors where control of the adsorbed geometry extends to orientation and conformation. Vibrational spectroscopy is a natural choice for such studies since one can probe specific chemical moieties without the attachment of labels such as fluorophores. We have demonstrated a complete procedure whereby SFG spectra obtained in different polarization schemes may be used to determine the orientation distribution of Phe on a hydrophobic polymer surface. There are several challenges that must be overcome to enable quantitative analysis by SFG spectroscopy. The first is calibration of the spectrometer response among the polarization schemes of interest. This is a nontrivial exercise but is perhaps the most crucial step for subsequent data analysis. Obtaining the macroscopic response is then reliant on fitting the spectra to obtain elements of the $\chi^{(2)}$ tensor for each vibrational mode of interest. Standard fitting routines are not well-suited to line shapes where peaks may have positive or negative amplitudes (or arbitrary phase) and then sum in a coherent fashion. We propose that one alternative is to consider fitting starting from a wide possibility of initial guesses to explore a multidimensional parameter space that contains many local minima. Finally, using macroscopic (ensemble averaged) quantities such as $\chi^{(2)}$ to deduce molecular orientation requires knowledge of the microscopic optical response.

We have used nonlinear vibrational spectroscopy to determine the structure of phenylalanine adsorbed at the aqueous–polystyrene interface. By calibrating the spectral response in different polarization schemes, we were able to collect spectra that revealed the contribution of individual components of the nonlinear susceptibility tensor, a measure of the ensemble average of surface molecules that ultimately encodes the structural information. We have described a robust fitting procedure suitable for the analysis of coherent line shapes with strong interferences. The molecular response was determined by calculating dipole moment and polarizability derivatives for the CH_2 symmetric and antisymmetric stretch from various ab-initio calculations. These values were then related from their molecular frame, in which they are calculated, to the laboratory frame in order to be comparable with the obtained spectral information. In the end, our favored structure had its CH_2 plane oriented with a tilt of 134–153° with a tilt angle distribution up to $18°$ wide; and a twist of 50–70° with a width up to $32°$. We have shown that the consequence of this geometry is that phenyl ring is situated with a narrow range of small angles relative to the plane of the interface (80–102° from the interface normal). This orientation has the unique characteristic of aligning the phenyl rings of the amino acid with those of the polystyrene surface. This suggests that intercalation may be responsible for the relatively constrained orientation of phenylalanine on the surface.

Chapter 3

A more general method for the determination of amino acid structure adsorbed to a surface based on nonlinear vibrational spectroscopy, electronic structure calculations and molecular dynamics simulations [1]

3.1 Overview

The great interest in the study of protein adsorption to polymeric surfaces is fueled by the application of the conclusions drawn from these studies to a variety of scientific and technical fields. The process of protein adsorption itself is known to be one of the most important events in many biological processes, impacting upon the initiation of many cellular activities [1]. In terms of chemical applicability, the understanding of this process is vitally important to the fields of chromatography [17, 21–26], where it is used to develop methodologies and separation technologies for the effective removal of proteins from solutions, to the development of biosensors [32–34] and drug delivery systems [35–37]. Many studies of protein adsorption are also conducted with a greater emphasis on the nature of the surfaces themselves. Control of the surface structure and topography as well

---

[1] Reproduced in part with permission from the Journal of Physical Chemistry, accepted. Unpublished work copyright 2011 American Chemical Society.

as the physical and chemical properties of the surface is incredibly important, as it can affect the reaction of the protein to the interfacial environment [5, 7, 8]. This is because the interaction of a protein with the polymeric surface can induce a change in the higher order structure of the protein [11]. This change can be drastic, even irreversible, in the case of protein denaturation upon adsorption [12, 13]. As such, there is also a great deal of research conducted based on the production of biocompatible polymeric coatings for medical implants, where it is known that the initial response of an implant is the formation of a protein layer at its surface [6]. In this case, there is a vested interest in the development of haemocompatible and bacterial-adhesion resistant polymers [14–16], for which a basic understanding of the processes involved in the formation of the protein film would be a great asset.

Adsorption of proteins to surfaces has been studied for the better part of the last century by a variety of processes. The difficulty in this, however, has been in focusing the experimental technique utilized solely upon the interfacial region so as to avoid any contamination of the data by responses obtained from the within the solution as opposed to the interfacial region. The methods of choice have included *in situ* procedures such as fluorescent- and radio-labelling [5], confocal fluorescence microscopy [142], total internal reflection fluorescence [143], and quartz crystal microbalance impedance [144–149], attenuated total reflection infrared spectroscopy [145, 151, 152], and Raman spectroscopy [154–157]. A variety of *ex situ* methods have also been employed, specifically atomic force microscopy [158–160], electron microscopy [161, 162], neutron scattering [163] and x-ray photoelectron spectroscopy or electron spectroscopy for chemical [164–167].

The inherent difficulty in furthering this field is evidenced in the nature of proteins themselves. They are, generally, very large molecules that are comprised of alternating regions of differing chemical and physical properties that, in turn, can be rearranged based on differences in higher order structure [12, 13]. As such, it is often necessary to simplify the system in order to focus upon specific regions of the protein and their individual interactions with the surface. The most logical course of action in this case is to reduce the size of the molecule being studied, such as using models for these regions of the proteins like peptides or even amino acids. It is known that the amino acid composition of the protein itself does have a great effect upon the adsorption characteristics [39, 40]. However, it should be noted that the ability to predict the adsorption characteristics based upon the amino acid composition is limited, making it important to carefully study amino acid adsorption in order to further this field.

Amino acid adsorption to a variety of surfaces has been studied by, generally, similar methods as those applied to protein adsorption, including electron microscopy [162], X-ray diffraction [52], spectrophotometry [55], and chromatography [59, 60].

While the importance of all of these methods cannot be overstated, there are some inherent problems in their ability to focus, exclusively, upon the interfacial region and to probe the actual physical orientation of the molecule of interest at the surface for *in situ* studies. At this point, it is important to introduce the experimental method utilized in this study: nonlinear optical techniques. Specifically, amongst the second-order nonlinear optical techniques visible-infrared sum frequency generation, or SFG, has the unique characteristics to make it extremely effective as a method for studying the adsorbed structure of amino acids. The most important characteristic possessed by SFG is that the intensity of a SFG active vibrational mode relies upon the second-order susceptibility $\chi^{(2)}$ tensor.

$$I_{\mathrm{SFG}} \propto \chi^{(2)}_{\mathrm{eff}} \chi^{(2)*}_{\mathrm{eff}} = |\chi^{(2)}_{\mathrm{eff}}|^2 \tag{3.1}$$

This $\chi^{(2)}$ tensor is only non zero under the condition that the two radiation sources involved, a fixed wavelength visible beam and a tuneable infrared source, are coincident in time and space at a point that does not possess symmetry through inversion. Since the bulk solution is centrosymmetric as well as the polymeric film, generally, the experiment only has a significant response from the interfacial region between these two phases. Additionally, the use of a tuneable infrared source in the experiment allows for the experiment to focus upon specific moieties of the amino acid being studied, allowing to focus upon specific regions of interest. This method has been applied to the study of amino acids previously [53, 80, 81], as well as other model peptide systems [43, 83–85], and complete proteins as well [86–89].

Finally, if the SFG experiment is conducted using a variety of polarization states for the incident visible and infrared beams as well as the resultant SFG beam, it is possible to determine the conformational structure of the molecule under analysis. This is due to the fact that the non zero components of 27-element $\chi^{(2)}$ tensor contain structural information, and these components can be extracted by performing the experiment in different polarization combinations. This, of course, presupposes that the molecular companion to the $\chi^{(2)}$ tensor known as the hyperpolarizability tensor, $\alpha^{(2)}$, of the molecule itself is completely known, which can be determined through either simple bond additivity models [181–183], or through quantum chemical calculations [100, 179, 184–186]. Several accounts are known in the literature of this being used to determine surface structure of molecules [93–95].

In a previous study performed by the author, the orientational distribution of phenylalanine adsorbed from an aqueous solution at a polystyrene layer was determined [208]. This work, while illuminating, was dependent upon the absolute assignment of the vibrational modes being used in the orientational study, in that case the symmetric and antisymmetric CH_2 stretches. The modes were also confined to the plane defined by the methylene moiety, making them useful in the definition of a molecular coordinate system that could be then related to the laboratory frame in order to determine the overall structure. These two requirements for the methodology utilized in that study, that the vibrational modes in question be absolutely determined and that there be no coupling between modes of similar energies, cannot always be satisfied. In the case of proteins this is fairly obvious. With large regions of alkyl moieties one would be justified in expecting many modes within the 2800–3200 cm^{-1} range. These modes are also likely to be very close in energy to one another, resulting in heavy coupling between modes. As such, the previous methodology is unsuitable to these molecules and another path to determine their surface orientation will be required.

To this end, we turn to molecular dynamics simulations for inspiration. Through the employment of the equations of Newtonian motion, one can study the forces and energies that exist in very complicated systems. This is done through the calculation of potential energy for a system with a given number of molecules with a specific configuration. In these calculations, each atom or species present has a given force acting upon it, which is then used to calculate a displacement. Once this displacement is completed, the potential energy is calculated once more and the calculation continues. These steps are generally on the order of femtoseconds, but with enough of these calculations sufficiently stable statistics can be obtained, in our case for the adsorption of a molecule to a surface. These methods have been used to considerable success in the study of interfacial regions [158, 169, 173–176].

The intent of this Chapter is to utilize information obtained from molecular dynamics simulations of the amino acid leucine to surfaces of hydrophobicity similar to that of polystyrene to determine an orientational distribution for these molecules, based upon SFG experiments performed on leucine adsorbed to polystyrene from an aqueous solution. Leucine was selected in this case due to its structure that contains several alkyl moieties, and the belief is that this would result in SFG spectra that are much more complex than those noted for phenylalanine. Specifically, the vibrational modes of leucine are expected to be heavily coupled to one another and very difficult to uniquely assign.

3.2 Materials and Methods

3.2.1 Sum Frequency Generation Experimental Procedure

The SFG spectrometry system used for these experiments (Ekspla, Lithuania) utilizes 30 ps Nd:YAG laser operating at a frequency of 10 Hz (Ekspla PL2241A). The system provides

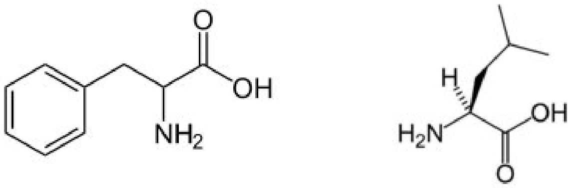

Phenylalanine **Leucine**

Figure 3.1: A structural comparison of the amino acids phenylalanine and leucine. It is important to note the many structural differences between these two molecules and the resultant predictions that can be made about their infrared spectra. Phenylalanine is comprised of a full phenyl ring with only one alkyl region, the methylene moiety. This is contrasted with the leucine molecule that contains two methyl and methine groups as well as a methylene group. Where the phenyl and methylene regions of phenylalanine are known to have different energies, all groups mentioned for the leucine molecule are known to be very similar in energy, complicating its response to infrared absorption.

two beams, one visible operating at 532 nm focused to a diameter of 1 mm at the sample providing an energy of 110 μJ per pulse, and the other an infrared source tuneable between 2800-3200cm^{-1} focused to 0.5mm at the sample at an energy of 200 μJ per pulse. The latter is produced in an optical parametric generator comprised of a crystal of $AgGaS_2$ by the process of difference frequency generation (Ekspla PG501). In order to couple these two beams to the sample, they are focused upon the prism-polymer interface of a dove-cut prism of CaF_2 (Del Mar Photonics), where the visible radiation is incident at 66° while the infrared contacts the interface at 64°.

The production of the polymer-coated prism begins with the submersion of the prism in 0.1% v/v nitric acid in concentrated sulfuric acid. This is followed by rinsing for at least 5 minutes with deionized water with a resistance of at least 18 MΩ (Nanopure, Barnstead Thermo). Next, a two stage polishing process is undertaken. Initially, the three faces of interest present on the dove-cut prism are polished with 3μm polycrystalline diamond suspension (Buehler Metadi Supreme), followed by a 1 minute rinse in deionized water. The second step involves polishing the 3 faces of interest again with a 0.05 μm silica suspension (Buehler Masterprep) and a final rinse with deionized water.

The polymer film itself is produced by dissolving D_8 polystyrene with a molecular weight of 270500 g/mol and a polydispersity index of 1.25 (Polymer Source) in $CDCl_3$ to produce a solution of 3% w/w. This solution was then spin coated (Model F3-8 Specialty Coating Systems, IN) on the back face of the prism, accelerated over 1s to 1500 rpm, spun for 90s, and decelerated over 1s. The prism was then dried overnight at room temperature beneath a protective covering.

The experimental cell itself is constructed by forming a water tight seal between the polymer-coated side of the prism and the teflon sample cell by pressing the prism into a fluoropolymer O-ring (Marco Rubber, NH). An initial scan of the sample with pure D_2O (Cambridge Isotope Labs) in the sample cell between 2800-3000cm^{-1} was performed to ensure the cleanliness of the system provided no C-H stretching modes were observed. The D_2O was then removed and replaced with a 12.5 mg/ml solution of L-leucine (Aldrich) in D_2O.

SFG spectra were obtained by varying the infrared beam energy between 2800-3000cm^{-1} with a step size, ω_{IR}, of 2cm^{-1}. At each infrared energy, the SFG intensity was calculated as an average of 100 pulses. Three separate combinations of the perpendicular polarization states (s- and p-) of the three beams present in the experiment, SFG, visible and infrared, were used: ssp, sps, and ppp.

3.2.2 Molecular Dynamics Simulations

All simulations of leucine adsorption were performed using the GROMACS package [209] with 3840 SPC/E water molecules [210] and one leucine molecule present in the zwitterionic state. These molecules were placed between two surfaces forming a three dimensional box of $42 \times 42 \times 70$ Å^3 initially. Cutoffs were placed upon the van der Waals interactions between atoms at a distance of 9 Å. The surfaces themselves were defined by Steele 10-4 potentials [211, 212] installed at the planes $z = 0$ Åand $z = 70$ Å. Thus, the

ε / kJ $\cdot$ mol^{-1}	contact angle /°	z cutoff /Å
0.550	156	3.0
1.10	151	3.0
1.93	134	3.5
2.75	125	3.8
4.13	101	3.9
5.50	84	4.0

Table 3.1: Values of ε and their corresponding contact angles and z cutoffs for water-surface derived from Ref [178]

potential energy of the surfaces was defined by the Lennard-Jones interactions which were integrated over these surfaces according to

$$U(z) = 2\pi\sigma^2\varepsilon\left[\frac{2}{5}\left(\frac{\sigma}{z}\right)^{10} - \left(\frac{\sigma}{z}\right)^{4}\right]. \tag{3.2}$$

In Equation 3.2, the variable σ defines the distance from the surface in the z direction at which the potential energy well will be zero while ε defines the depth of said potential well at the surface itself. For this study, the value of σ was maintained at 3 Å, while the value of ε was varied to produce surfaces of differing hydrophobicities [178, 213].

The intramolecular interactions for leucine and those between the leucine and surrounding water molecules were calculated as per the OPLS-AA/L force field [214]. In order to allow for free rotation of the dihedral angles in leucine the harmonic terms in the potential energy calculation were removed, allowing bond rotation to be more accessible. The only interactions impacting upon dihedral angles were van der Waals interactions, requiring the removal of these 1-4 interactions specified in the OPLS-AA/L force field.

The potential energy of each configuration was determined by minimizing the systems energy three times via the steepest descent method, using step sizes of 0.01 Å, 0.05 Å and 0.1 Å, in order of increasing step size to ensure the system was not trapped in an unstable starting configuration. The next step involved the simulations of the system in parallel, 9 simulations each on 8 processors, each being equilibrated for 200 ps. Each simulation had its own initial set of starting velocities for each atom, generated randomly while ensuring an average temperature of 300 K and at a pressure of 1.01325 bar using the Berendsen thermostat and barostat [215]. The pressure was maintained by allowing variation in the x and y directions while maintaining a constant z dimension. This pressure coupling resulted in, at maximum, a 1% variation in the x and y dimensions of the system, which equilibrated after the first 10 ps. Each simulation provided 10 ns of data, with a snapshot of the configuration being saved every 50 fs, resulting in 90 ns of data for each system integrated with a 1 fs step size. In order to ensure the two surfaces were identical, all molecules above the midpoint in the z direction of the box in the simulations were transformed by a 180° rotation about the y-axis.

3.2.3 Electronic Structure Calculations

All calculations were done using the GAMESS quantum chemistry package [187] deployed on an Intel Xeon cluster, at the B3LYP/6-31G(d,p) level of theory, as it is noted that this basis set is capable of reproducing infrared spectra of gas phase amino acid [194]. A polarizable continuum model (PCM) was used to predict properties arising from an aqueous solution. In the case of the separate conformations determined from molecular dynamics, it was necessary to produce input structures based on the simulations and the optimize their structures constraining the two dihedral angles upon which their structures were determined from the simulations. This initial optimization allowed the remaining parts of the leucine structure to reorient themselves accordingly. Once this was done, the constraints were removed and the structural optimization performed once more. These optimized structures were then used to calculate their Hessian matrices. Since the normal modes were not readily assignable the choice of a scaling factor was made non-trivial. Finally, instead of choosing a single scaling factor, it was decided that of the 10 modes noted for each structure comprised of C-H stretches, the highest and lowest energy stretches should be assigned to values obtained from a similar SFG experiment where leucine was studied at the air-water interface [82]. At these two extremes, the interpolated scaling factors were near to 0.94 and

0.97, certainly within the regularly acceptable ranges for these types of vibrations.

In order to approximate the $\alpha^{(2)}$ tensor and, thus, be able to predict SFG spectra, it was necessary to calculate the derivatives of the dipole moment and polarizabilities of each of the 10 normal modes noted.

$$\alpha^{(2)}_{lmn}(\omega_{\mathrm{IR}}) = \alpha^{(2)}_{\mathrm{NR},lmn} + \sum_{\nu} \frac{a_{\nu,lmn}}{\omega_{\nu} - \omega_{\mathrm{IR}} - i\Gamma_{\nu}} \tag{3.3}$$

This was accomplished by constructing 6 structures, in addition to the original equilibrium structure, for each of the 5 conformers. These were based upon extending and contracting the bonds being varied in each vibrational mode by stepping along their normal mode coordinate, Q. Once calculated, the values of the dipole moment and polarizability can be plotted with respect to their normal mode coordinate and the derivative approximated by determining the tangent at Q = 0, allowing for the determination of $\alpha^{(2)}$ as per Equation 3.3.

3.3 Implementation of Coordinate Transformation in the Leucine Orientation Analysis

While the general principle of obtaining necessary information in an appropriate frame of reference is conserved between the analysis of phenylalanine and leucine, certain interesting facets actually make the methodology used in the leucine case more general and, surprisingly, simpler to implement. While the same information is obtained, in the form of SFG spectra and ab-initio calculations, there is another collection of information obtained for leucine on surfaces: Molecular Dynamics simulations. From the MD data, the surface orientation of the molecule, and thus the modes being compared to the SFG spectra, are known exactly, allowing for SFG spectra to be calculated directly. Additionally, is not necessary, nor simple, to accurately define the modes of interest, as was required for the phenylalanine project exhibited in the selection of the symmetric and antisymmetric stretchs of the CH_2 mode to correspond with the CH_2 plane. As such, the combination of MD data with ab-initio calculations leading to approximate values of α and μ for all modes

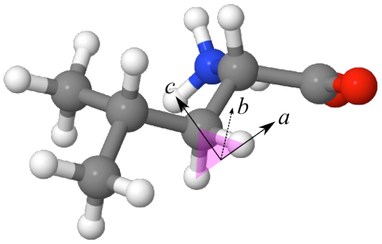

Figure 3.2: Definition of a coordinate system based entirely upon the CH_2 region of leucine. Euler angles show the rotations about their respective axes relating abc to xyz.

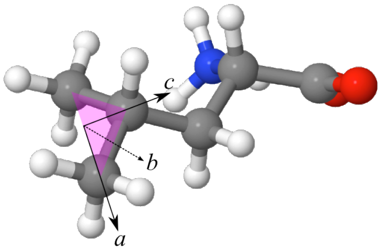

Figure 3.3: Definition of a coordinate system based entirely upon the region comprised of the two methyl carbons and the tertiary carbon in leucine. Euler angles show the rotations about their respective axes relating abc to xyz.

within a region of interest provides us with a simpler route for getting the desired theoretical data that can then be fit against the SFG spectra themselves. The MD simulations provide theoretical values for the orientation of the molecule at the surface and are defined in the same frame as the laboratory, ijk. As such, provided that the information determined from the MD simulations is obtained in a consistent manner based on a specific coordinate system, only one transformation is required.

As can be seen in Figures 3.2, 3.3 and 3.4, any correctly defined collection of three orthogonal vectors can provide a coordinate system for the orientational analysis of leucine at the surface. As such, it is necessary to choose a frame based not upon which frame provides the most physically relevant information. In the case of leucine, an interesting piece of information used for the comparison of spectra was calculated from the different populations of leucine molecules standing or laying upon the surface. The Figure 3.4 shows

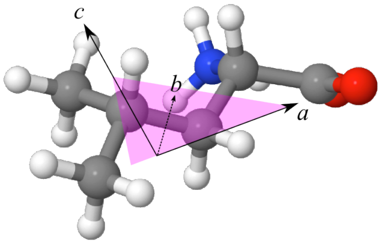

Figure 3.4: Definition of a coordinate system based entirely upon an arbitrary region of leucine. Euler angles show the rotations about their respective axes relating abc to xyz.

that the a vector closely approximates the "long axis" of leucine, and thus would clearly mark whether the molecule were standing or laying. The vector c in the "3C" plane, as described by Figure 3.3 also closely resembles the long axis.

Once the coordinate system is selected and the orientation determined from the molecular dynamics data directly, from which the Euler angles can be determined, it is simply necessary to define an identical coordinate system within the arbitrary frame of reference in which our ab-initio calulations are performed. For this reason alone, it is easiest to select a coordinate system based on atoms within the molecule. The two coordinate systems defined for the leucine molecule, named 3C and CH_2 respectively, were analyzed in their entirety to discover which provided the best resolution, as exemplified by differences in calculated SFG spectra, between standing and laying leucine molecules. For the 3C plane, the c vector was defined as emanating from the midway point between the two methyl carbons through the tertiary carbon. a was defined as emanating from the same midway point through one of the methyl carbons, selected arbitrarily. b as per usual is described by the cross product of c and a. In the CH_2 system, c is defined as a vector from the bisector between the two hydrogen atoms passing through the carbon atom, a is defined as a vector traveling from the same original point as c through an arbitrily selected hydrogen atom, and b exists once more as their cross product. The latter system was used for the analysis as it provided greater resolution between standing and laying spectra.

The DCM for the plane selected is defined based on these three vectors as seen in

Equation 2.8 in the previous Chapter. For clarity the development of D will be repeated. The actual transformation process is now distinctly more simple than that which was used for the phenylalanine system. Again, it is necessary to transform the α and μ derivatives from the arbitrary GAMESS frame into the selected frame, in this case the CH_2 frame, by performing a "forward" coordinate transformation, employing the matrix D.

We know that, specifically, we have a desire to move information calculated in the GAMESS frame, xyz, into the aforementioned molecular frame of choice, abc. This can be done quite simply knowing that our xyz coordination system is built from the three orthogonal unit vects $x = [1, 0, 0]$, $y = [0, 1, 0]$, and $z = [0, 0, 1]$. In order to build a direction cosine matrix, we will need to determine the cosine elements, D_{qr}, which can be calculated as the cosine of the angle between any two vectors q and r. As an example, we will show this calculation between the vectors b and y.

$$\cos\theta_{by} = \frac{b \cdot y}{|b||y|} = b \cdot y = b_1 y_1 + b_2 y_2 + b_3 y_3 \tag{3.4}$$

Since y is a unit vector, we obtain $y \cdot b = b_2$. If we perform this operation for all 9 possible combinations of vectors between these two frames, we can determine all elements of the direction cosine matrix, D.

$$D = \begin{bmatrix} a_1 & b_1 & c_1 \\ a_2 & b_2 & c_2 \\ a_3 & b_3 & c_3 \end{bmatrix} \tag{3.5}$$

To show that this matrix, in fact, applies the transformation correctly to data in the xyz frame in order to transform it into the abc frame, we can show that multiplying this by any of the three vectors that definine the xyz frame should result in their being transformed to their corresponding vector in the abc frame.

$$\begin{bmatrix} a_1 & b_1 & c_1 \\ a_2 & b_2 & c_2 \\ a_3 & b_3 & c_3 \end{bmatrix} \begin{bmatrix} 1 \\ 0 \\ 0 \end{bmatrix} = \begin{bmatrix} a_1 \\ a_2 \\ a_3 \end{bmatrix} \tag{3.6}$$

This holds true for the transformation of the vectors y and z into their corresponding abc system vectors as well.

As an example, we will describe the transformation of the dipole derivatives from their original GAMESS based frame, $i'j'k'$, to the laboratory frame as defined by the molecular configuration from the MD simulation. We begin with a forward transformation, taking the dipole moment derivatives from the arbitrary GAMESS frame into the CH_2, or lmn, frame.

$$(\frac{\partial\mu}{\partial Q})_{lmn} = D_{\text{GAMESS}}(\frac{\partial\mu}{\partial Q})_{i'j'k'} \tag{3.7}$$

Now, once the DCM is built based on the location of the CH_2 frame found in the molecular dynamics simulation, we can use the fact that the CH_2 frames as located in our GAMESS calculation and those found in the MD simulation are identical. Thus, we can move directly to the laboratory frame, xyz, as defined in GAMESS by applying the inverse transformation determined by the DCM of the CH_2 frame determined from the molecular dynamics simulation.

$$(\frac{\partial\mu}{\partial Q})_{xyz} = D^{-1}_{\text{GROMACS}}(\frac{\partial\mu}{\partial Q})_{lmn} \tag{3.8}$$

Now that the information is possessed in this plane, it is necessary to simply select the molecule of choice from the molecular dynamics data, build its DCM based on the same CH_2 frame and transform the information from the molecular CH_2 frame to the laboratory xyz frame through the application of another “inverse” coordinate transformation. This transforms the information from the CH_2 frame in GAMESS molecule directly into the xyz frame of the molecular dynamics simulation, or laboratory frame. This is true as the xyz frame defined within the molecular dynamics simulations is the same as the actual laboratory xyz frame, employing the matrix D^{-1}.

$$D^{-1} = \begin{bmatrix} a_1 & a_2 & a_3 \\ b_1 & b_2 & b_3 \\ c_1 & c_2 & c_3 \end{bmatrix} \tag{3.9}$$

Step by step, this takes the information from the arbitrary GAMESS frame to the CH_2 frame of the molecule in the GAMESS calculation to the xyz frame of the molecular dynamics simulation, which is commensurate with the laboratory frame. This eliminates the necessity for the use of orientation distribution functions and projecting the information in the molecular frame into the laboratory frame based on that as the structure is essentially known. This allows for fairly direct determinations of the hyperpolarizability approximations in the frame of interest and, most importantly, does not require any knowledge of the mode assignments prior to use. Thus, it is applicable to other systems in a very general fashion, specifically of interest to those that are more complex and less well studied.

3.4 Molecular Dynamics Analysis

The utility of molecular dynamics studies is that they provide the exact positions of the atoms present with the systems, allowing for the analysis of systems that vary over time at a molecular level. In this case, it was leucine adsorbing to surfaces of varying hydrophobicity that was studied by Travis Trudeau in his work [178]. This initial study of leucine adsorbing to surfaces from aqueous solutions relied upon the definitions of a few specific points on the zwitterionic form of leucine, $\mathrm{P}_{\mathrm{CH}_3}$, $\mathrm{P}_{\pm}$, and $\mathrm{P}_{\mathrm{COG}}$, the point between the two methyl groups, between the nitrogen of the amino group and the carbon of the carboxylate group and the center of mass respectively. The $\mathrm{P}_{\mathrm{COG}}$ was of great use in that it helped defined whether a leucine molecule was close enough to the surface to be considered adsorbed, in the case that $\mathrm{P}_{\mathrm{COG}} \leq 7.5$ Å. Additionally, a vector traveling from $\mathrm{P}_{\mathrm{CH}_3}$ through $\mathrm{P}_{\pm}$, known as V_l was defined. Through the monitoring of the tilt of this vector with respect to the surface normal, it was discovered that when adsorbed, leucine adopted either a standing orientation, with the tilt of V_l between 0 and 20°, or laying, with the tilt existing between 70 and 90°. This discovery, that leucine adopted different conformations, was the initial inspiration for fitting the obtained SFG spectra using molecular orientations found from MD simulations.

Based on a cursory inspection of Figure 3.6, the previously described phenomena become apparent. It is obvious, by following the distance of $\mathrm{P}_{\mathrm{COG}}$ from the surface that the molecule is adsorbing and desorbing from the surface, and through monitoring the tilt of V_l

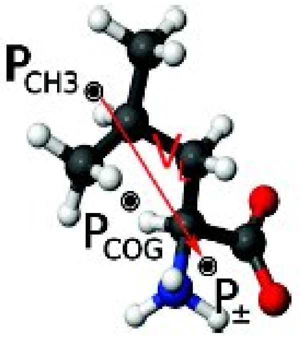

Figure 3.5: Original description of the zwitterionic form of leucine used in Ref. 178, describing the three points of interest, the midpoint between the two methyl carbons, P_{CH_3}, the midpoint between the carbon of the carboxylate group and the nitrogen of the amino group, $P_\pm$, and the center of gravity, P_{COG}. Finally, the vector traveling from P_{CH_3} to $P_\pm$ is defined. This was the vector V_l initially used to determine whether the molecule was adsorbed in a standing or laying orientation.

it can be seen that it exists in two separate orientations at the surface.

However, simply having these three points of interest and this single vector form and insufficient basis for the prediction of SFG spectra. Specifically, it is necessary to have a plane that is shared between the molecule present in the molecular dynamics simulations and the molecule defined in the input of the electronic structure calculations. Upon inspection, leucine has two promising regions that could be used for this purpose, the methylene moiety and the adjacent sec-propyl group. These two regions were used to create two planes and their associated coordinate systems, known as CH_2 and 3C respectively, described in detail in Figure 3.2 and 3.3.

Since the two planes defined based on these different sets of atoms in the leucine molecule are essentially equivalent in utility, they were both subjected to an orientational analysis in order to compare their ability to differentiate between the standing and laying orientations of leucine. This was done by comparing the tilt and twists of the CH_2 and 3C planes individual to the tilt angle of the V_l vector. The improved separation between the standing, blue contours, and laying, red contours, for the CH_2 plane made this the plane of choice for further analysis as seen in Figure 3.7. The CH_2 moiety would also form the

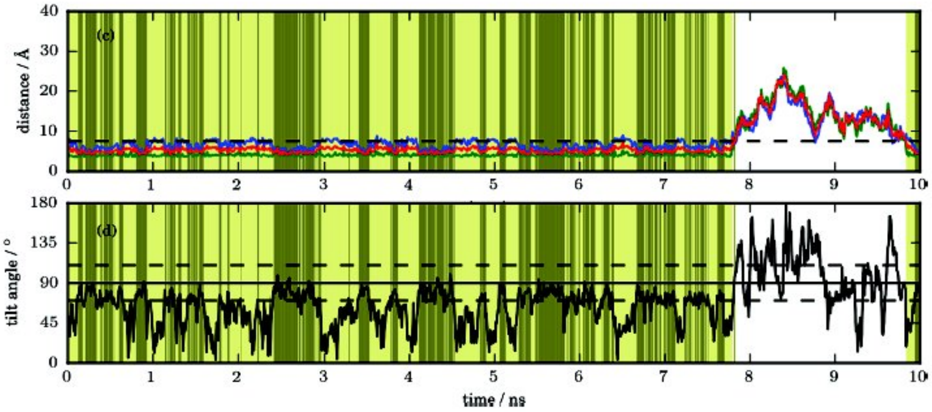

Figure 3.6: 10 ns example of the molecular dynamics simulation for the 84° contact angle surface described in Ref. 178. The molecule is considered at the surface for all the yellow region shows where leucine has adsorbed to the surface and white where it is tumbling in solution. The three traces in the upper graph describe the three positions along the z axis of P_{CH_3} in green, $P_{\pm}$ in blue and P_{COG} in red. The molecule is defined as being in the laying orientation if the tilt angle of the vector V_l was between 70 and 90°, shown by the dashed horizontal lines in the lower graphic.

central point for which our dihedral angles were defined later in the analysis.

At this point, an abortive initial attempt was made at fitting the SFG spectra. This seemed logical as a basic structural difference between the molecules adsorbed at the surface, standing versus laying, was found, planes correctly defined and the spectral responses of these two different orientations was found to be different. Unfortunately, the quality of the fits obtained was abysmal, and it became apparent that we did not possess sufficient information to accurately fit the spectra. Up until this time, the electronic structure calculations had been performed using a stock leucine molecule found in the GAMESS structure archive. It was thought that this could possibly be the source of the difficulties being experienced. Since leucine is a relatively small molecule, it was decided that the definition of two dihedral angles, ξ_1 between hydrogens 1 and 4 described in Figure 3.8 and ξ_2 between hydrogens 4 and 6 in the same figure, could effectively describe the conformation of the molecule entirely. The molecular dynamics data was then analyzed once more, wherein the molecules adsorbed at the surface were separated

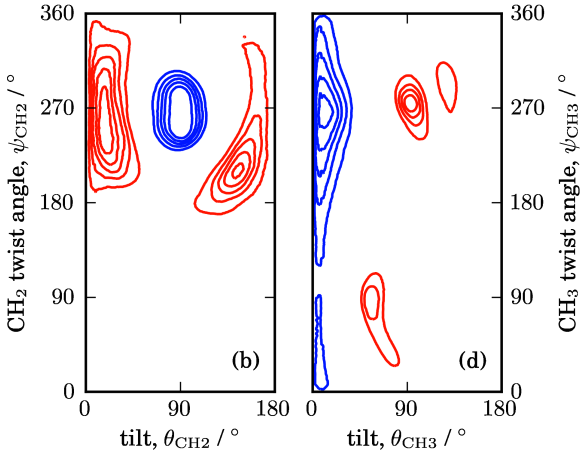

Figure 3.7: The orientation distribution, described through the tilt and twist angles of the two planes used for the initial analysis, with the CH$_2$ plane on the left and the 3C plane on the right. The red traces are for the laying populations, while the blue traces are correlated to standing species. As can be noted from this figure, the CH$_2$ plane provide better resolution, and thus was used for further analytical purposes.

not only into standing and laying populations, but for each molecule the value of ξ_1 and ξ_2 were determined and correlated, in the hopes of identifying the structures at the surface.

The results of this analysis are collected in Figure 3.9. Upon inspection, 5 distinct regions of correlated dihedrals were apparent. These 5 regions describe unique conformations of the leucine molecule adsorbed at the surface and, provided that they all provide different predicted spectral responses, could be used as a basis for fitting the acquired SFG spectra. It is important to note that all 5 conformations exist both in the standing and laying orientations, as can be seen in sections (a) and (b) in Figure 3.9. The structures for each of these conformations with their geometries optimized in GAMESS are presented in Figure 3.10.

More information can be gleaned from Figure 3.9, specifically in terms of the relative populations of each of these conformations present at the surface. This can be determined by summing up the populations in each of the 5 regions, described in (c) of Figure 3.9. In that Figure, all the populations from the 5 different surfaces were summed, but the same analysis could be performed for each separate case. The results are described graphically in

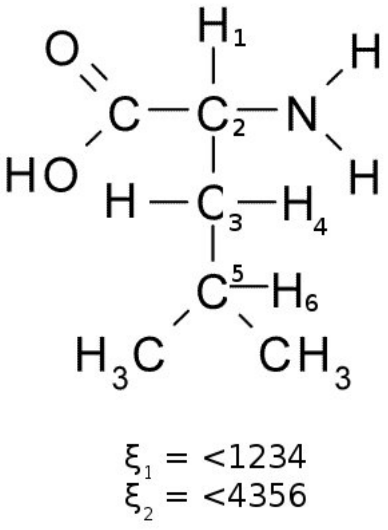

Figure 3.8: A flat projection of l-leucine for the purposes of defining the two dihedral angles used to determine different conformations of leucine present at the surface. ξ_1 is defined as the dihedral between Hydrogen 1 and Hydrogen 4. ξ_2 is defined as the dihedral angle between Hydrogen 4 and Hydrogen 6. These dihedrals are also known as the "R"-group dihedral and the "iso"-butyl dihedral, shortened to "R" and "iso" or (ξ_1, ξ_2) for convenience. It is to be noted that the relatively small nature of leucine allows its structure to be efficiently described in these two dihedrals alone.

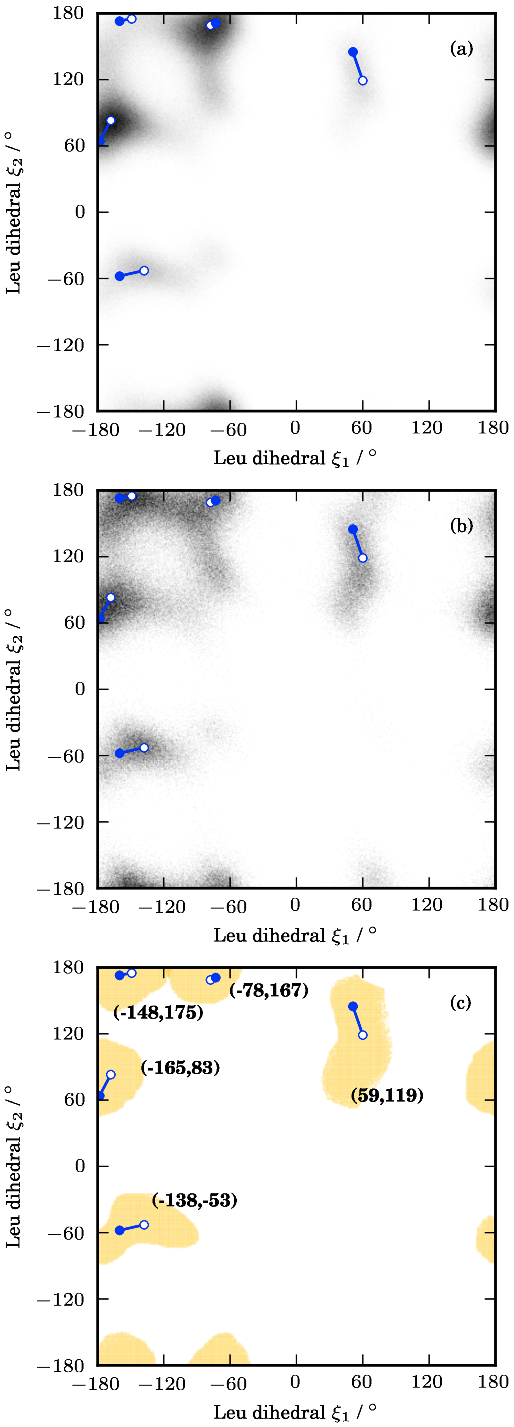

Figure 3.9: Correlations between the dihedral angles ξ_1 and ξ_2 for the standing (a) and laying (b) populations of leucine molecules. The third graphic, c, describes the regions used for the calculation of population statistics for each of the 5 notable regions present. The black points show the final dihedrals obtained from quantum chemical calculations while the white points show the position of highest population density. The 5 regions correspond to 5 unique conformations of leucine that are present at the surfaces for these MD simulations. For these graphics, the populations of all 5 surfaces are summed.

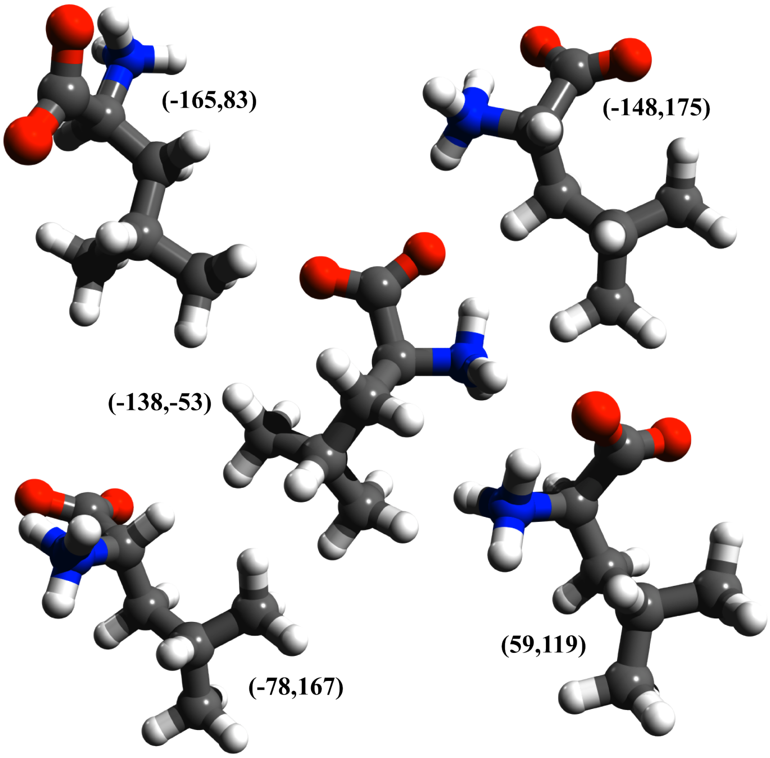

Figure 3.10: Representations of the 5 conformations of leucine identified at the surfaces from the MD simulations, as defined by the two dihedral angles (ξ_1,ξ_2).

Figure 3.11. As can be noted, there is a variation in the relative populations of standing and laying within the individual conformers as a function of the surface hydrophobicity, with a greatest percentage of laying at highest hydrophobicity. There is also a slight variation in the overall population of each conformer.

Based on this information, the existence of 5 conformers at the surfaces in the molecular dynamics simulations, a fitting routine can be readily developed to fit the obtained SFG spectra providing insight into the orientational distribution.

3.5 Spectral Fitting and Orientational Analysis

SFG spectra for leucine adsorbed to a deutrated polystyrene surface from a D_2O solution were obtained in three polarization configurations, ssp, sps, and ppp, as shown in Figure 3.12.

Beginning from this point, it is the goal to relate the information obtained from the molecular dynamics simulations to these obtained SFG spectra. Structures based on the 5 conformations were generated and subjected to geometry optimizations in GAMESS followed by calculations of their Hessian matrices. Upon inspection of these matrices, it was determined that for each conformation there existed 10 modes based exclusively upon C-H vibrations. What was also noted, however, was that these modes were heavily coupled, with the atomic motions spread across large regions of the leucine molecule. These two complicated factors justify the choice of leucine as a model compound, as they would negate the possibility of applying the same procedure as was outlined in Chapter 2.

In order to fit these deceptively simple appearing spectra based on the information gathered thus far, a new computational fitting routine will be required. From the quantum chemical calculations and the related determinations of $\alpha^{(2)}$ as per the previously described method [208] it was apparent that the 5 different conformers should have very different spectral responses. Thus, it is logical to assume that some combination of these 10 populations, standing and laying for each of the 5 conformers, would result in an optimal

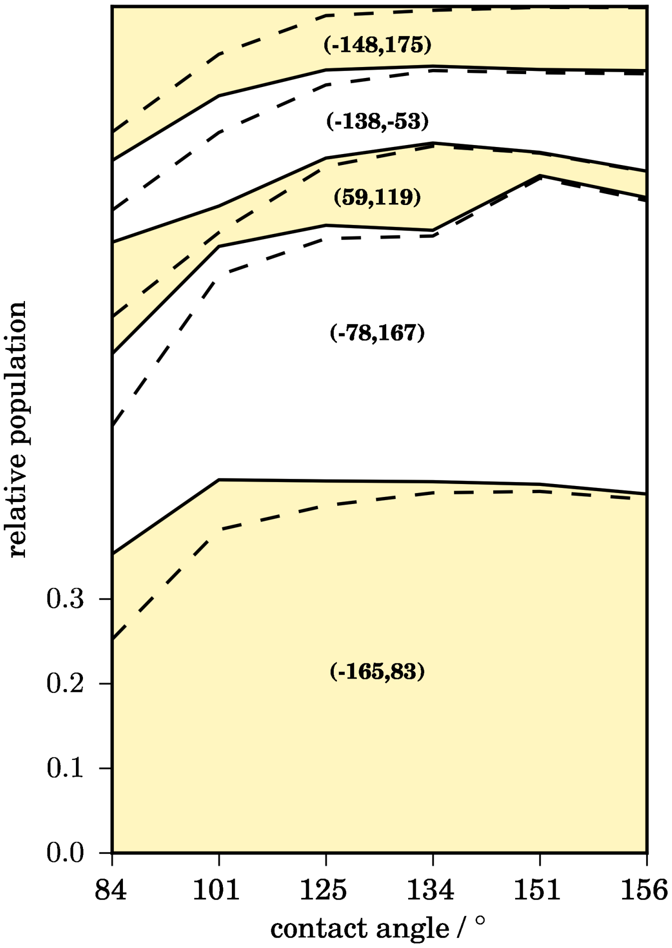

Figure 3.11: This stacked bar graph describes the variation in the relative populations of the 5 conformations identified at the surfaces of varying hydrophobicity, as defined by their water contact angle, obtained from MD simulations. The population below the dashed lines belong to the standing portions while that between the dashed lines and nearest solid line describes the laying proportion of that isomer. Varying regions of yellow and white are to provide contrast only.

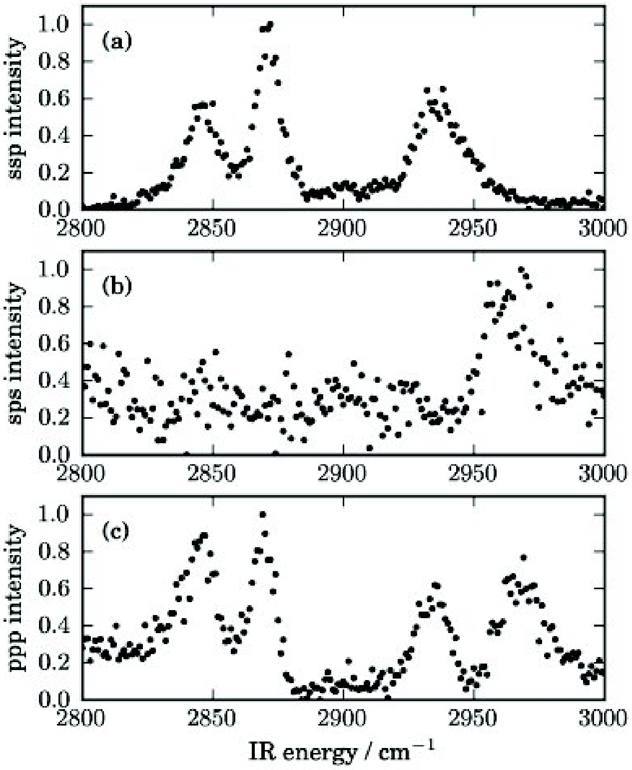

Figure 3.12: Acquired SFG spectra of leucine adsorbed at the deuterated polystyrene/D_2O interface. The spectra have been obtained in 3 different polarization configurations for the SFG, visible, and infrared radiation, specifically ssp (a), sps (b), and ppp (c).

spectral prediction.

$$\chi^{(2)}_{total}(\omega_{\mathrm{IR}}) = \chi^{(2)}_{\mathrm{NR},lmn} + P_i^{5,(s,l)} \times \sum_{\nu} \frac{a_{\nu,i}}{\omega_\nu - \omega_{\mathrm{IR}} - i\Gamma_\nu} \tag{3.10}$$

Within Equation 3.10 there is one additional term, $P_i^{5,(s,l)}$, which defines the fractional population of each of the 5 conformations in either their standing or laying form. This will form the basis for how we will determine different predictions for $\alpha^{(2)}$ and, subsequently, obtain fits to our acquired spectra. The values of $\alpha^{(2)}$ for each individual conformation were calculated by looking at each snapshot of the molecular dynamics data from all of the surfaces and determining whether the molecule was at the surface. If the molecule was indeed adsorbed, by calculating the tilt angle of the long axis of leucine, the laying molecules were then separated into standing and laying. At this point the two dihedrals, ξ_1,ξ_2, were calculated, and the molecules were selected as belonging to one of the 5 families of conformations. Based on this conformation, an addition to the running sum of $\alpha^{(2)}$ for that conformation was made. In the end, 10 separate amplitudes for each of the peaks present in the SFG spectrum were obtained for each conformation in both standing and laying orientations. These were then divided by their total populations in their particular conformation in order to allow for our fitting procedure to apply different relative populations of each species in order to fit the SFG spectra.

Additional information regarding the SFG spectrum is known, based on an experiment studying the structure of leucine adsorbed at the air/water interface [82]. From this study, it is known that there exist two Fermi resonances in the spectrum, present at 2889 and 2930 cm^{-1} respectively. Finally, there is a necessity to scale the frequencies for the infrared absorptions calculated by ab-initio methods. Several attempts were made at fitting with a variable scaling factor, but the end results were unacceptable. The decision was made to fix the highest and lowest peaks for each of the conformers at those defined in Ref. 82 at 2850 and 2963 cm^{-1}, while scaling the peaks between these two according to a sliding scaling factor defined by those applied to these extrema. This range was generally between

0.94 and 0.97, consistent with the accepted range of correction factors for the basis set and method used in this study.

It is now possible to describe the overall fitting routine. First, using random number generation, population ratios for each conformer in both standing and laying orientations are produced and normalized such that their sum is equal to one. These fractions are applied according to Equation 3.10 and using the previously described values for the approximated $\alpha^{(2)}$ values in the correct frame of reference, relative amplitudes of each of the peaks are obtained for that particular population distribution. Since there still exists the need for a non resonant contribution for each of the 3 polarization configurations as well as Fermi resonance amplitudes, phases, and positions, these are generated randomly within a defined parameter space as well. Based on this collection of parameters, an initial error value can be determined by comparing the predicted spectra to those found in Figure 3.12. The 3 polarization configurations are weighted according to their variability at a point where no resonant absorption is measured. This is calculated by measuring the standard deviation of the signal in each of the 3 polarization configurations in a region between 2800 and 2815 cm^{-1}, resulting in the contribution to the error from the SPS and PPP being divided by 8.27 and 3.00 respectively. This error value is then compared to a list of the lowest errors that have already been stored and if the current error value is lower than the greatest error value on that list, it and all its associated parameters are saved. Due to the high dimensionality of this parameter space, it is necessary to perform this operation many times over. Once a suitably large number of iterations have occurred, the final list of the parameters associated with the lowest errors is passed on to a steepest descent minimization for the nonresonant and Fermi resonant components only. Attempts were made at applying a steepest descent minimization to the relative populations, but all methods applied were unable to cope with the high dimensionality of the problem.

As an initial test for this methodology, best fits were obtained for each of the conformers in purely standing and laying orientations separately. This was done in order to gauge the

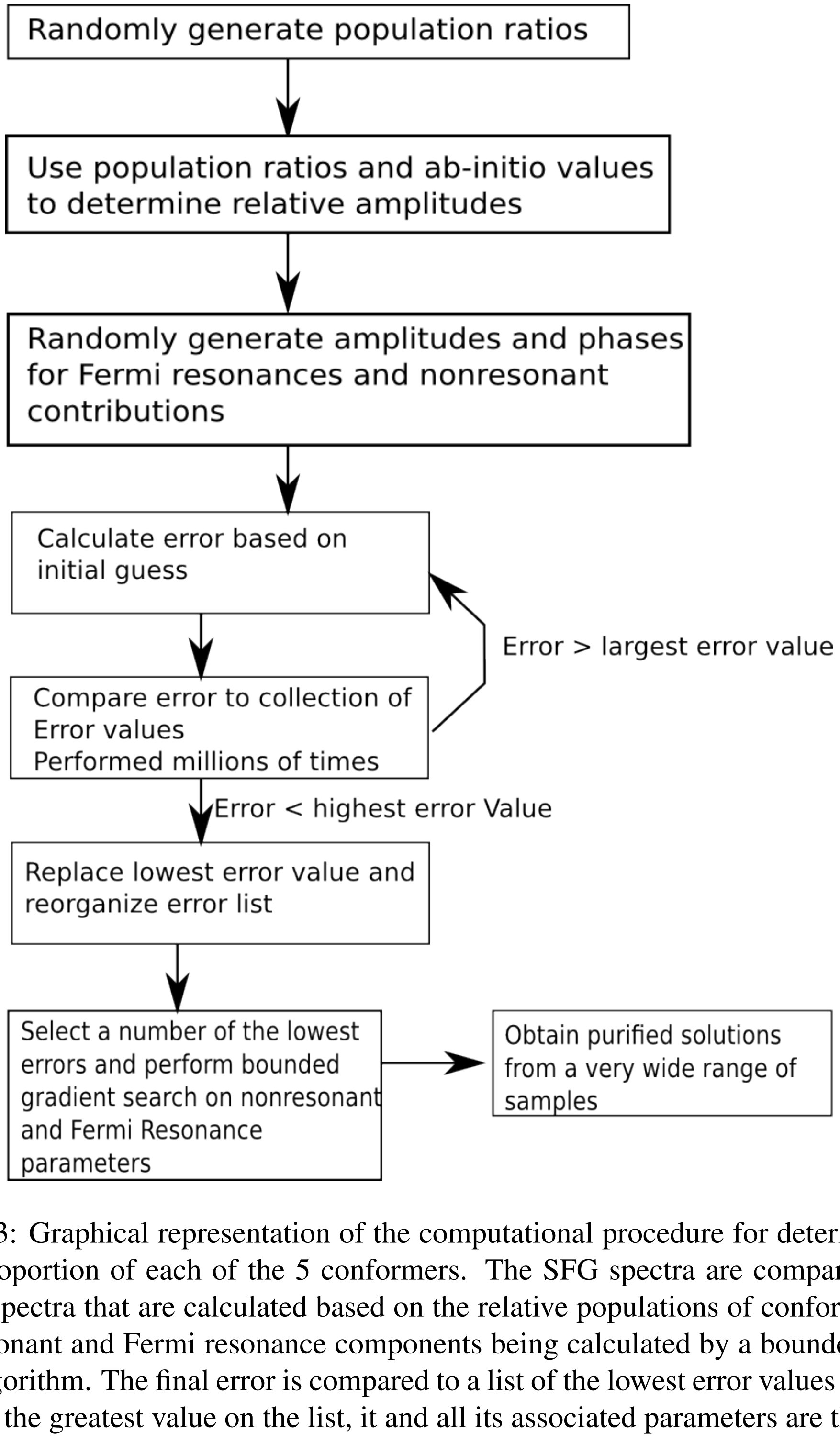

Figure 3.13: Graphical representation of the computational procedure for determining the optimal proportion of each of the 5 conformers. The SFG spectra are compared against predicted spectra that are calculated based on the relative populations of conformers, with the nonresonant and Fermi resonance components being calculated by a bounded steepest descent algorithm. The final error is compared to a list of the lowest error values and, if it is lower than the greatest value on the list, it and all its associated parameters are then saved.

efficiency of the method and in order to ascertain the similarities between the individual predicted spectral responses and the actual SFG spectra. The results are summarized graphically in Figure 3.14.

The point of interest that is immediately apparent upon viewing Figure 3.14 is just how drastically different each of the individual spectra are. Within a single conformer, between standing and laying, the variation is generally less pronounced, but between conformers the differences are striking. It is also quite obvious that the predicted spectra based on the ($\xi_1 = -138°$, $\xi_2 = -53°$) and ($\xi_1 = -165°$, $\xi_1 = 83°$) appear to most closely resemble the acquired SFG spectra. In future conformations will be referred to as (ξ_1,ξ_2) for simplicity. A final point in this case that must be emphasized is that these spectra are excellent descriptions of why a method such as this is necessary. From an initial perusal of the acquired SFG spectra, one can define 4 bands at most in the PPP spectrum. What is impossible to guess is that these 4 bands arise from 10 individual vibrational absorptions along with two Fermi resonances, making the lineshapes remarkably convoluted and the extraction of information directly from the spectra extremely difficult.

The next logical step was to determine the best possible fits to the acquired SFG spectra by allowing the individual conformers to vary their proportion of standing to laying during the fitting process. These results are shown in Figure 3.15. The (-138,-53) and (-165,83) have, by far, the closest fits to the actual SFG spectra, but they still contain noticeable defects. At this point, it has been shown that the fitting routine is working and now must be unleashed on the entire fitting problem, varying all 10 relative populations in order to fit the spectra.

What can be noted from Figure 3.16 is that modestly good agreement can be found between the predicted spectra and those obtained by experiments. However, it must be noted that the computational time required to reach this point was considerable, with the approximate 10 billion iterations of the sequence described in Figure 3.13 over a matter of months. What was disconcerting at this point though was that the lowest

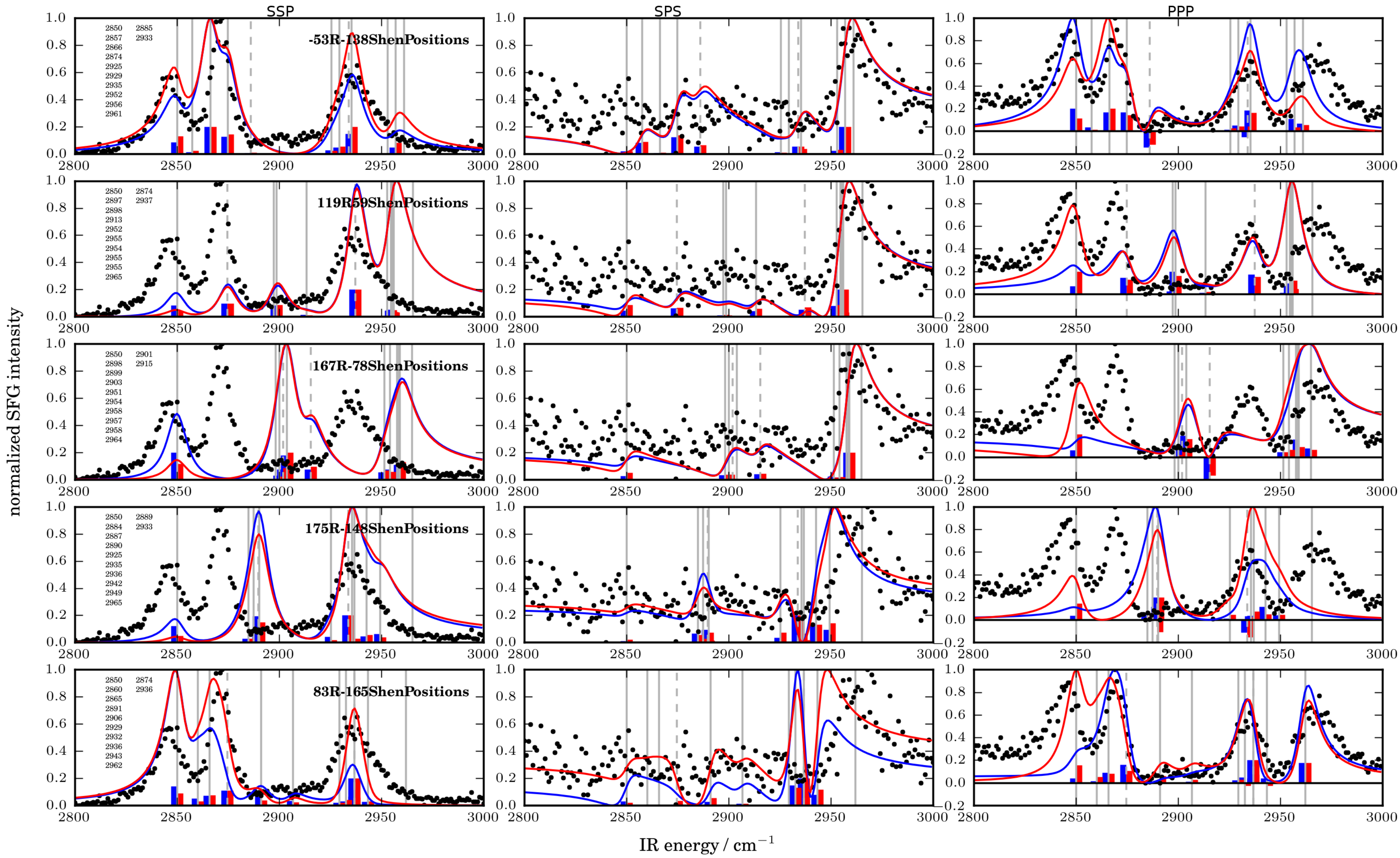

Figure 3.14: Predicted SFG spectra for the 5 different conformers of leucine present at the interface. Blue traces describe the standing molecule while the red traces describe the spectral response for the laying molecules. The solid, grey, vertical lines define the centers of the peaks obtained from quantum chemical calculations. The dashed, grey, vertical lines define the positions of the two Fermi resonances known to exist in the spectra.

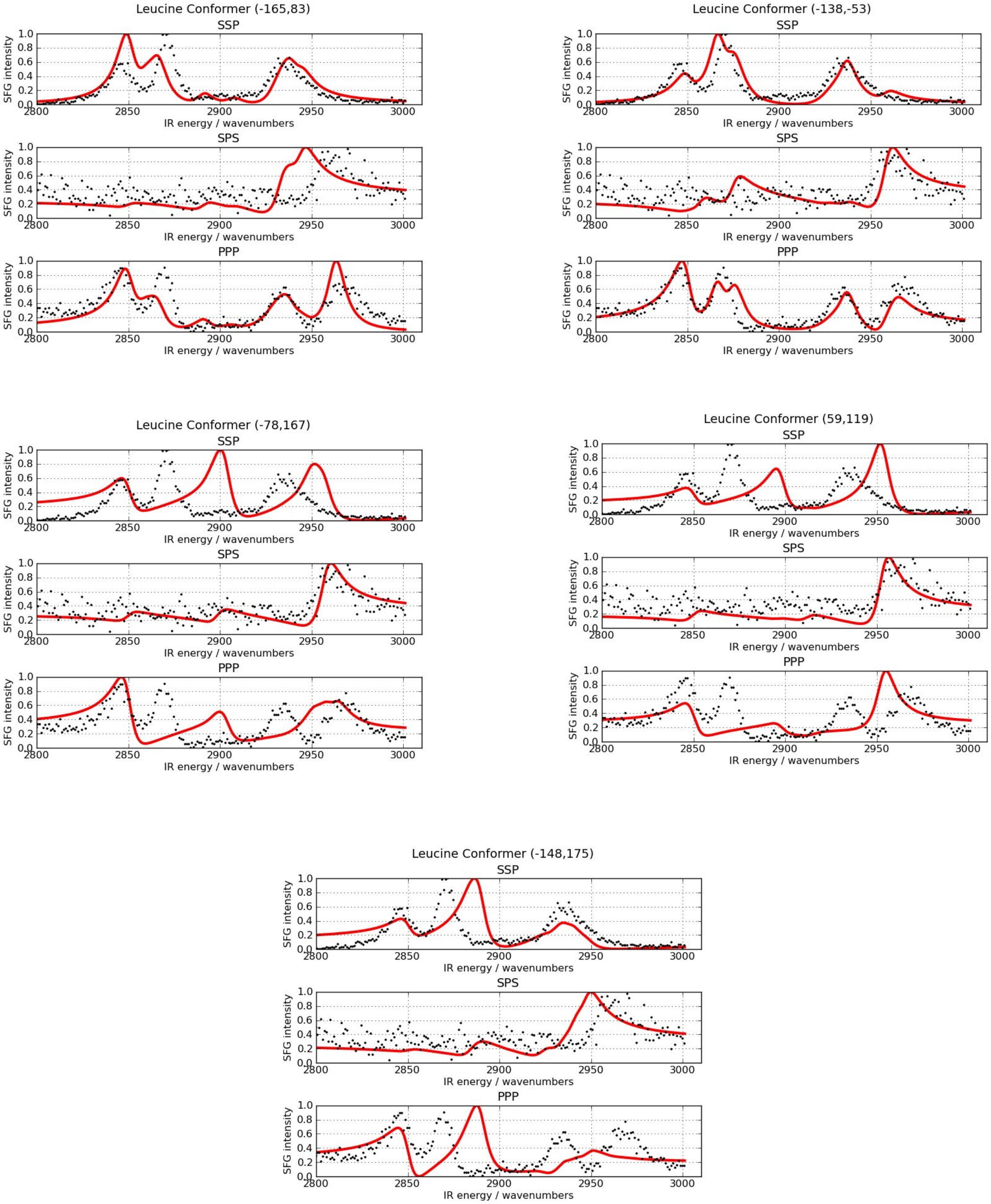

Figure 3.15: The best fits for each of the individual conformations. For these fits, only the difference in population between standing and laying conformers was varied. It is easily inferred that the (-138,-53) and (-165,83) conformers most closely match the acquired spectra.

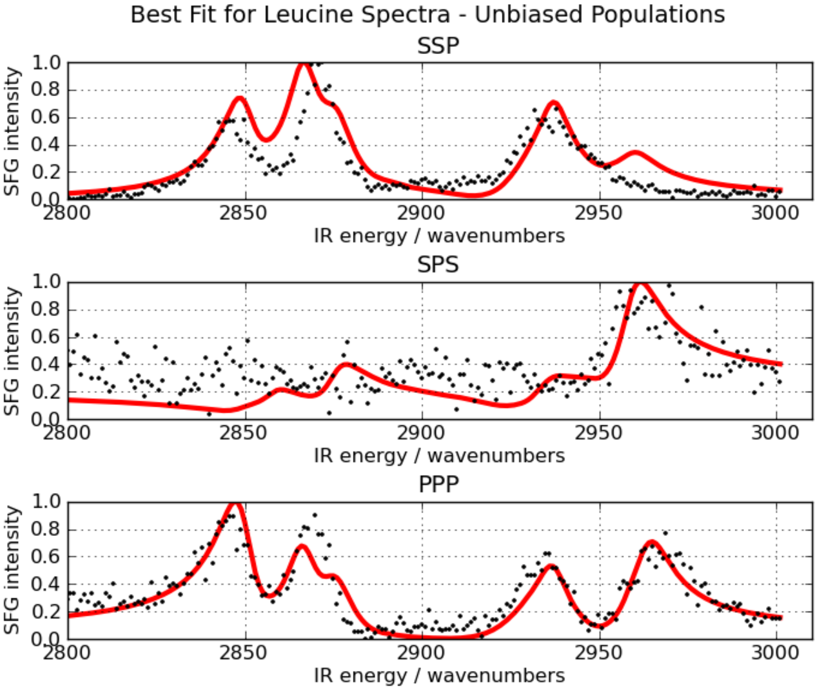

Figure 3.16: The best fits to the acquired spectra obtained through approximately 10 billion random collections of the relative populations of all 5 conformations.

error obtained, 5.628, was still greater than that which could be obtained by allowing the (-138,-53) alone to vary its standing to laying populations, with a minimum error of 5.116. This is understandable considering the high dimensionality of the problem under analysis. However, from the information obtained by inspecting Figure 3.15 it is possible to intelligently guide the calculation to sample populations that would result in a lower error. Since the (-138,-53) and (-165,83) provide the closest predicted spectra, it would be logical to bias the calculation in favour of having large proportions of these conformers. This is accomplished by simply multiplying their random number generated between zero and one by an arbitrary factor to improve the sampling of higher proportions of these species. The random population for the (-138,-53) was multiplied by 8 while that of the (-165,83) was multiplied by two. The results are found in Figure 3.17.

The improvement is noticeable, with a drop in the overall error to 4.670, a value appreciably lower than that which was obtained for both the entirely unbiased results and those obtainable from the single (-138,-53) and (-165,83) conformer analyses. These values were also found in approximately half the time as was required to perform the completely unbiased analysis, showing the importance of an intelligent selection of boundaries for the parameters in this analysis. As a final test, a set of fitting runs was performed with only the two best conformers,(-138,-53) and (-165,83), present.

The improvement in these fits is marginal, with the overall error decreasing from the biased results on the order of 2.6%. It is inferred, therefore, that the biased results were converging upon this point, making an excellent case for performing the analysis sequentially in this fashion in order to determine the global minimum and optimum parameters in an acceptable timeframe. The relative populations and optimal parameters for the two most important individual conformers as well as the unbiased, biased, and (-138,-53) and (-165,83) alone studies are presented in Table 3.2.

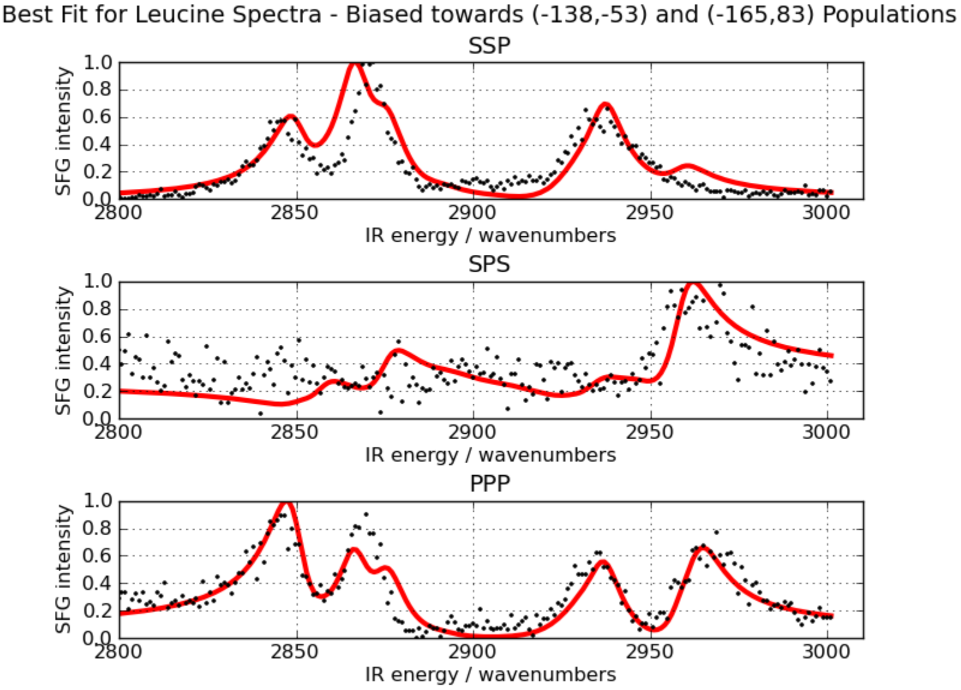

Figure 3.17: The best fits obtained through approximately 5 billion random collections of the relative populations of all 5 conformations, with the populations of the (-138,-53) and (-165,83) artificially biased through the application of a multiplicative factor to their randomly generated populations. The (-138,-53) is weighted roughly 8 times more and the (-165,83) twice as heavily as the other conformations. No bias was installed between the standing and laying conformations themselves.

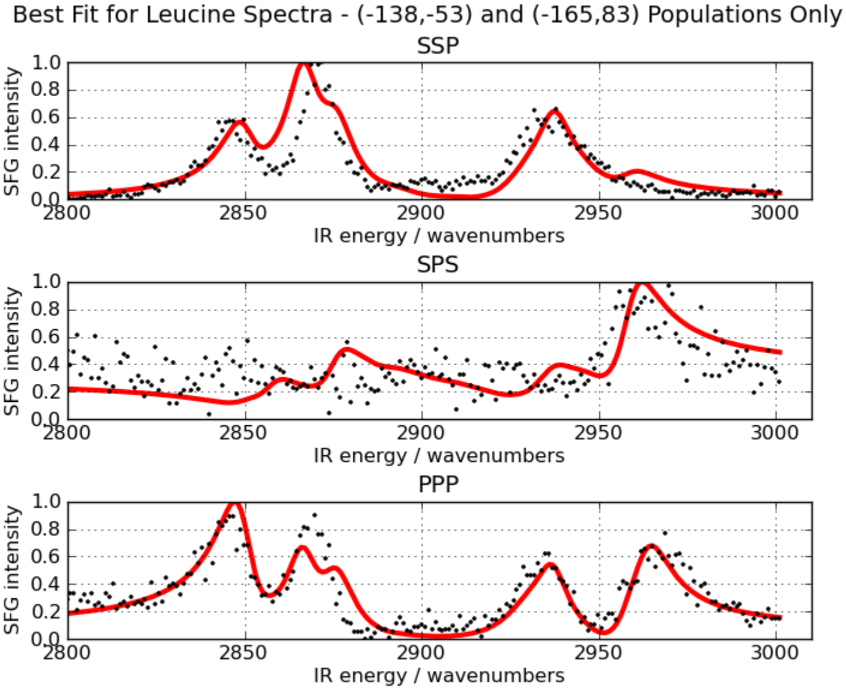

Figure 3.18: Fits to the acquired SFG spectra of leucine generated with contributions only from the (-138,-53) and (-165,83) conformers through approximately 2 billion calculations.

	(-165,83)	(-138,-53)	All Unbiased	All Biased	(-138,-53) (-165,83)
Lowest Error	9.857	5.1160	5.628	4.697	4.547
P_{Standing}	0.289	0.886	0.670	0.854	0.932
P_{Laying}	0.711	0.114	0.330	0.146	0.068
$P_{119,\text{Standing}}$	0.000	0.000	0.014	0.007	0.000
$P_{83,\text{Standing}}$	0.289	0.000	0.198	0.121	0.201
$P_{175,\text{Standing}}$	0.000	0.000	0.006	0.021	0.000
$P_{-53,\text{Standing}}$	0.000	0.886	0.445	0.690	0.730
$P_{167,\text{Standing}}$	0.000	0.000	0.007	0.014	0.000
$P_{119,\text{Laying}}$	0.000	0.000	0.025	0.002	0.000
$P_{83,\text{Laying}}$	0.711	0.000	0.043	0.067	0.055
$P_{175,\text{Laying}}$	0.000	0.000	0.028	0.004	0.000
$P_{-53,\text{Laying}}$	0.000	0.114	0.203	0.064	0.013
$P_{167\text{Laying}}$	0.000	0.000	0.031	0.010	0.000
NR Amp SSP / $10^{-}3$ au	-0.206	-0.156	-0.3	-0.158	-0.258
FR 1 Amp SSP / $10^{-}3$ au	-2.27	-1.69	-1.60	1.09	-0.356
FR 2 Amp SSP / $10^{-}3$ au	-2.26	1.78	-2.19	1.31	0.934
NR Amp SPS / $10^{-}3$ au	-5.97	-5.95	-4.03	-5.34	-5.71
FR 1 Amp SPS / $10^{-}3$ au	-0.929	0.743	-1.50	-0.414	0.552
FR 2 Amp SPS / $10^{-}3$ au	-1.92	-1.06	-0.271	-1.77	-1.43
NR Amp PPP / $10^{-}3$ au	-1.32	-2.64	1.84	-2.06	2.05
FR 1 Amp PPP / $10^{-}3$ au	0.464	1.51	0.891	-1.42	-0.941
FR 2 Amp PPP / $10^{-}3$ au	-1.73	-2.25	-0.209	-0.812	0.555
NR Phase PPP /rad	3.61	1.55	-1.60	1.54	-1.57
FR 1 Phase PPP	0.365	-1.40	-1.42	1.52	2.01
FR 2 Phase PPP	-1.76	-3.37	0.583	-2.00	-0.104
FR 1 Position /cm^{-1}	2893	2886	2890	2897	2891
FR 2 Position /cm^{-1}	2939	2937	2939	2938	2944

Table 3.2: Tabulated values for relative populations and optimal parameters for the various modifications to the fitting routine.

Relative Energy / kJ/mol	(-165,83)	(-148,175)	(-138,-53)	(-78,167)	(59,119)
Relative Energy / kJ/mol	1.84	13.22	15.23	0.0	11.09
Lowest Error	9.857	19.183	5.116	24.814	19.600
Total Standing Fraction	0.289	0.886	0.670	0.854	0.932
Total Laying Fraction	0.711	0.114	0.330	0.146	0.068

Table 3.3: Table relating the energies of the individual conformers, relative to the lowest energy conformer, as determined through electronic structure calculations. These values are compared with the error of the best fit of each individual conformer and the associated standing to laying ratio to highlight the interaction between the internal energy of the molecule and the effects of solvent and discrete leucine-surface atom interactions that result in the preferences for the (-165,83) and (-138,-53) conformations.

3.6 Discussion

The main goal of this undertaking has been to obtain a sense of the physical orientation of leucine adsorbed at the polystyrene interface, without the prior knowledge of its vibrational assignments. While this has been accomplished, with there being an obvious preference for the (-165,83) and (-138,-53) conformations the reasons as to why this should be the case requires careful explanation.

First and foremost, there must be some sort of energetic argument for these two conformations being preferable. Since the electronic structure calculations were formed identically and in a polarizable continuum model in order to more closely model the dielectric constant associated with being in an aqueous solution, we should be able to compare the energies of the conformers. This was done simply by measuring them relative to the energy with the lowest calculated energy, the (-78,167) conformer, with the results stored with comparable data of interest in Table 3.3.

In the most simple of cases, one could make an assumption that the conformer with the lowest energy should be the most favourable. This is almost the case with regards to that of the (-165,83) conformer, being a mere 1.84 kJ/mol higher in energy than the lowest conformer, but the conformer with the highest predicted proportion from the comparison of these structures to the actual leucine SFG spectra, the (-138,-53) conformer, is in

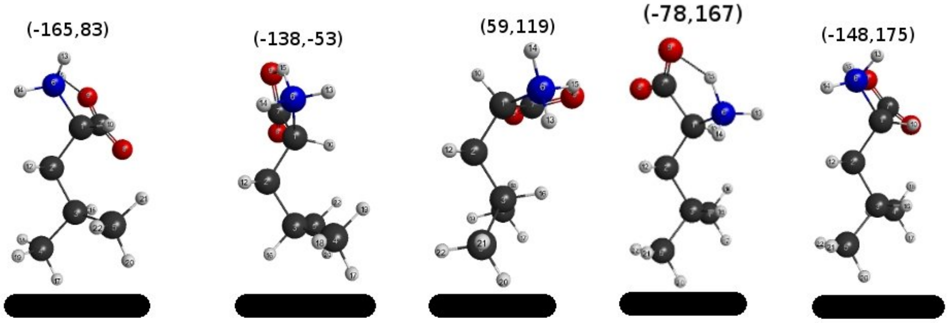

Figure 3.19: All 5 conformations of leucine known to exist when adsorbed to the surfaces studied through molecular dynamics simulations. Focusing upon the CH_2 plane, these molecules all show a tilt of 90° to the hypothetical surface normal, thus making them representations of the molecule in its standing orientation.

fact the conformer with the greatest overall energy at 15.23 kJ/mol with respect to the lowest energy conformer. At this point, the solution to this problem must require a more advanced analysis. While the PCM may be useful as a first order approximation to an aqueous solution, it will lack the discrete solvent-molecule interactions that exist in a real solution. More importantly than this, at the interface between the solution and the polystyrene surface other effects will be of great importance as well, including molecule-surface interactions. Thus, the conformers require a closer analysis as well, with a focus on their standing and laying orientations.

In the case of the fits that resulted in the lowest overall errors, those being the runs involving contributions from all conformers with the proportions of the (-165,83) and (-138,-53) conformations biased to be larger and the runs involving contributions solely from the (-165,83) and (-138,-53) conformations showed a greater proportion of standing molecules at the surface. This is quite predictable, as it would provide the maximum separation of the relatively nonpolar and hydrophobic alkyl sidechain of the leucine molecule and the charged carboxylate and amino groups. This conformation would also point the resultant dipole of the molecule more directly towards the solvent, which would be energetically favourable provided water molecules oriented their dipoles in the opposite direction. Upon inspection of the (-138,-53) standing conformations in Figure 3.19 one notices that its -$CH(CH_3)_2$ region is almost coplanar with the hypothetical surface. This conformation is unique in this regard, with all other conformations possessing a -$CH(CH_3)_2$ plane nearly perpendicular to the surface. This unique property of the (-138,-53) standing conformation would maximize the hydrophobic interactions with the relatively nonpolar, aromatic polystyrene surface. This conformation also aims its polar carboxylate and amino groups directly towards the solvent. It is postulated that these two unique characteristics of the (-138,-53) standing conformation result in this molecular form being so favoured, even though it exists at a higher energy than any of the other conformations.

The preference for the (-165,83) conformer in the standing conformation is based on a similar argument. This molecule does have at least both methyl groups pointed towards the surface, thus ensuring strong hydrophobic interactions, at the same time as having the amino group pointed towards the solvent. However, for this conformer, the energetic barrier is much lower, at only 1.84 kJ/mol greater than the most stable conformation. While its structure is not so well suited to this environment as the (-138,-53) conformation, its agreeable structure and lower internal energy make it another prime candidate for a preferred surface orientation. The other conformations have less desirable characteristics, such as tending to point only a single methyl group down towards the surface, causing decreased hydrophobic interactions with the surface, as well as not pointing their charged groups well into the solvent.

By looking at the laying orientations of the 5 conformers, as shown in Figure 3.20, similar conclusions can be reached. Again, the (-138,-53) conformer has superior potential for hydrophobic interactions, as is exhibited through its unique structural ability to point two methyl groups down towards the surface. While the two polar regions are relatively coplanar with the surface, they are separated from the likely point of contact with the surface, the -$CH(CH_3)_2$ region, allowing for solvation of these groups. This is likely

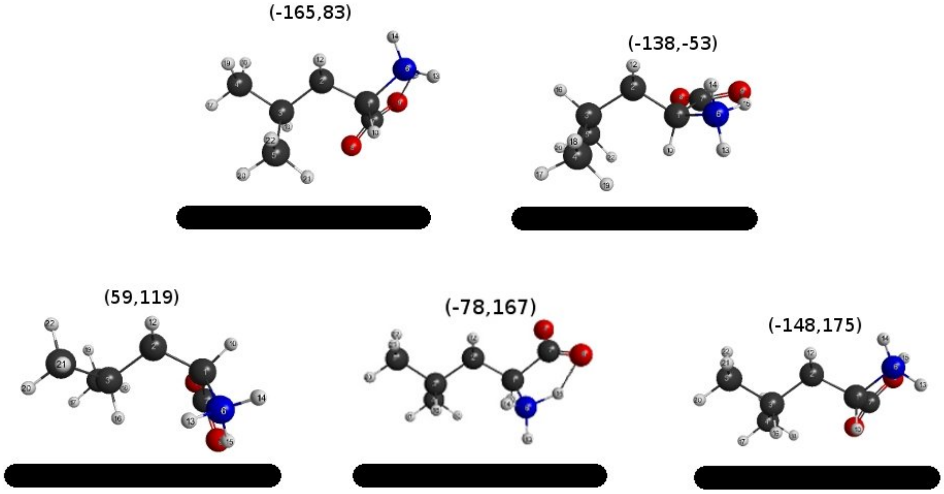

Figure 3.20: All 5 conformations of leucine known to exist when adsorbed to the surfaces studied through molecular dynamics simulations. Focusing upon the CH_2 plane, these molecules all show a tilt of 0° to the hypothetical surface normal, thus making them representations of the molecule in its laying orientation.

sufficient to overcome the increased energy of this conformer and make this conformer favourable. For the (59,119), (-78,167), (-148,175) conformers, the molecules adopt configurations wherein the leucine lays very flat on the surface. These orientations lack the necessary separation between their hydrophobic and polar regions that would allow for effective hydrophobic interactions with the surface and solvation of the ionic moieties. This is the most logical reason for their low determined relative popularions. While the (-165,83) only points 1 methyl group directly at the surface, it still possesses a better separation of these regions, which along with its low internal energy favour the adoption of this conformation.

3.7 Conclusions

A methodology for the determination of the relative population of conformers at surfaces based on molecular dynamics simulations and sum frequency generation spectroscopy has been developed. The method has been applied to an example system wherein the structure of leucine adsorbed to a polystyrene surface was determined. This system was selected as the SFG spectra of leucine at a surface is known to be extremely complex, making accurate assignments of any of the vibrational modes present difficult. The determination of surface structure was facilitated through the development of a fitting routine that calculated predicted SFG spectra based on the populations of several conformations of leucine adsorbed at various hydrophobic dielectric surfaces identified from molecular dynamics simulations. In the case of leucine, 5 conformations were identified at the surface, existing either in an standing or laying orientation at the surface. The predicted SFG spectra that most closely matched those obtained experimentally were those calculated based on the highest percentages of two conformers, defined by two dihedral angles in Figure 3.8, (-138,-53) and (-165,83). It was determined that molecules that are standing at the surface, with their alkyl groups pointed towards the surface and their charged amino and carboxylate groups pointed towards the solvent are highly favoured. The two structures that dominate the populations are those that possess the greatest contacts between their alkyl regions and the hydrophobic surface while maintaining an orientation in which their charged groups point directly into the solvent. It was discovered that one of these conformations, (-165,83), was very close in energy to the most stable conformation present, (-78,167), while the other, (-138,-53), possessed the greatest relative energy of all 5 conformations. As such, it is postulated that the structure of the (-138,-53) is stabilized at the surface due to its unique conformation of its alkyl region allowing for the greatest contact with the hydrophobic surface. This highlights the importance of the difference in overall energetic environments between solution and the interface. In terms of the laying conformations, the (-165,83) was most favoured, most likely as a result of the combination of its low relative energy and its conformation that allows considerable separation between its methyl group pointing towards the surface and its charged groups. In this case, even though the (-138,-53) also has appreciable separation between the hydrophobic surface and its charged groups, it is likely that the relative energy of the (-138,-53) is greater than the stabilization incurred when adsorbed to the surface in this conformation.

This initial study using this methodology shows great promise as it possible to obtain structural information from SFG spectra without the assignment of the vibrational modes using molecular dynamics simulations and the results are consistent with basic chemical principles. It is hoped that through a similar process, this methodology could be used on larger molecules, such as proteins.

Chapter 4

Mueller Matrix Ellipsometry and Stokes Vector Polarimetry

4.1 Overview

The characterization of chemical species at interfaces has long been performed with the aid of carefully controlled or analyzed radiation interacting with the species of interest at the position of interest. This is useful as many methods are capable of being surface selective, such as sum frequency generation spectroscopy. However, in the case where the system of interest is anisotropic, inhomogeneous, or depolarizing many methods lack the rigourous analysis required to extract specific information regarding the nature of the species of interest from the heavily convoluted signal. In most cases, Stokes polarimetry is sufficient to accurately describe the system of interest and with the advent of the photoelastic modulation of light, very precise measurements of optical parameters can be obtained at very fast rates. When depolarizing effects do occur though, frequently the best solution involves the invokation of Mueller calculus and the analysis of the Mueller matrix of the sample, which is capable of successfully encoding both the sample information and the depolarization information [104, 112, 113].

Several experimental methods have been employed for the analysis of optical systems by ellipsometry, and have been reviewed extensively [105–107]. Originally, optical parameters were obtained from simple null-ellipsometers that obtained the ellipsometric parameters Ψ and Δ through the nulling of a signal from a sample, accomplished by rotating the polarizer and compensator before the sample such that the elliptically polarized light incident on the sample is reflected as linearly polarized light that is nulled when incident on an analyzer perpendicular to it. This method, while remarkably accurate, requires time to accurately null the signal, even if this process is automated. Another drawback inherent in this method is that it is only capable of determining these two parameters, and not the full Mueller matrix. At the next level of complexity exists the rotating element ellipsometer. These systems, generally constructed in the form of polarizer-compensator-sample-analyzer or polarizer-sample-compensator-analyzer configurations, provide some modulation in the polarization of the light incident or excident to the sample of interest. As such, a number of pairs of Ψ and Δ are obtained, from which information regarding the sample can be obtained. If performed by hand, individual pairs can be obtained, or if automated a large number of stationary points can be obtained or with constant rotation and frequency based detection, Ψ and Δ can be obtained directly. Closely related to this instrument is the rotating compensator ellipsometer, that functions in a similar fashion. These rotating element ellipsometers, while faster than null ellipsometers, contain similar drawbacks. In terms of rotating element based Mueller matrix ellipsometers, there exists examples based upon the employment of dual rotating compensators [108–110]. While effective, these systems require incredibly stable rotation of the compensators at very specific frequencies for real-time detection or a stepwise rotation of the compensators in order to produce the waveform followed by mathematical processing in order to determine the Mueller matrix.

Real-time Ψ and Δ measurements are most readily determined from high speed polarization modulation by virtue of the employment of photelastic modulators as the polarization modulating element. Through various implementations, these PEM based ellipsometers are capable of performing as Stokes polarimeters [122–125] capable of determining Ψ and Δ at very high speeds and as Mueller matrix ellipsometers [126–128].

These systems, again, have some rather difficult technical requirements in order to utilize them effectively, such as acquiring waveforms based on synchronized PEMs performing at kilohertz frequencies, requiring data obtained in multiple orientations of the ellipsometric configuration, or the use of up to 8 lock-ins simultaneously synchronized to various sums, multiples, and differences of the PEM operating frequencies.

Despite all of these inherent difficulties in Mueller matrix ellipsometry, it is remarkably useful as it is capable of the complete analysis of complex systems, such as liquid crystals [129, 130] and protein adsorption to a variety of surfaces [120, 131–135]. It is also known that the structure of proteins is heavily affected by the nature of the surface it is adsorbing to and the solution conditions in which it is initially [12, 58, 216, 217]. However, it is also known that surfaces consisting of adsorbed protein layers are generally rough and depolarizing. Even though this inherent difficulty exists in studying these systems, they are of vital interest to biology and medicine, as they are the at the roots of the processes of biofouling [31] and implant compatibility [218], and haemocompatibility [14, 15, 117]. The adsorption of proteins to a surface in contact with blood is known to be the first even that occurs, followed by coagulation, thrombus formation and embolization. An accurate understanding of the mechanism of this initial event is vital to the design of implant materials that avoid these negative consequences.

In order to study these complex systems despite the problems mentioned, it is important to note that the two aforementioned techniques become complementary: Stokes polarimetry providing high speed information on the changing physical and optical constants of the growing monolayer as it forms including the development of depolarization while Mueller matrix ellipsometry can be employed when the adsorbing system reaches a steady state allowing for the extraction of all information specifically pertaining to the adsorbed layer of protein. It is in this cause that a system capable of interchangably performing as high speed and high precision dual-PEM based Stokes polarimeter and an accurate Mueller matrix ellipsometer as well as the necessary calibration procedure has been developed.

4.2 Materials

The material of choice for our prisms was fused silica (Del Mar Phototonics, San Diego CA) with the incident and exit faces of the prism used for the current experiments are cut at the desired angle of incidence (70°) so the beam approaches the air-fused silica interface and leaves the fused silica-air interface at normal incidence, simplifying analysis of the polarization change at the sample interface.

Prior to use, the prism was cleaned by dipping in a solution of 0.1 v/v% nitric acid in sulfuric acid, followed by copious rinsing in 18 $M\Omega$ deionized water (Nanopure, Barnstead Thermo). The three prism surfaces of interest were lightly polished using a 3 μm polycrystalline diamond suspension (Buehler Metadi supreme), followed by 0.05 μm silica suspension (Buehler Masterprep) and again rinsed with deionized water. Prior to assembling the sample cell, a deuterated d_8-polystyrene (MW 270 500 g/mol, PDI 1.25 from Polymer Source, QC) film was applied to the backside of the prism by spin coating (Model G3-8, Specialty Coating Systems, IN) from a 2 w/w% chloroform solution for 90 s at 1500 rpm, then drying covered overnight covered at room temperature.

Bovine serum albumin (MW 66430 g/mol, lyophilized powder $\geq$ 96% Sigma) solutions were made by dissolving 626.9 mg of powder in PBS (1X Dulbecco's formula without magnesium, MPBio) which was produced by dissolving one previously prepared tablet containing 20 mg KCl, 20 mg KH_2PO_4, 800 mg NaCl and 115 mg Na_2HPO_4 in 18 $M\Omega$ deionized water.

4.3 Instrument Overview

A schematic of the instrument appears in Figure 4.1. The current configuration is suitable for any single fixed wavelength. On the incident arm, we use a 632.8-nm HeNe laser (Thorlabs HRP170) as a light source. A low frequency modulation (about 1 kHz) is then

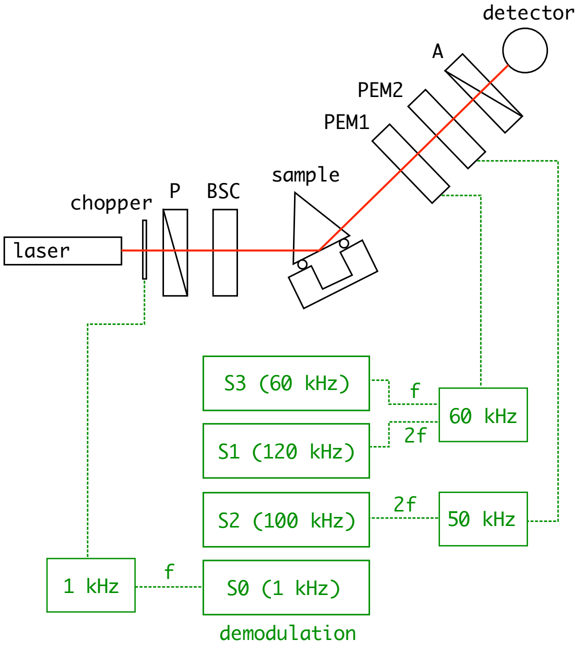

Figure 4.1: Schematic of the optics (black) and electronics (green) of our instrument. A 632.8-nm HeNe laser is modulated by a mechanical chopper at 1 kHz. The light then passes through a polarizer and Babinet-Soleil compensator (BSC) before approaching the sample interface through a prism. Reflected light passes through a 60 kHz photoelastic modulator (PEM1), 50 kHz photoelastic modulator (PEM2), analyzer (A), and is collected on a high-speed Si photodiode. The signal waveform is demodulated at the fundamental and harmonic components of the input frequencies by four lock-in amplifiers.

applied by a mechanical chopper (Thorlabs MC1000A) with a 30-slot blade. The light then passes through a calcite Glan Taylor polarizer (Thorlabs GT10) with polarization ratio better than 200,000:1. Finally the light passes through a Babinet-Soliel compensator that has been set to $\lambda/4$ retardation for our working wavelength. This comprises the polarization state generator (PSG) arm of the instrument. A diagram of our custom sample compartment appears in Figure 4.2. It consists of a teflon cell housed in an aluminum block. The front face of the teflon cell is in contact with a fluoropolymer o-ring (Marco Rubber, Seabrook NH) pressed against a prism that can be coated with the polymer of choice.

The polarization state analyzer (PSA), our Stokes polarimeter, consists of two fused silica photoelastic modulators (Hinds Instruments, Hillboro OR), anti-reflection coated for

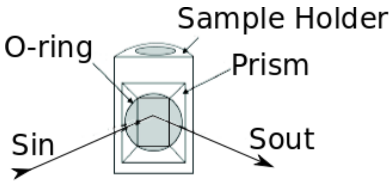

Figure 4.2: Schematic of the sample holder used for the Stokes Polarimeter. The teflon sample holder is equipped with a cap containing a stirrer motor that turns a paddle within the solution itself ensuring proper mixing. The entire sample holder shown is housed within an aluminum block that has been machined to allow for water flow through it, allowing for maintenance of sample temperature

wavelengths 400-700 nm. The crystal in the first modulator is cut to vibrate at nominally 60 kHz; the second at 50 kHz. The light then passes through an analyzer, another Glan Taylor polarizer. Since we need to demodulate the signal at high frequencies, we use a reverse-biased amplified Si photodiode (Thorlabs DET10A) with 1 mm^2 active area and 1 ns rise time. In order to facilitate different samples/substrates with different angles of incidence, the sample and PSA are mounted on a home-built computer-controlled θ-2θ stage. The azimuths of all optical elements are controlled with stepper motors (Standa, Lithuania).

The output of the photodiode is therefore demodulated using 4 lock-in amplifiers (Signal Recovery 7265). The information that we desire is encoded in the amplitudes of the 2nd harmonic of the first PEM, the 2nd harmonic of the second PEM, and from the fundamental of the first PEM. We also measured in the DC component, obtained by demodulating at the chopper frequency. Since the highest frequency of interest is 120 kHz, we do not need all of the available bandwidth. We therefore increase our signal-to-noise with a 10 kΩ load on the detector.

4.4 Calibration Procedures

When working with optical elements, the necessity for accurate calibrations cannot be overstated. To this end, the calibration of the azimuthal alignments of each of the optics will be outlined as well as the determination of the retardation amplitudes of the photoelastic modulators as well as the Babinet-Soleil compensator will be described in detail.

4.4.1 Azimuthal Calibration of Optics

Initial, a reference polarization state is required prior to calibrating the azimuth of any other optics in our system. This is obtained by performing a Brewster's angle measurement. This procedure involves reflecting light off a surface of known refractive index, in our case a piece of flat glass with n $\approx$ 1.5, at an angle defined by the following equation.

$$\theta_{\mathrm{B}} = \arctan \frac{n_2}{n_1} \tag{4.1}$$

In Equation 4.1, θ_{B} is known as Brewster's angle and n_1 and n_2 define the refractive indices of the incident and reflecting media. In our case, $\theta_{\mathrm{B}} \approx 56^\circ$. This angle is defined by properly aligning the flat piece of glass such that its back reflection passes through the iris through which the incident beam passed as well as through an iris set up at 90° to the sample. All of our optical elements are mounted on computer controller rotation stages. As such, once a reference point is located, the flat piece of glass being perfectly perpendicular to the incident beam, the stages can be set to that reference angle, in this case 0°. From this point, they can be rotated by their computer controlled rotation stages to any angles with a resolution of 1 arcsecond. Upon moving the sample to 56°, the initial polarizer is installed in the beam path and rotated by hand to a rough minimum. This is due to the fact that at Brewster's angle only incident light that is s–polarized will be reflected, while p–polarized light will be absorbed completely. A computer program steps through a symmetric range near the minimum and collects the intensity at the detector demodulated at the chopper frequency. By fitting the intensity to a parabola, the azimuthal angle at which the minimum is observed can be calculated and the motor moved to that position. The polarizer is now at 0° with respect to the plane of incidence.

Now, the analyzer can be installed and calibrated. This is done by, again, rotating the analyzer until the intensity demodulated at the chopper frequency is at a minimum.

The program once more moves the analyzer through a small range about this point and determines the minimum. Upon moving to the azimuthal angle at which the minimum occurs the analyzer is set to 90° with respect to the plane of incidence.

Once this is performed, additional elements can be added between these crossed polarizers and the same procedure performed. Generally, they are rotated until they are near 0° and then optimized by the same program to be aligned with the initial polarizer present at 0°. This works for the Babinet-Soleil compensator, provided its retardation is not set to 0 or 2π and for the PEMs, provided that they are oscillating driven by a voltage that produces an amplitude of greater than 0. In this case, the fast axis of the BSC can be aligned with the initial polarizer and the axis of modulaton of the PEMs can be aligned.

4.4.2 Calibration of Retardation Amplitudes

First, it is necessary to determine the settings for the Babinet-Soleil compensator that provide the correct retardation ($\frac{\lambda}{4}$) for our 632.8 nm light. This form of compensator is special in that it is a continuously variable zero order retarder that is capable of operating for a wide number of wavelengths. The process by which it retards light is based upon passing the light through variable widths of a birefringent material. The normal construction of this form of compensator involves a long birefringent wedge, that can be moved back and forth, over a fixed wedge. By varying the distance the light travels through the birefringent material, the desired retardation can be obtained. Practically, this is performed by rotating a micrometer dial that, in turn, pushes the long wedge along the fixed wedge.

The calibration of this retardation is fairly simple. The Babinet-Soleil compensator is placed between crossed polarizers at 45° with respect to the initial polarizer. The micrometer dial is then moved, starting at the minimum position of the micrometer, until the intensity is at a minimum. At this point, the compensator is functioning at a retardation of 0. The micrometer is then moved again until a second minimum is reached, which occurs at a retardation of 2π. Based on these two known distances, any fraction of retardation can be obtained. In the case of our $\frac{\lambda}{4}$, which is equivalent to a retardation of $\frac{\pi}{2}$, can be obtained by moving the micrometer to a position one quarter of the distance traveled between the initial minimum, at a retardation of 0, and the second minimum, corresponding to a retardation of 2π. With the BSC now set appropriately, the amplitude of the photelastic modulators can be calibrated.

Appropriate PEM calibration factors were necessary for the production of a system capable of determining simultaneously precise and accurate polarization measurements was the amplitude of the photoelastic modulators. It has been shown [219] that with a single photoelastic modulator at $0°$ placed between an initial polarizer at $-45°$ and an analyzer at an arbitrary angle, the intensity of the output light can be broken into three components, specifically the dc component as well as the odd and even harmonics of the fundamental photoelastic modulation frequency as a function of the modulation amplitude.

$$I_{dc}(A) = 0.5I_0[\sin A^2 + \tan\Psi^2 \cos A^2 - \tan\Psi \cos\Delta J_0(\delta_0)\sin 2A] \tag{4.2}$$

$$I_{(2m+1)f}(A) = -I_0[\tan\Psi \sin\Delta J_{(2m+1)}(\delta_0)\sin 2A] \times \sin{(2m+1)\omega t} \tag{4.3}$$

$$I_{(2nf)}(A) = -I_0[\tan\Psi \cos\Delta J_{2n}(\delta_0)\sin 2A] \times \cos{(2n\omega t)} \tag{4.4}$$

From the above, it is easy to determine that ratios of either successive odd or even harmonics can be utilized to determine the value of the current modulation amplitude.

$$\frac{I_{(2m+1)}}{I_{(2m+3)}} = \frac{J_{(2m+1)}(\delta_0)}{J_{(2m+3)}(\delta_0)} \tag{4.5}$$

$$\frac{I_{(2n)}}{I_{(2n+2)}} = \frac{J_{(2n)}(\delta_0)}{J_{(2n+2)}(\delta_0)} \tag{4.6}$$

This method was attempted several times, providing inconsistent results. The cause of this was determined to be a result of the extremely high frequencies required for the demodulations of the higher harmonics, specifically 240 kHz for the 60 kHz PEM. This allowed for the use of a very small terminal resistor to the circuit, placing the signal in a range very close to the noise level of the signal used. It was determined that another method

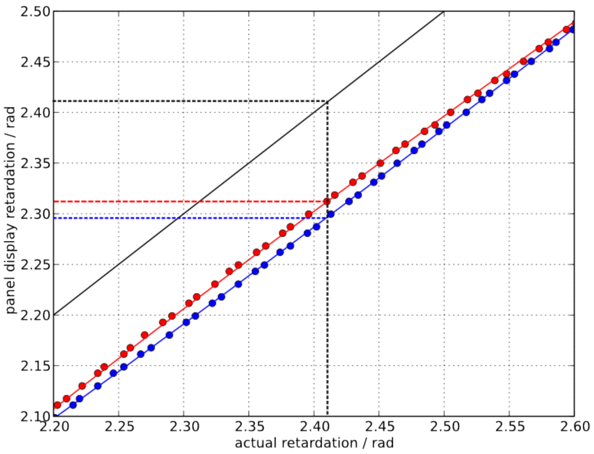

Figure 4.3: Calibration of the retardation amplitude δ_0 of each photoelastic modulator. The retardation displayed on the front panel of the controller is plotted against the best fit δ_0 obtained from the ratio I_{2f}/I_{4f} for the 50 kHz modulator in red, and the 60 kHz modulator in blue. Experimental data are plotted with points. Lines through the points are fits to a 3rd-order polynomial. Interpolations based on these fits are used to set $\delta_0 = 2.4048$ rad. The deviation of both experimental slopes from unity (solid black line) is apparent.

would be necessary in order to correctly determine the exact modulation amplitudes for our PEMs.

The solution reveals itself in analyzing the mathematic representations for the demodulation of light at specific frequencies for the determination of Stokes vectors of reflected light, the basis for the high speed Stokes polarimeter we were building. In the suggested orientation, with the second PEM at 0°, the first PEM at 45° and the analyzer present at 22.5°, the overall intensity seen at the detector is calculated as follows.

$$\begin{aligned} I_{\text{det}} &= \frac{1}{2}I_0 - \frac{1}{2\sqrt{2}}I_3 \sin\delta_1 + \left[\frac{1}{4\sqrt{2}}I_1 - \frac{1}{4\sqrt{2}}I_2\right]\cos\delta_1 + \\ &\quad \left[\frac{1}{4\sqrt{2}}I_1 + \frac{1}{4\sqrt{2}}I_2\right]\cos\delta_2 + \frac{1}{2\sqrt{2}}I_1 \sin\delta_1 \sin\delta_2 \\ &\quad + \frac{1}{2\sqrt{2}}I_3 \cos\delta_1 \sin\delta_2 - \frac{1}{4\sqrt{2}}I_1 \cos\delta_1 \cos\delta_2 \end{aligned} \tag{4.7}$$

where

$$\sin\delta_1 = \sin\left(\sin\left(A_1\omega_1 t\right)\right) = 2\sum_{j=1} J_{2j-1}(A_1)\sin\left(2j-1\right)(\omega_1 t) \tag{4.8a}$$

$$\sin\delta_2 = \sin\left(\sin\left(A_2\omega_1 t\right)\right) = 2\sum_{j=1} J_{2j-1}(A_2)\sin\left(2j-1\right)(\omega_2 t) \tag{4.8b}$$

$$\cos\delta_1 = \cos\left(\sin\left(A_1\omega_1 t\right)\right) = J_0(A_1) + 2\sum_{j=1} J_{2j}(A_1)\sin 2j(\omega_1 t) \tag{4.8c}$$

$$\cos\delta_2 = \cos\left(\sin\left(A_2\omega_2 t\right)\right) = J_0(A_2) + 2\sum_{j=1} J_{2j}(A_2)\sin 2j(\omega_2 t). \tag{4.8d}$$

The installation of these Bessel functions found in Equation 4.8 is the source of the ability to determine the values of the Stokes parameters directly by demodulating the detector at specific frequencies, but the important thing is the J_0(A) component. In the case that $J_0(A) = 0$, for which A = 2.4048, this has no effect upon the I_{dc} component, but in the case where it is not correctly set to this value there arises a complex sinusoidal variation in the DC signal when the input polarization state is varied as a result of J_0(A) not being equal to zero. As a test of this, an experiment was performed wherein the Babinet-Soleil compensator is rotated in 5° increments from 0° to 90° in front of a polarizer set at 0°.

As can be noted in Figure 4.4, there is indeed a variation in the I_{dc} following a sinusoidal pattern upon the application of varying input Stokes parameters exclusively as a result of the amplitudes of the two PEMs being incorrectly set. Since this effect is a result of the incorrect amplitude settings of these PEMs, a fitting routine capable of determining the correct amplitudes was readily available. The simple experiment shown in Figure 4.4 was simply repeated at various front-panel settings for the amplitude of each PEM and then fit to a sine function. From this sine function, a percent variation can be accurately determined and the minimization of this variation of I_{dc} will occur at the correct values for the amplitudes.

The inverted error map can be seen in Figure 4.5 (top). The data was inverted in order to be able to accurately model the shape of the error surface by a two dimensional Gaussian

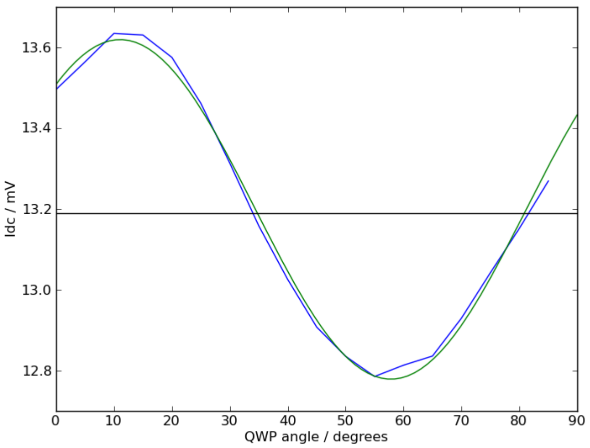

Figure 4.4: An example of the variation of I$_{dc}$ with the variation of the input Stokes parameters as a result of incorrectly set amplitudes for the two modulators. In this case, they were set to A$_0$ = 2.24 and A$_1$ = 2.30. The actual variation is present as the blue trace, while a fit to a sine function is shown in green. A solid black horizontal line shows the mean I$_{dc}$ value, which is predicted to be the constant value for which both modulators are set to an amplitude of 2.4048 radians.

function for the purposes of extracting the optimal retardation amplitude settings for the two PEMs.

$$\Delta I_{\mathrm{dc}} = A \exp\left(-\frac{(A_0 - A_{0,\mathrm{optimal}})^2}{2\sigma_{A_0}} + \frac{(A_1 - A_{1,\mathrm{optimal}})^2}{2\sigma_{A_1}}\right) \tag{4.9}$$

From the fits to Equation 4.9, shown in Figure 4.5 (bottom), it was readily determined that an actual retardation amplitude of 2.4048 was to be achieved at a front panel retardation setting for the 60 kHz PEM of 2.4882 rad and 2.4806 rad for the 50 kHz PEM. From this point on, the system should be fully calibrated and ready to perform, and is graphically described in Figure 4.1.

4.5 Stokes Vector Ellipsometry

With the azimuths and PEM retardation amplitudes effectively calibrated, it is possible to determine the Stokes parameters from a reflected sample, provided a proportionality

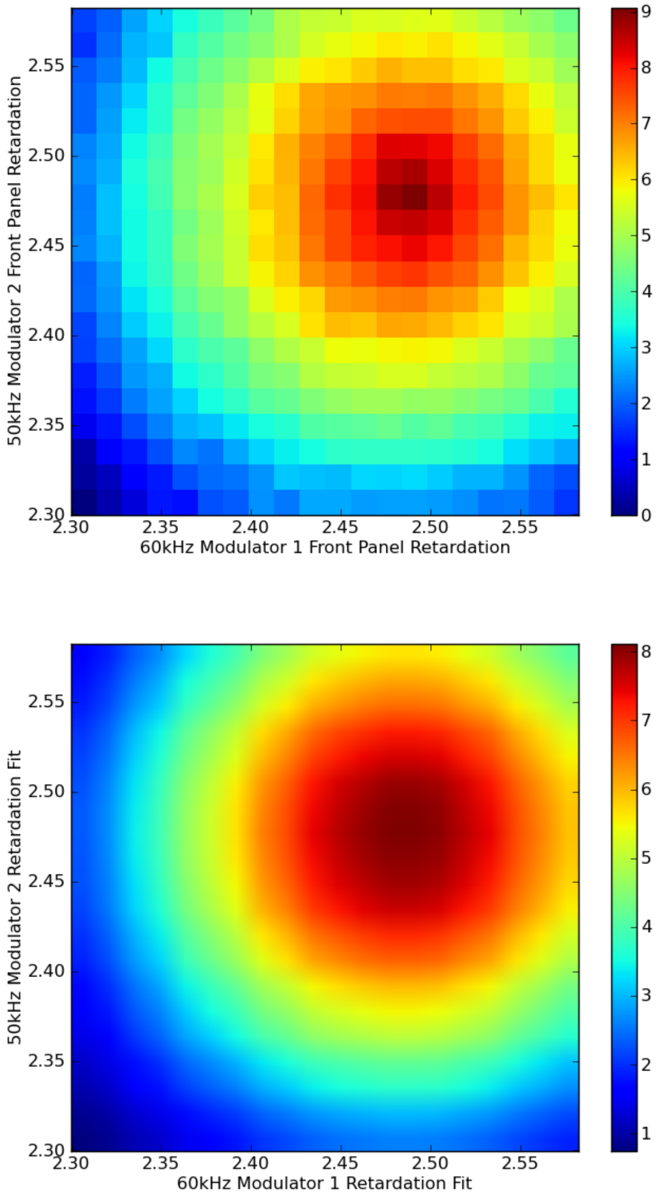

Figure 4.5: Top: Map of the percent variations of the I_{dc} signals experienced as a result of the variation of the input Stokes parameters due at various settings of the front-panel retardation amplitudes for the two PEMs. This map has been inverted in order to be more closely modeled by a 2-dimensional Gaussian function in order to extract the optimal settings for the amplitudes. Regions of high intensity (red) describe the basin for which the variation was at its lowest. Bottom: Fit of the data represented in figure 4.5 to Equation 4.9. This two-dimensional Gaussian fit clearly shows a single maximum, corresponding to the optimal front panel settings of the 60 kHz and 50 kHz photoelastic modulators of 2.4882 and 2.4806 rad respectively.

between the intensities detected at the previously mentioned frequencies and the actual Stokes parameters can be determined.

We begin by setting the azimuth of the first PEM to $0°$, the second PEM to $45°$, and the analyzer to $22.5°$ then it has been demonstrated that the light reaching the detector has a time-dependance according to

$$I(t) = I_0 + I_1 \cos 2\omega_1 t + I_2 \cos 2\omega_2 t + I_3 \cos \omega_1 t \tag{4.10}$$

where $\omega_1/(2\pi) = 60$ kHz and $\omega_2/(2\pi) = 50$ kHz, provided the retardation amplitudes of the two photoelastic modulators have been set to 2.4048 rad.

From Equation 4.10 we see that we acquire four signals $I_i (i = 0..3)$ that are proportional to the four desired elements of the Stokes vector S_i. In theory, the constants of proportionality k_i

$$S_i = k_i I_i \tag{4.11}$$

may be evaluated directly from the fourier coefficients in (4.10). In practice, this is best obtained by calibration [122,124] since instrument parameters such as impedance matching between different lock-in amplifiers may then be included in the k_i values.

In our case, a further improvement of the calibration is realized by rotating the BSC in small steps from 0° to 90° for four different settings of the initial polarizer: $P = 0°, 45°, 90°$ and $135°$. The first step is to normalize all intensities according to $I_i = I_i/I_0$. Then we form a column vector of normalized I_0^2 (ones) with length equal to the number of data points n, irrespective of the polarizer setting.

$$\mathbf{a} = \begin{bmatrix} (I_0^2)_1 \\ (I_0^2)_2 \\ (I_0^2)_3 \\ \vdots \\ (I_0^2)_n \end{bmatrix} = \begin{bmatrix} 1 \\ 1 \\ 1 \\ \vdots \\ 1 \end{bmatrix} \tag{4.12}$$

Here we are working under the assumption that when the PSG is directly inline with the PSA with no sample present, there are no depolarizing elements and therefore

$$S_0 = \sqrt{S_1^2 + S_2^2 + S_3^2} \tag{4.13}$$

becomes

$$I_0^2 = k_1^2 I_1^2 + k_2^2 I_2^2 + k_3^2 I_3^2 \tag{4.14}$$

having set $k_0 = 1$. We then form the matrix

$$\mathbf{B} = \begin{bmatrix} (I_1^2)_1 & (I_2^2)_1 & (I_3^2)_1 \\ (I_1^2)_2 & (I_2^2)_2 & (I_3^2)_2 \\ (I_1^2)_3 & (I_2^2)_3 & (I_3^2)_3 \\ \vdots & \vdots & \vdots \\ (I_1^2)_n & (I_2^2)_n & (I_3^2)_n \end{bmatrix}. \tag{4.15}$$

Finally we define a vector containing the squares of the desired coefficients

$$\mathbf{k} = \begin{bmatrix} k_1^2 \\ k_2^2 \\ k_3^2 \end{bmatrix}. \tag{4.16}$$

The relationship in Equation. 4.11 is then expressed as

$$\mathbf{a} = \mathbf{B}\mathbf{k} \tag{4.17}$$

and so the desired coefficients are obtained from

$$\mathbf{k} = \mathbf{B}^{-1}\mathbf{a}. \tag{4.18}$$

Results of the fit are shown in Figure 4.6. We point out that as a result of our choice of polarizer and BSC azimuths used in the PSG, we calibrate over the full range of $-1 < S_i(i = 1..3) < 1$. The linearity of the plots and the proximity of their slopes to unity (solid black lines) is a testament to the quality of the calibration for all ranges of input and output Stokes vectors.

We now possess everything we need to determine the Stokes vector from a reflected sample as a follows.

$$S_0 = k_{dc} I_0 \tag{4.19a}$$

$$S_1 = k_1 I_1 \tag{4.19b}$$

$$S_2 = k_2 I_2 \tag{4.19c}$$

$$S_3 = k_3 I_3 \tag{4.19d}$$

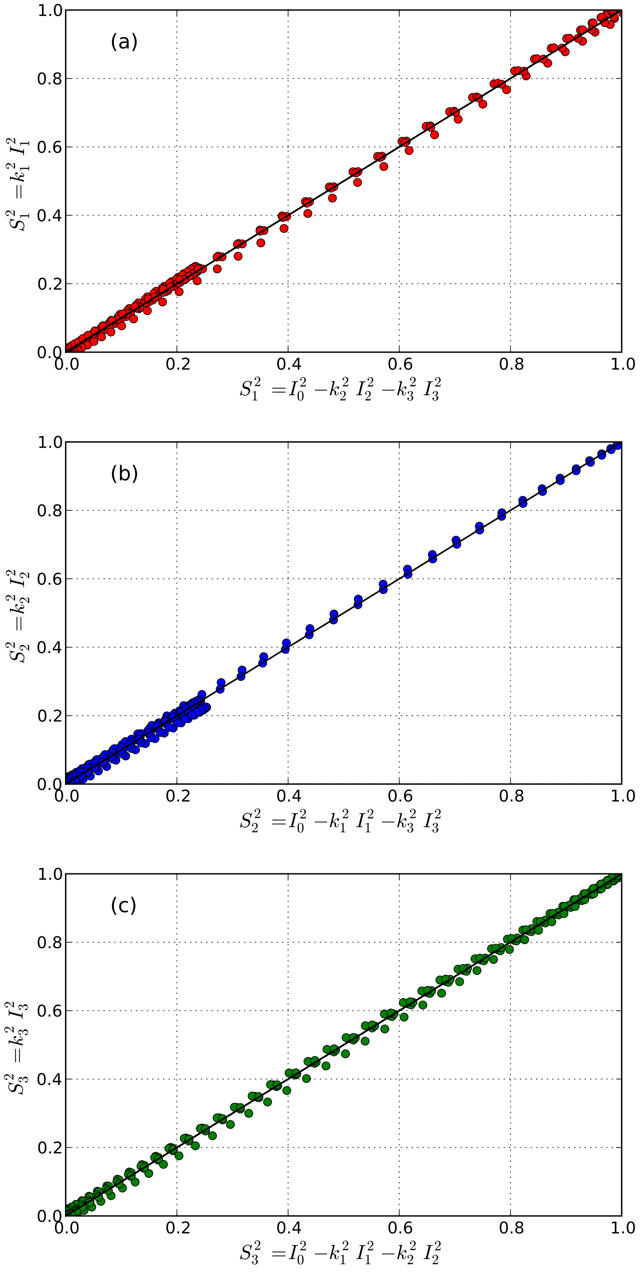

Figure 4.6: Calibration of the instrument response in the absence of depolarization. Assigning $k_0 = 1$ and simultaneously fitting the data from all of the input polarization states resulted in $k_1 = 14.0742$, $k_2 = 11.3868$ and $k_3 = 5.8472$. Linearity of the plots and proximity of the slopes to unity is shown for (a) S_1, (b) S_2 and (c) S_3. Experimental data are plotted as points; the solid line has unit slope.

This expression illustrates that all 4 elements of the Stokes vector are simply encoded as different frequency components of the signal. The output of the photodiode is therefore demodulated using 4 lock-in amplifiers. The S_1 element there comes from the amplitude of the 2nd harmonic of the first PEM, S_2 from the 2nd harmonic of the second PEM, and S_3 from the fundamental of the first PEM. S_0 is measured in the DC component, obtained by demodulating at the chopper frequency, multiplied by k_dc which is equal to 1. Since the highest frequency of interest is 120 kHz, we do not need all of the available bandwidth.

The polarization of any beam is completely described by the 4-element Stokes vector [141]

$$\mathbf{S} = \begin{bmatrix} S_0 \\ S_1 \\ S_2 \\ S_3 \end{bmatrix} = \begin{bmatrix} I_{\text{total}} \\ I_0 - I_{90} \\ I_{+45} - I_{-45} \\ I_{\text{rcp}} - I_{\text{lcp}} \end{bmatrix} \tag{4.20}$$

where S_0 represents the total intensity of the light; S_1 is the excess of horizontally-polarized over vertically-polarized light; S_2 the excess of light polarized at $+45°$ over that at $-45°$; S_3 is the excess of right circular polarization of the two circularly-polarized states. Measurement of the complete Stokes vector also yields the degree of polarization since its elements are related by

$$S_0^2 \leq S_1^2 + S_2^2 + S_3^2 \tag{4.21}$$

where the equality holds in the case of perfectly polarized light.

By measuring the polarization of light that has been transmitted or reflected from proteins adsorbed at the solid-liquid interface, one is able to determine how the polarization has changed from the incident light. This may be traced back to the optical constants of the interface and, ultimately, to the structural features of the interfacial proteins. The instrument described here is based on a polarization modulation from photoelastic modulators, and so is capable of monitoring structural changes that occur on the millisecond timescale.

For many interfaces under investigation, structural information is sufficiently decoded from the polarization of the reflected beam. In general however, interfaces comprised of adsorbed proteins are inhomogeneous, rough, and anisotropic [114–117]. In such cases, more direct characterization is performed by measuring elements of the sample's Mueller matrix, $\mathbf{M}$. The 16 elements of this 4×4 matrix relate the incident and measured output Stokes vectors and may be used to determine the optical and geometric properties of these anisotropic systems [138–140].

$$\mathbf{S}_{\text{out}} = \mathbf{M}\mathbf{S}_{\text{in}} \tag{4.22}$$

For a homogeneous isotropic sample in the absence of any depolarization, the Stokes vector of the reflected light is readily converted into the conventional ellipsometric angles ψ and Δ

$$\tan\psi e^{i\Delta} = \frac{r_p}{r_s} \tag{4.23}$$

if we know the incident light polarization. Maximum sensitivity is achieved when the PSG creates linearly polarized light with $45°$ azimuth. In this case

$$\mathbf{S}_{\text{out}} = \begin{bmatrix} S'_0 \\ S'_1 \\ S'_2 \\ S'_3 \end{bmatrix} = \begin{bmatrix} 1 & -N & 0 & 0 \\ -N & 1 & 0 & 0 \\ 0 & 0 & C & S \\ 0 & 0 & -S & C \end{bmatrix} \begin{bmatrix} 1 \\ 0 \\ 1 \\ 0 \end{bmatrix} = \begin{bmatrix} 1 \\ -N \\ C \\ -S \end{bmatrix}. \tag{4.24}$$

where $N = \cos 2\psi$, $C = \sin 2\psi \cos\Delta$, and $S = \sin 2\psi \sin\Delta$.

Although data reduction in terms of ψ and Δ may be convenient, measuring the complete Stokes vector should be of particular interest to the study of protein adsorption since the resulting surfaces are known to be rough, inhomogeneous, and likely depolarizing as a result. We can evaluate this by examining the extent of the inequality in Equation. 4.21, plotting S_0 against $\sqrt{S_1^2 + S_2^2 + S_3^2}$.

The above calibration procedure could have been carried out with an arbitrary retarder. In our case, however, since we use a BSC set to $\lambda/4$, we have a known PSG. Applying the k values from the above procedure, we are then able to transform the measured I_i into the S_i elements of the input Stokes vectors. This is shown in Figure 4.7 for each setting of the polarizer. These plots demonstrate the quality of our calibration, and clearly show that each element of the input Stokes vector is generated over its full range. They will also provide a means for measuring the full Mueller matrix of any sample, as will be demonstrated later.

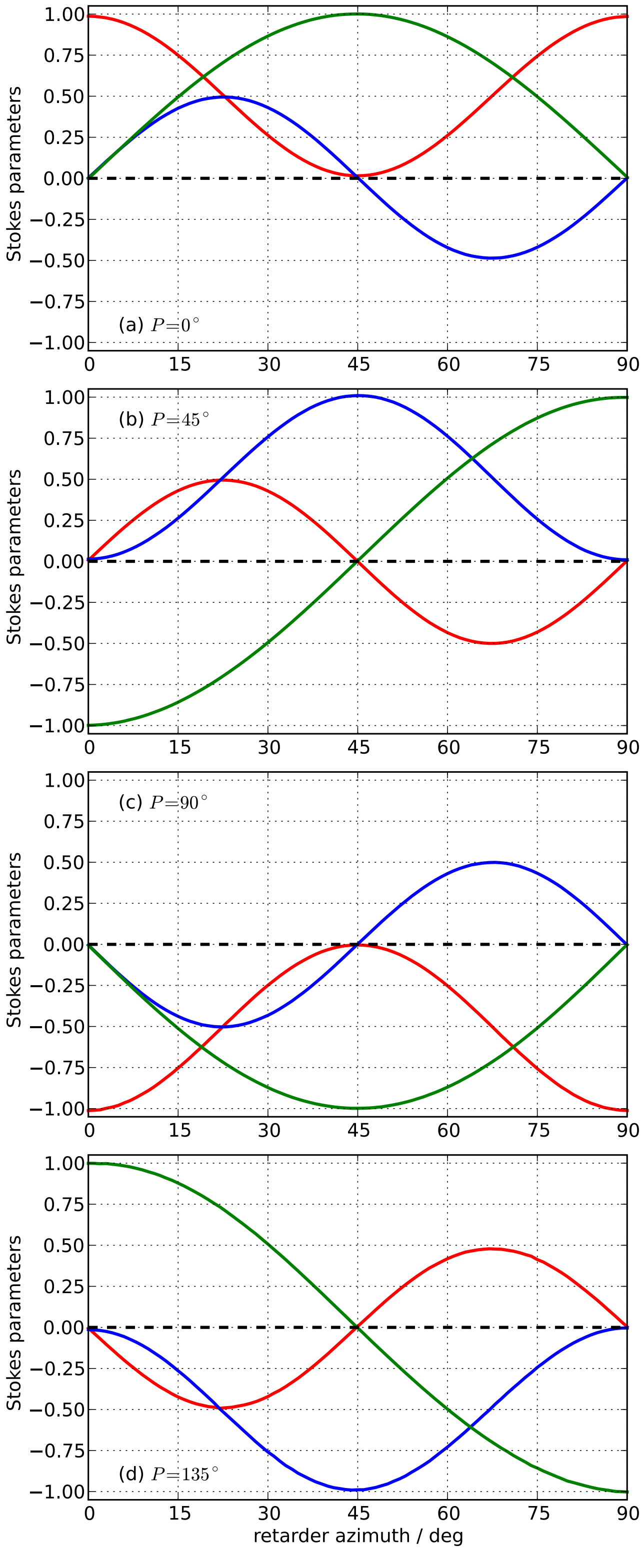

Figure 4.7: Measurement of the normalized input Stokes vectors as a function of the $\lambda/4$ retarder azimuth for four different settings of the polarizer: (a) 0°, (b) 45°, (c) 90°, and (d) 135°. In each case, the S_1 element is shown in red; S_2 in blue; S_3 in green.

	Solution BSA Concentration / mg/mL	Solution Refractive Index	Δ / °
PBS	0.00	1.3330	170.50
Addition 1	2.27	1.3334	170.55
Addition 2	4.17	1.3338	170.60
Addition 3	5.77	1.3341	170.64
Addition 4	7.14	1.3344	170.68

Table 4.1: Variation in refractive index and associated predicted values of Δ based on changing concentrations of BSA for a total internal reflection experiment at 70° for fused silica.

Now that the system is fully calibrated, an experimental example in order to prove the efficiency and accuracy of the system as a functioning high speed Stokes polarimeter is necessary. To this end, a stock solution of 25 mg/mL bovine serum albumin (BSA) in phosphate buffered saline was produced.

At this point, it is necessary to discuss additional optical effect that is predicted to occur during these additions. The changing refractive index of the solution is expected to vary based on the addition of these solutions. In this wavelength region, it is known that the refractive index increment (dn/dc) for BSA solutions is approximately 0.190 mL/mg [220]. In this case, we can predict the variation in the Stokes parameters based on this variation.

Two surfaces were used for adsorption studies, namely naked fused silica and polystyrene coated fused silica. 5 mL of phosphate buffered saline were added to the sample holder first and allowed to reach equilibrium prior to 4 sequential additions of 0.5 mL of the BSA solution, with the results being shown in Figures 4.8 and 4.9.

In the analysis of the adsorption of BSA to fused silica, as shown in Figure 4.8, it is immediately apparent that the Stokes polarimeter is capable of monitoring extremely fast processes. As is noted in Table 4.1, an immediate variation in Δ is expected upon addition of a 0.5 mL aliquot of our BSA solution. Since Δ is determined from the $\cos^{-1}(S_2/S_3)$, we expect to see some variation in one of these Stokes parameters. As can be seen by looking at S_3, graph d in Figure 4.8, we see that at the point of addition, indicated by the vertical

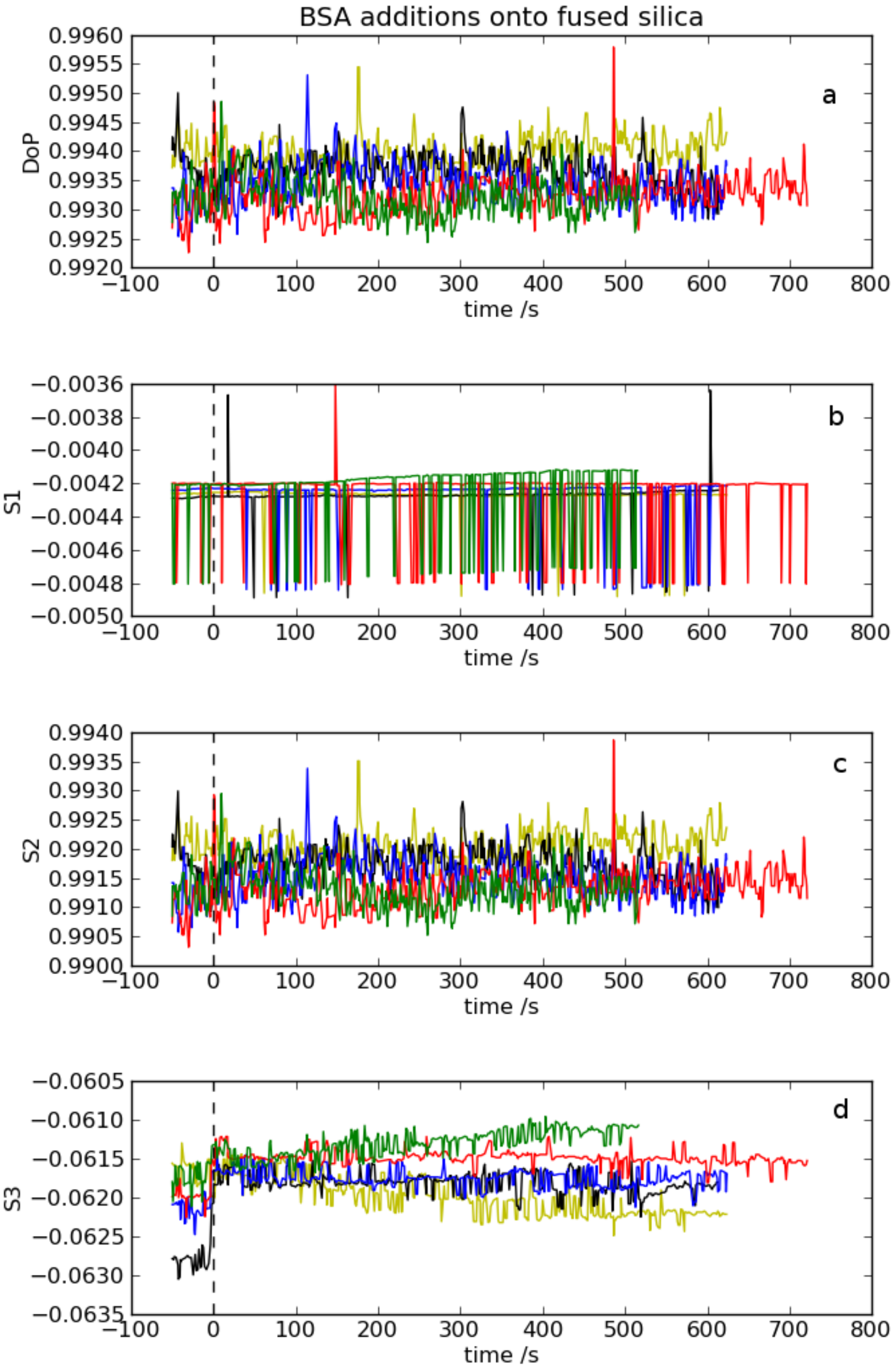

Figure 4.8: Individual Stokes parameters and the overall degree of polarization as a function of time for four consecutive additions of 0.5 mL of 0.5 mg/mL bovine serum albumin in deionized water to naked fused silica. The initial equilibration with PBS is in yellow with the first, second, third, and fourth additions of BSA in black, blue, red and green respectively. The four plots, a,b,c and d describe the overall degree of polarization and the three stokes parameters S_1, S_2, and S_3 respectively.

dashed line, this expected variation occurs. In fact, it occurs for each consecutive addition, as described in order of addition by the black, blue, red, and green traces, albeit with a smaller variation. It is also interesting to note that this initial jump is not instantaneous, but a very quickly increasing curve. This is likely a result of mixing occuring within the sample holder until a uniform concentration is reached in the sample, showing how quickly Stokes parameters can be determined for this system. The overall degree of polarization, along with S_1 and S_2, shown in graphs a, b, and c in Figure 4.8, do not vary considerably over the course of the experiment, but S_3 shows some additional variation after each of the additions, showing a small increase in S_3 through subsequent additions that is unrelated to the change in the refractive index of the solution. This is likely due to the BSA layer adsorbed at the surface growing over time.

The variation in the Stokes parameters for the adsorption of BSA on polystyrene is both more pronounced and more complex than that which was noted in the study of BSA adsorption onto fused silica. The initial increase in S_3, shown in graph d in Figure 4.9, as a result of the changing refractive index of the solution is still noted, but the variation after this point is much greater than for the previous case. What is noted that, in spite of additional aliquots of BSA being added to the system, S_3 undergoes a decrease through the first two additions, shown in the black and blue traces, and a considerable increase through the last two additions, shown in red and green. Another difference between this study and the one done on naked fused silica is evident in the fact that variation occurs in the degree of polarization, S_1, and S_2, shown in graphs a, b and c in Figure 4.9 in addition to the variation in S_3. The variation in S_2 appears to be opposite to that noted for S_3, with the first three additions showing a decrease after the addition of BSA and the final addition resulting in a considerable increase. This is mimicked in the variation of the degree of polarization, as shown in a. The greater variations incurred throughout this experiment are likely due to the increased adsorption of BSA to the polystyrene surface, which is predicted due to the fact that BSA is known to adsorb to similar polymeric surfaces to a greater extent and

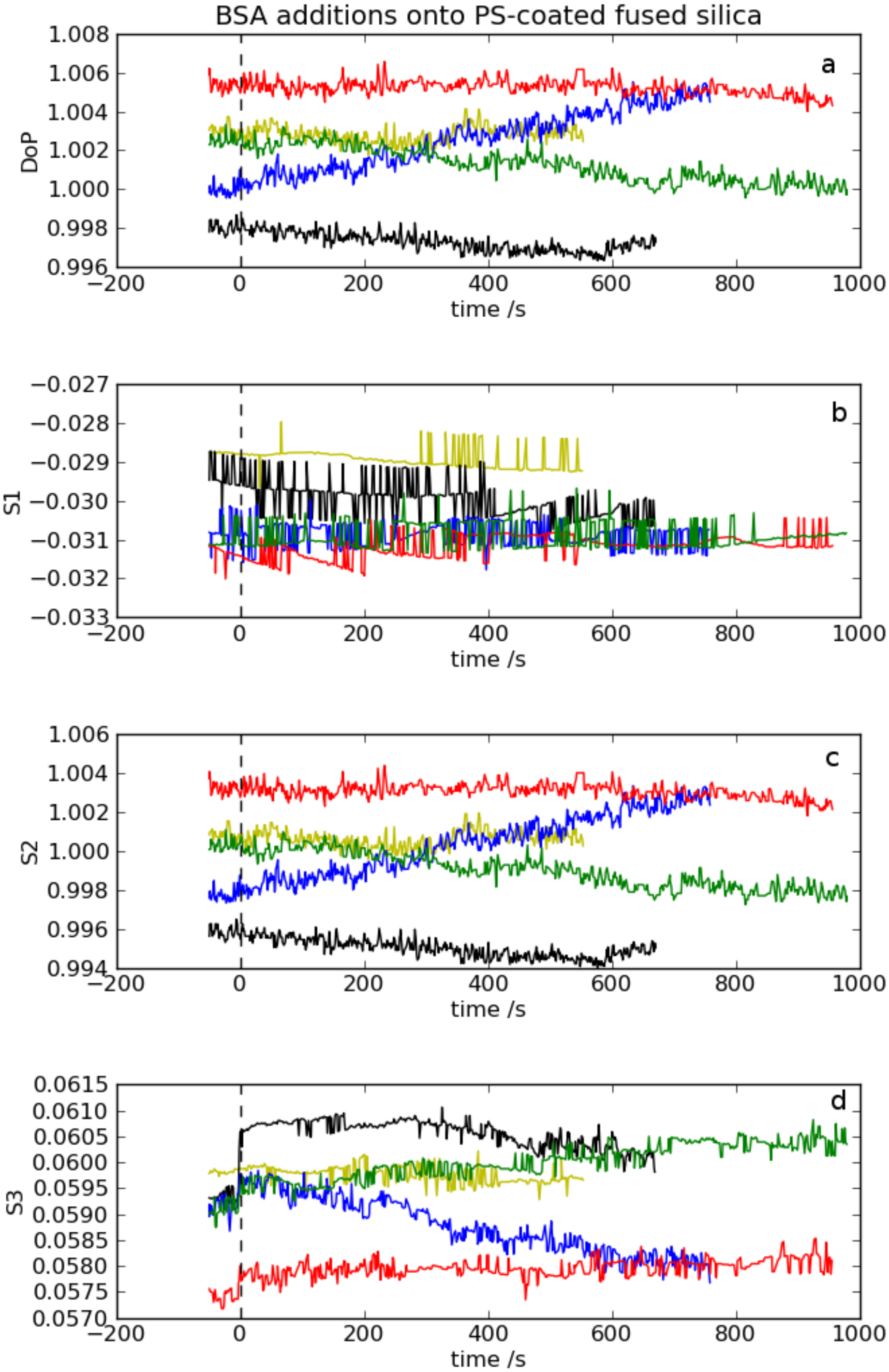

Figure 4.9: Individual Stokes parameters and the overall degree of polarization as a function of time for four consecutive additions of 0.5 mL of 0.5 mg/mL bovine serum albumin in deionized water to naked polystyrene coated fused silica. The initial equilibration with PBS is in yellow with the first, second, third, and fourth additions of BSA in black, blue, red and green respectively. The four plots, a,b,c and d describe the overall degree of polarization and the three stokes parameters S_1, S_2, and S_3 respectively.

faster than to silica [221]. It is also possible that the polymer film is swelling as a result of absorbing water from the solution. The separation of these two effects would be vital for the further interpretation of this varying Stokes parameters.

4.6 Mueller Matrix Ellipsometry

Since our instrument consists of a calibrated PSG in the incident arm, and PSA in the detector arm we are setup to measure all 16 elements of the sample's Mueller matrix. Expanding Equation. 4.22 reveals that for a single polarization state incident on the sample, measurement of the output Stokes vector results in an underdetermined system for $\mathbf{M}$, a system of 4 equations in 16 unknowns

$$\begin{bmatrix} S_0' \\ S_1' \\ S_2' \\ S_3' \end{bmatrix} = \begin{bmatrix} m_{11} & m_{12} & m_{13} & m_{14} \\ m_{21} & m_{22} & m_{23} & m_{24} \\ m_{31} & m_{32} & m_{33} & m_{34} \\ m_{41} & m_{42} & m_{43} & m_{44} \end{bmatrix} \begin{bmatrix} S_0 \\ S_1 \\ S_2 \\ S_3 \end{bmatrix}. \tag{4.25}$$

However, as shown in Figure 4.7, we are capable of generating many input polarization states with our calibrated PSG, so we can easily overdetermine the solution to $\mathbf{M}$. If we designate the calibrated input Stokes vector as $\mathbf{S}$ and the measured output Stokes vector as $\mathbf{S}'$ then we first construct a $n \times 4$ matrix $\mathbf{D}$ containing as many rows n as there are pairs of input-output Stokes vectors used in the determination

$$\mathbf{D} = \begin{bmatrix} (S_0^2)_1 & (S_1^2)_1 & (S_2^2)_1 & (S_3^2)_1 \\ (S_0^2)_2 & (S_1^2)_2 & (S_2^2)_2 & (S_3^2)_2 \\ (S_0^2)_3 & (S_1^2)_3 & (S_2^2)_3 & (S_3^2)_3 \\ \vdots & \vdots & \vdots & \vdots \\ (S_0^2)_n & (S_1^2)_n & (S_2^2)_n & (S_3^2)_n \end{bmatrix}. \tag{4.26}$$

We then use the measured elements of $\mathbf{S}'$ to solve for $\mathbf{M}$ one row at a time, defining a row vector of elements

$$\mathbf{m}_j = \begin{bmatrix} m_{j1} & m_{j2} & m_{j3} & m_{j4} \end{bmatrix} \tag{4.27}$$

where $j = 1..4$ together with a column vector of n measured outputs of the $(j-1)$-th element of $\mathbf{S}'$

$$\mathbf{c_j} = \begin{bmatrix} (S'^2_{j-1})_1 \\ (S'^2_{j-1})_2 \\ (S'^2_{j-1})_3 \\ \vdots \\ (S'^2_{j-1})_n \end{bmatrix}. \tag{4.28}$$

Each row of the solution then proceeds according to

$$\mathbf{m}_j^T = \mathbf{D}^{-1}\mathbf{c}_j. \tag{4.29}$$

The final Mueller matrix is then assembled from the four row vectors

$$\mathbf{M} = \begin{bmatrix} \mathbf{m}_1 \\ \mathbf{m}_2 \\ \mathbf{m}_3 \\ \mathbf{m}_4 \end{bmatrix} = \begin{bmatrix} m_{11} & m_{12} & m_{13} & m_{14} \\ m_{21} & m_{22} & m_{23} & m_{24} \\ m_{31} & m_{32} & m_{33} & m_{34} \\ m_{41} & m_{42} & m_{43} & m_{44} \end{bmatrix}. \tag{4.30}$$

4.6.1 Experimental Determination of Mueller Matrices

As a first demonstration of this procedure, consider the ellipsometer in its straight-through configuration with no sample present. If the data in Figure 4.7 is to be taken as a set of input and output Stokes vectors, then the sample (air) matrix should be the identity matrix. Applying the above scheme results in

$$\mathbf{M}_{\text{air}} = \begin{bmatrix} 1.000 & 0.000 & 0.000 & 0.000 \\ 0.000 & 1.000 & 0.000 & 0.000 \\ 0.000 & 0.000 & 1.000 & 0.000 \\ 0.000 & 0.000 & 0.000 & 1.000 \end{bmatrix} \tag{4.31}$$

with the largest error in a single element less than 0.001. Further tests were conducted, including the acquisition of Mueller matrices for the external reflection from fused silica at 70 degrees, total internal reflection between fused silica and air at 70 degrees and for total internal reflection at the fused silica/phosphate buffered saline solution.

$$\mathbf{M}_{\text{ExtRefFS70}^\circ} = \begin{bmatrix} 1.000 & -0.728 & 0.010 & 0.006 \\ -0.736 & 0.998 & 0.011 & -0.012 \\ 0.005 & -0.002 & 0.6803 & -0.000 \\ 0.006 & 0.014 & 0.003 & 0.711 \end{bmatrix}. \tag{4.32}$$

$$\mathbf{M}_{\mathrm{FS/AirTIR70^\circ}} = \begin{bmatrix} 1.000 & 0.006 & 0.001 & -0.001 \\ -0.003 & 1.028 & 0.037 & 0.095 \\ 0.004 & 0.015 & 0.904 & -0.464 \\ 0.001 & -0.097 & 0.471 & 0.891 \end{bmatrix}. \tag{4.33}$$

$$\mathbf{M}_{\mathrm{FS/PBSTIR70^\circ}} = \begin{bmatrix} 1.000 & 0.007 & 0.002 & 0.007 \\ -0.032 & 1.026 & 0.007 & 0.105 \\ 0.003 & 0.003 & 1.017 & -0.052 \\ 0.001 & -0.101 & -0.056 & 1.006 \end{bmatrix}. \tag{4.34}$$

The external reflection from fused silica had a maximum error of approximately 0.03, while the two totally internally reflecting systems had maximum errors of nearly 0.1.

4.6.2 Polymer Film Thickness from Experimental Mueller Matrices

In order to determine the thickness of the polystyrene film, matrices for external reflections were obtained at incident angles of 66, 68, 70, 72, and 74 degrees. These 5 matrices were fit simultaneously to predicted matrices based on reflection ratios calculated from an equation describing a simple 3 layer model, shown in Equation 4.35.

$$r_{pp,ss} = \frac{r_{1,pp,ss} + r_{2,pp,ss}\mathrm{e}^{-2ib}}{1 + r_{1,pp,ss}r_{2,pp,ss}\mathrm{e}^{-2ib}} \tag{4.35}$$

where

$$b = \frac{2\pi d_f}{\lambda} n_f \cos\theta_f$$

In Equation 4.35, the subscripts 1 or 2 define the two interfaces present, in our case air/polystyrene and polystyrene/fused silica. The index of refraction used for polystyrene at 632.8 nm was 1.58772 [222] and a value of 1.45702 was used for fused silica. λ describes the wavelength used in the experiment, θ_f is the angle with respect to the surface normal that the light is traveling through the film and, most importantly, d_f is thickness of the film.

It is known that the value of b varies periodically, depending upon the angle of at which the light travels through the film and the wavelength of light used in the experiment. As such, it is very difficult to locate global minima and by doing so correctly determine the thickness of the film. The fitting routine used determined the absolute error between the

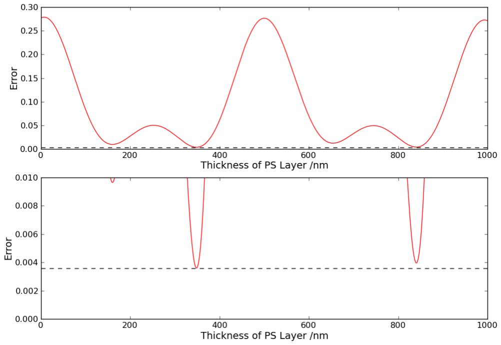

Figure 4.10: Absolute error calculated between experimental Mueller matrices and predicted matrices based on varying thickness of the polystyrene layer. This error is the sum of the errors determined for each set of experimental and predicted matrices at the incident angles of 66°, 68°, 70°, 72°, and 74°. The periodicity of the error as a function of thickness is apparent. One can see though, in the expansion of the lowest error values, that a global minimum does exist for a thickness of 348nm, as shown by the dashed horizontal line.

experimental Mueller matrix and that predicted using Equation 4.35 in the range of 1 nm to 1 μm in steps of 1 nm. The errors as a function of the thickness are shown in Figure 4.10.

It is interesting to use this thickness to generate predicted Mueller matrices for each of the incident angles used in the experiment in order to determine just how sensitive the fitting procedure actually is. This was determined by calculating the N, C, and S parameters of the predicted Mueller matrices, which are determined based on averages of the $-m_{12}$ and $-m_{21}$, m_{34} and $-m_{43}$, and m_{33} and m_{44} elements respectively. These results are shown in Figure 4.11 along with predicted values for 318 nm and 378 nm in order to show the variation of these values with thickness.

The fact that this procedure located the global minimum in error through data obtained at only 5 angles of incidence is quite remarkable, and indicative of the analytical power of Mueller matrix ellipsometry.

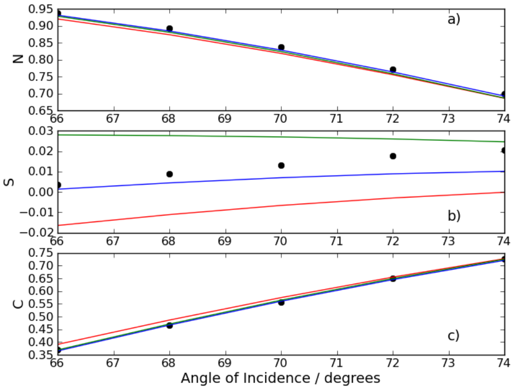

Figure 4.11: Experimental values for N, C, and S, shown as black dots, for the Mueller matrices determined for external reflection from the polystyrene coated film at incident angles of 66°, 68°, 70°, 72°, and 74°. Three predicted trances for each parameter are shown, with the blue line showing the predicted values of N, C, and S for a 348 nm thick polystyrene film on fused silica. The green and red traces show the predicted values based on films of 318 and 378 nm respectively. As can be noted in Figure 4.10, the minimum is quite sharp, and the differences between these three traces only becomes apparent at differences of 30 nm or greater from the optimum thickness.

4.6.3 Mueller Matrices of Adsorbed BSA on Polystyrene and Fused Silica

In order to understand the differences between the adsorption of BSA onto a polystyrene film it was necessary to compare the Mueller matrices of equilibrated systems for which adsorption occurred from solutions of the same concentration. After the fourth aliquot addition, as shown in Figures 4.8 and 4.9, of the BSA solution, the overall concentration was 7.14 mg/mL. Once the systems had reach equilibrium, their matrices were determined as mentioned above, we obtain

$$\mathbf{M}_{\mathrm{FS/BSA}} = \begin{bmatrix} 1.000 & 0.007 & 0.002 & 0.007 \\ -0.004 & 1.020 & 0.006 & 0.100 \\ 0.002 & 0.002 & 1.012 & -0.052 \\ -0.001 & -0.098 & 0.055 & 0.999 \end{bmatrix}. \tag{4.36}$$

$$\mathbf{M}_{\mathrm{PSBSA}} = \begin{bmatrix} 1.000 & 0.039 & -0.003 & 0.003 \\ 0.037 & 1.004 & -0.002 & 0.070 \\ 0.002 & -0.005 & 1.008 & 0.063 \\ 0.002 & -0.074 & -0.063 & 0.993 \end{bmatrix}. \tag{4.37}$$

The form of the above matrix reveals both anisotropy and depolarization. Our interest is to first separate the polarizing from depolarizing contributions. The amount of depolarization may be used as an indicator of the surface roughness. The remaining polarized portion of the Mueller matrix may be quantitatively examined to deduce the optical constants and their anisotropy for the adsorbed BSA molecules. There exists a necessity to develop models capable of differentiating between the layers formed upon the adsorption of BSA and the variation in the refractive index, as well as to take into account optical anisotropy and depolarization. These undertakings will be the focus of future work within the group.

4.7 Discussion

The calibration procedure developed for this system proved to be quite exceptional. Based on minimizing the variation in the dc signal for varying input polarization states through our dual PEM Stokes ellipsometer, it was possible to accurately determine the correct settings for each PEM controller to obtain modulation amplitudes of exactly 2.4048. This new calibration procedure for photoelastic modulators provided us with an extremely well calibrated ellipsometer, capable of detecting very small changes in the optical parameters of a surface at high speeds.

In order to test this, it was decided that a study BSA adsorption to naked and polystyrene coated fused silica should be undertaken. Studies of BSA adsorption to solid surfaces have been undertaken by various methods, specifically ellipsometry [223], total internal fluorescence [224–226], ATR-IR [227] and radio-labeling [221]. Our concentration range is significantly larger than those used for the fluorescence studies, which were typically on the nanomolar range. These studies are interesting, as they show the relatively quick adsorption of the protein to the surface, on the order of a few minutes, and allow for the determination of thermodynamic parameters governing their adsorption. However, at these low concentrations, it is unlikely that the molecules can aggregate and interact with one another, as is likely the case at our approximately 32 to 60 micromolar solutions. What is notable for systems of concentrations closer to ours was that the timescale of experiments was much larger than ours, with equilibration times of hours to days. Our focus was on the study of fast processes, typically those on the order of less than 10 minutes. As can be noted from our experiments in Figures 4.8 and 4.9, there is an instantaneous process, likely a result of the changing refractive index of our solutions as shown in table 4.1, as well as some BSA moving to the surface. This is followed by a slower change that had appeared to have completed within 10 minutes. What can be seen from the 4 traces of S_3 for BSA addition to PS coated fused silica is that after the initial addition (black), the value of S_3 decays, continuing its decay after the second addition (blue) until reaching a minimum value and increasing once more through the third (red) and fourth (green) traces. This is the inverse of the variation in S_2 and the overal degree of polarization, which do not show the instantaneous jump upon the addition of BSA, but increase from the first and second additions and decrease from the third and fourth. The variations in the signal for the naked fused silica are much more simple, existing only appreciably in the S_3 signal, which increases steadily throughout the additions. In a comparison of BSA adsorption at the same concentration to glass and hydrophobic polymer films, it was shown that the overall adsorption process at the polymeric film, in this case PMMA, was faster and resulted in more BSA being adsorbed to the surface [221]. This, it is believed, is the source of the greater variation in the Stokes parameters for the polystyrene coated surfaces.

However, this was only one aspect of our ellipsometer. The determination of Mueller matrices for various samples by our new method involving matrix inversion proved to be quite accurate, readily determining accurate matrices for air, external reflection from fused silica and total internal reflection through fused silica coupled to both air and PBS solution with good agreement with predicted values. In order to show the utility of these determinations, the thickness of the polystyrene film that was coated onto the back of a fused silica prism was determined by fitting Mueller matrices obtained at 5 different angles of incidence, determining the thickness to be 348 nm. The accuracy and sensitivity of this determination was also shown, highlighting the quality of data that can be extracted from accurately determined Mueller matrices.

4.8 Conclusions

The construction of a dual photoelastic modulator based ellipsometer has been completed, along with the development of novel calibration procedures that improve the overall precision of the equipment. The calibration procedure for the accurate determination of the amplitudes of the photoelastic modulators is most interesting, as it removes the necessity for calibration techniques based on demodulating signals at very high frequencies, improving the reliability and precision of the calibration.

Based on this Stokes polarimeter, methods have been developed for the determination of Mueller matrices without great variation of the instrument. Through the comparison of the input unnormalized Stokes parameters and those obtained as output from the experiment, we have shown it is possible to determine the Mueller matrix elements. This is extremely useful as it allowed us to perform both high speed Stokes measurements and to obtain Mueller matrices for equilibrated samples with the same instrument.

In order to determine the accuracy of the machine, the Stokes parameters and Mueller matrices for various samples with known refractive indices and configurations were studied. From the studies based on the external reflection from fused silica and those based in total internal reflection using specially prepared dove-cut 70° prisms of fused silica it was shown that Mueller matrices can be determined with great accuracy.

Chapter 5

Conclusions

5.1 Summary of Work

A major project completed during this work was that of the determination of the surface structure of phenylalanine adsorbed at the polystyrene-solution interface. It was vital to calibrate the SFG system in order to determine an orientation distribution for the adsorbed phenylalanine. This calibration step was vital, as the necessary structural information was encoded in 3 distinct polarization configurations: ppp, ssp, and sps. Based on the inspection of these spectra, it was concluded that the vibrational responses from the phenyl ring were, at least initially, too small to be used and the focus was placed upon the symmetric and antisymmetric stretches of the CH_2 region. In order to determine the orientation distribution, it was necessary to first determine the properties of these vibrations, namely an approximation for their $\alpha^{(2)}$ tensors. This was accomplished by performing ab initio calculations and analysing the results to determine the derivatives of the polarizability and dipole of phenylalanine with respect to each of these normal modes of interest. The relationship between these molecular properties and those of the ensemble, as measured by the sum frequency generation experiments, was quantified in fitting expressions containing the tilt and twist distributions of the plane defined by the CH_2 group on the molecule. A novel fitting routine, capable of locating a global minimum for a highly dimensional parameter space while maintaining efficiency, was developed and the necessary amplitudes, widths, and phases for each of the peaks were extracted from the spectra. Through the comparison of ratios of the amplitudes between different polarization configurations derived from the spectra and predicted ratios based on the ab initio calculations, a set of feasible orientation distributions was obtained.

Based on the orientation distributions determined for phenylalanine adsorbed at a polystyrene surface, a collection of two “families” of tilt and twist distributions were determined to satisfactorily represent the molecules resulting in the acquired spectra. However, based on literature information, it was known that the tilt of the polystyrene ring at the surface with respect to the surface normal was approximately 70°, which was quite complimentary to one of these families, possessing tilts between 80 and 102° degrees. This configuration would provide maximum opportunities for π-π stacking interactions between the phenyl rings, providing an energetic stabilization. Additionally, this would explain the relatively narrow distribution of the phenyl ring tilts of phenylalanine resulting in acceptably small phenyl mode intensities, as noted in the spectra, as these strong interactions would effectively immobilize phenylalanine. Additionally, a rather intense blue-shift was noted for the symmetric and antisymmetric stretches of the CH_2 group were noted, on the order of 12 and 40 cm^{-1} respectively. Based on phenylalanine being immobilized at the surface it was suggested that the proximity of the carboxylate group of one phenylalanine could be interacting with the methylene group of an adjacent phenylalanine, as is known from the literature to cause blue-shifting of alkyl streches. The support from the chemical literature for this structure is considerable, making the case for the methodology used to arrive at this conclusion as being useful for other adsorption studies in which the vibrational modes are well known and assigned.

However, it was noted that the method used in the phenylalanine analysis required a knowledge of the vibrational modes being used for the orientation analysis. For this reason, the modes were also required to not be heavily convoluted with other modes of nearby energy. As an example of this problem, sum frequency generation spectra of leucine were acquired adsorbed on a polystyrene surface. From ab initio calculations, it was known that many peaks existed within the CH region of the infrared and Raman spectra for this molecule with their vibrations being highly coupled to one another. In order to discern the structural information of this molecule, molecular dynamics simulations were employed. By studying the adsorption of leucine to a surface of varying hydrophobicities, including one with a contact angle comparable to polystyrene, 5 separate conformations of leucine were discovered at the surface, as defined by two dihedral angles. These 5 conformers were also able to adopt two different configurations: standing and laying. Ab initio calculations, were performed and predicted sum frequency generation spectra were calculated for each of these conformers in both standing and laying conformations. In order to fit the spectra, a fitting routine was developed that factored in the relative populations of each of these species by calculating an overall $\chi^{(2)}$ by summing contributions of each of the conformers multiplied by their fractional population. The dimensionality of this problem was considerably greater than that of the phenylalanine project and it was determined to be necessary to bias the sizes of certain populations selected to possess the predicted spectra most similar to those acquired. By doing this, a collection of relative orientations providing acceptable fits to the acquired spectra were determined.

Based on these optimum population distributions determined for the fitting of the spectra, it was discovered that with the largest population fractions belonged to two conformers. These structures were defined based on two dihedrals shown in Figure 3.8 with values of (-138,-53) and (-165,83). Both of these conformers were preferrably in their standing orientations. This makes good chemical sense, as it would maximize the hydrophobic interactions between the relatively hydrophobic polystyrene surface and the sec-propyl region of leucine that points towards it in the standing orientation. Additionally, both of these conformers direct their charged, polar groups normal to the surface, maximizing their abilities to be hydrated by water molecules. In the case of the most popular conformer, (-138,-53), the area of contact between the sec-propyl region and the surface is greatest allowing it to have greater hydrophobic interactions with the surface.

These effects would result in considerable stabilization of the (-138,-53) conformer, as would be required based on the knowledge that its internal energy is 15.23 kJ/mol greater than the lowest energy conformer, highlighting the remarkable differences between the energetics of solvent phase and interfacial molecules. In the case of the other conformer with appreciable population size, (-165,83), its energy is much closer to the most stable conformer, only 1.84 kJ/mol higher. Its structure is amenable to being stabilized in standing and laying orientations, with at least two methyl groups capable of contacting the surface, as opposed to the entire sec-propyl group for (-138,-53), and its charged groups being pointed in the direction of the solvent. In the laying phase, it does have one distinct methyl group pointing towards the surface as well. Even with this acceptable structure and lower internal energy, the superior capability of the (-138,-53) conformer to create hydrophobic contacts and to have its charged groups hydrated results in it being the one present in the highest proportion. The fact that these two, the structures most capable of forming these two primary stabilizing functions when present at a hydrophobic surface in an aqueous solution suggest that the methodologies used to arrive at these relative populations is sound.

Finally, the design, assembly and calibration of a dual purpose high speed Stokes polarimeter and Mueller matrix ellipsometer was undertaken. The configuration, based on the use of dual photoelastic modulators, was capable of determining Stokes vectors at high speeds, making this system capable of determining adsorption kinetics. Once equilibrium was reached, the design of the polarimeter allowed it to perform as a Mueller matrix ellipsometer with only a slightly different operational procedure, providing us with the optical and physical properties of adsorbed layers necessary to complement our sum frequency generation spectra. However, in order to function in these dual purposes an extremely accurate calibration of the system was required. Aside from the usual azimuthal orientations, precise calibrations of the photoelastic modulators were required. Various literature methods were attempted with little success, precipitating the development of a new, simple, and effective method for the determination of the driving voltages necessary to produce a precise retardation amplitude. Specifically, it was necessary to determine the correct settings of the photoelastic modulators that would provide a retardation amplitude of 2.4048 rad. The calibration method developed for this purposes was based upon the fact that if the ellipsometric configuration was properly calibrated in terms of azimuths and set up as per the usual experiment, it was shown that a variation in the detected dc signal would occur upon the input of varying polarizations states of light only if the modulators themselves were not calibrated correctly. A method for the minimization of this dc variation by locating the correct setting for the photoelastic modulators was developed and shown to be extremely accurate. It was determined that the 50 and 60 kHz PEMs needed to be set to 2.3315 and 2.3322 rad respectively on their individual controllers in order to produce amplitudes of 2.4048 rad. This allowed for the extremely precise and accurate measurement of Stokes parameters. This allowed for the monitoring of the adsorption of bovine serum albumin to both naked and polystyrene coated fused silica surfaces.

In terms of the calculation of Mueller matrices, a new method for their calculation was developed. Based on the acquired, accurate Stokes parameters, it was found that by creating various input states of known polarization, as defined by their Stokes parameters, and comparing them to those that are present after the sample, it was possible to determine the samples Mueller matrix. This was used to determine the Mueller matrices for samples composed of adsorbed bovine serum albumin at either fused silica or polystyrene coated fused silica surfaces. Additionally, the Mueller matrices for the external reflection from the fused silica surfaces at a variety of angles of incidence were determined and, from these matrices, the thickness of the polystyrene film determined to be 348 nm. The design and calibration of this ellipsometric configuration along with the development of methods for the calculation of accurate Stokes parameters and Mueller matrices provides access to a wealth of information for interfacial systems.

5.2 General Conclusions

The study of molecules adsorbed to surfaces is an important and diverse field, with applicability to a wide variety of medical, industrial, and chemical processes. While this is the case, the fundamental properties of molecules and surfaces that define the characteristics of adsorption processes are still not well understood. It has been the intention of the bulk of this work to provide some insight into these processes by developing methods to determine the orientation of molecules adsorbed at surfaces. In the case of the "top down" method developed, as shown through the study of phenylalanine adsorbed to polystyrene in Chapter 2, it has been shown that the structure of a molecule at a surface can be determined fairly directly, provided the vibrational modes used in fitting the orientational distribution to the acquired SFG spectra are well defined. This methodology, while limited by this requirement, is applicable to a wide variety of small molecules whose adsorption to surfaces are of interest to the previously mentioned fields. In order to develop a more general method for determining the structure of molecules at surfaces, molecular dynamics analysis was incorporated. As was shown for leucine adsorbed to polystyrene surfaces it is possible to determine information regarding the surface structure of molecules with highly complex and heavily convoluted SFG spectra, involving a number of overlapping spectral features. This is vitally important as the spectral responses for many large molecules, such as proteins, would have the same types of complex features. However, by selecting appropriate markers for structural conformation at the surface and carefully studying molecular dynamics simulations based on these markers, it is possible to discover stable surface conformers. From these, it is relatively simple to determine their predicted spectral response and by comparing population fractions of these conformations to determine the optimal fit to acquired spectra based on these population ratios. This method shows incredible promise due to its generality and could greatly further the knowledge of the nature of molecules adsorbed to surfaces.

While the two methodologies developed are directly related to the study of molecular orientation at surfaces, there is a necessity for the study of the films of these adsorbates as a whole. These adsorbate layers possess their own unique optical properties that, if left entirely out of an analysis, could lead to different conclusions being reached than if they were taken into account. In order to determine these properties, Stokes polarimetry and Mueller matrix ellipsometry were selected as they, in conjunction, are capable of determining the properties of evolving adsorption processes as well as the characteristics of complex depolarizing and anisotropic systems once they have reached equilibrium. While various configurations for these two optical experiments exist in the literature, we elected to design a new system that would function in both capacities and developed calibration methods to ensure accuracy as well as mathematical methods for determining these parameters with the least amount of variation in the experimental configuration. This ability to rapidly determine these parameters will prove extremely useful in providing complementary information to further studies of adsorbed molecules.

5.3 Suggestions for Future Work Based on These Findings

The methods developed for the determination of surface structural information are based on very current methods, but there are certain emerging methods that could provide some more insight into these studies. Specific to the acquisition of sum frequency generation there exists a difficult, but extremely interesting experiment in which the polarity of bonds can be deteremined. By performing phase sensitive experiments, the absolute phase of the amplitudes of vibrational adsorptions present in the spectra can be determined [228–231] This allows for the determination of absolute bond polarity and significantly improves the robustness of the fitting procedure. As it stands, a symmetric region spanning both positive and negative values is required to be scanned to determine the amplitude. Not only does this slow down the fitting procedure, but it provides only relative amplitude information. Thus, phase sensitive experiments would greatly improve the accuracy and efficiency of fitting the acquired spectra. As an example of the improvements possible by performing this phase sensitive SFG experiment, in the case of the phenylalanine structural analysis, it was not possible to differentiate between the two plausible families of structures, specifically the B and D families shown in Figure 2.13. It was necessary to use arguments based on the chemical literature to select the B family as the most likely orientation, but with a phase sensitive measurement this would be unnecessary. The structures present in the B and D families are related in terms of their tilt and twist values wherein B has a tilt and twist value of θ and ψ and D has a corresponding structure for $(180° - \theta)$ and $(\psi + 180°)$. Since a phase sensitive measurement would be able to determine the exact phase of the amplitude of the peaks present in our SFG spectra, it would be possible to determine which of these two tilt and twist distributions provided the best fit and allow for the selection of a single orientation distribution as a solution. Obviously, this is not only an important experiment for reducing the complexity of fitting routines but for the accurate description of orientation distributions.

From the calculational side of the work performed, three modifications could be made in the future. While performing the normal mode calculations through ab initio methods, a harmonic oscillator approximation has been used throughout this work. If anharmonicity was added into these calculations, it would be possible to determine the position and amplitudes of Fermi resonances, which up to this point have had to be fit based on information obtained from the literature [232, 233]. Additionally, the addition of static hyperpolarizability to these calculations would allow for the prediction of nonresonant contributions to $\chi^{(2)}$ [234]. These predictions would be of great use, as currently the ranges used for fitting the nonresonant contributions are defined based on the regions of minimal intensity noted in the acquires spectra. This is difficult, as the complicated lineshapes of sum frequency spectra are capable of producing flat regions where peaks of appreciable intensity exist. This prediction would also provide a sign for the nonresonant contribution, which is normally determined only by scanning positive and negative values. Once these improvements to ab initio calculations can be applied to systems such as those studied in this work, they will greatly improve the robustness of the fitting routines and provide more appropriate initial parameters for those searches.

Finally, a promising method for the determination of normal modes and their associated intensities exists in the molecular dynamics simulations [179]. This method, while in its infancy, is of incredible promise as through performing simulations with all atoms capable of motion on very small timescales, it is possible to obtain information on the vibrational modes. This time-dependent approach removes the approximation that exists in our current method of the widths of the peaks being Lorentzian in shape. Additionally, this would simplify the fitting as the widths would be removed from the fitting calculations. Essentially, what is provided by these experiments is a predicted spectrum based on the forces acting upon the atoms as they oscillate on these very small timescale. The result is that the spectra possess a prediction of the actual shape of the peaks, removing the necessity to approximate this by a function such as, in our case, a Lorentzian. At the moment, these methods are only being applied to very simple systems, but once they are capable of functioning for more complex systems, such as our model system for leucine dissolved in water, it is hoped that their benefits will be applicable to our structural analyses.

With regards to the ellipsometric experiments, a useful addition would be the implementation of spectroscopic ellipsometry [121, 140, 235–238]. This would require the replacing of the current HeNe laser source with a multiwavelength source. By performing identical experiments at a variety of input wavelengths it is possible to more robustly fit the data to a variety of optical properties. The reason that this is considered to be an appropriate step in improving our current system is based on the complexity of the systems that we are studying. With each added layer present at the surface of interest, each with their own refractive indices, thicknesses and other properties, the extraction of this information in a reliable fashion becomes more and more difficult. With access to redundant data acquired from the same system at a variety of wavelengths the ability to fit for these parameters becomes more manageable, making the introduction of a multiwavelength source to our system a promising future endeavour.

References

[1] Mermut, O.; York, R. L.; Phillips, D. C.; McCrea, K. R.; Ward, R. S.; Somorjai, G. A. *Biointerphases* **2006,** *1,* 5–11.

[2] Dejardin, P., Ed.; *Proteins at Solid-Liquid Interfaces;* Springer: 2006.

[3] Puleo, D. A.; Bizios, R., Eds.; *Biological Interactions on Materials Surfaces;* Springer: 2009.

[4] Sadana, A., Ed.; *Bioseparation of Proteins;* Academic Press: 1998.

[5] Wahlgren, M.; Arnebrant, T. *TIBTECH* **1991,** *9,* 201-208.

[6] Kasemo, B. *Curr. Opin. Solid State Mater. Sci.* **1998,** *3,* 451-459.

[7] Dickinson, E. *Colloids Surf., B.* **1999,** *15,* 161-176.

[8] Roach, P.; Farrar, D.; Perry, C. C. *J. Am. Chem. Soc.* **2006,** *128,* 3939-3945.

[9] Onuchic, J. N.; Luthey-Schulten, Z.; Wolynes, P. G. *Annual Reviews of Physical Chemistry* **1997,** *48,* 545–600.

[10] Dobson, C. M. *Nature* **2003,** *426,* 884–890.

[11] Roach, P.; Farrar, D.; Perry, C. C. *J. Am. Chem. Soc.* **2005,** *127,* 8168-8173.

[12] Soderquist, M.; Walton, A. *J. Colloid Interface Sci.* **1980,** *75,* 386-397.

[13] Nakanishi, K.; Sakiyama, T.; Imamura, K. *J. Biosci. Bioeng.* **2001,** *91,* 233–244.

[14] Xu, F.; Nacker, J. C.; Crone, W. C.; Masters, K. S. *Biomaterials* **2008,** *29,* 150-160.

[15] Logothetidis, S. *Diam. Relat. Mater.* **2007,** *16,* 1847-1857.

[16] Pavithra, D.; Doble, M. *Biomed. Mater.* **2008,** *3,* 034003–034016.

[17] Elbert, D. L.; Hubbell, J. A. *Annu. Rev. Mater. Sci.* **1996,** *26,* 365–394.

[18] Advances in Polymer Sciences 79. In ; Andrade, J. D.; Hlady, V., Eds.; Springer-Verlag: 1986; Chapter Protein Adsorption and Materials Biocompatibility: A Tutorial Review and Suggested Hypotheses, pages 3–63.

[19] Tan, J. S.; Martic, P. A. *J. Coll. Interfac. Sci.* **1990,** *136,* 415–431.

[20] Satulovsky, J.; Carignano, M. A.; Szleifer, I. *PNAS* **2000,** *97,* 9037–9041.

[21] Szleifer, I. *Biophys. J.* **1997,** *72,* 595–612.

[22] Lu, J. R.; Zhao, X.; Yaseen, M. *Curr. Opin. Coll. Inter. Sci.* **2007,** *12,* 9–16.

[23] Chena, H.; Yuana, L.; Song, W.; Wub, Z.; Lia, D. *Prog. Poly. Sci.* **2008,** *33,* 1059–1087.

[24] Zhang, L.; Sun, Y. *Biochem. Eng. J.* **2010,** *48,* 408–415.

[25] Krishnan, S.; Weinman, C. J.; Ober, C. K. *J. Mater. Chem.* **2008,** *18,* 3405–3413.

[26] Green, R.; Frazier, R.; Shakesheff, K.; Davies, M. C.; Roberts, C.; Tendler, S. *Biomater.* **2000,** *21,* 1823-1835.

[27] Arakawa, T.; Tsumoto, K.; Kita, Y.; Chang, B.; Ejima, D. *Amino Acids* **2007,** *33,* 587-605.

[28] Leonard, M. *J. Chromatog. B.* **1997,** *699,* 3–27.

[29] Ghosh, R. *J. Chromatog. A.* **2002,** *952,* 13–27.

[30] Lee, A. G. *Biochem. Biophys. Acta* **2003,** *1612,* 1–40.

[31] Fusetani, N. *Nat. Prod. Rep.* **2004,** *21,* 94-104.

[32] Miyata, T.; Uragami, T.; Nakamae, K. *Adv. Drug Delivery Rev.* **2002,** *54,* 79-98.

[33] Adhikari, B.; Majumdar, S. *Prog. Polym. Sci.* **2004,** *29,* 699-766.

[34] Jin, W.; Brennan, J. *Anal. Chim. Acta* **2002,** *461,* 1-36.

[35] Zentner, G.; Rathi, R.; Shih, C.; McRea, J.; Seo, M.; Oh, H.; Rhee, B.; Mestecky, J.; Moldoveanu, Z.; Morgan, M.; Weitman, S. *J. Controlled Release* **2001,** *72,* 203-215.

[36] van Butsele, K.; Jerome, R. *Polymer* **2007,** *48,* 7431-7443.

[37] Jain, A.; Jain, S. *Crit. Rev. Ther. Drug Carrier Syst.* **2008,** *5,* 403-447.

[38] Rusmini, F.; Zhong, Z.; Feijen, J. *Biomacromolecules* **2007,** *8,* 1775–1789.

[39] Malmsten, M.; Veide, A. *J. Coll. Int. Sci.* **1996,** *178,* 160-167.

[40] Kyte, J.; Doolittle, R. F. *J. Mol. Biol.* **1982,** *157,* 105–132.

[41] Bachmann, M.; Janke, W. *Phys. Rev. E.* **2006,** *73,* 020901-1–020901-4.

[42] Long, J. R.; Oyler, N.; Drobny, G. P.; Stayton, P. S. *J. Am. Chem. Soc.* **2002,** *124,* 6297–6303.

[43] York, R. L.; Mermut, O.; Phillips, D. C.; McCrea, K. R.; Ward, R. S.; Somorjai, G. A. *J. Phys. Chem. C* **2007,** *111,* 8866–8871.

[44] Horinek, D.; Serr, A.; Geisler, M.; Pirzer, T.; Slotta, U.; Lud, S.; Garrido, J.; Scheibel, T.; Hugel, T.; Netz, R. *Proc. Nat. Acad. Sci. USA* **2008,** *105,* 2842–2847.

[45] Raut, V. P.; Agashe, M. A.; Stuart, S. J.; Latour, R. A. *Langmuir* **2005,** *21,* 1629–1639.

[46] Song, D.; Forciniti, D. *J. Chem. Phys.* **2001,** *115,* 8089–8100.

[47] Vlasova, N. N.; Golovkova, L. P. *Colloid J.* **2004,** *66,* 657–662.

[48] Hedges, J. I.; Hare, P. E. *Geochim. Cosmochim. Acta* **1987,** *51,* 255-259.

[49] Kavasmaneck, P. R.; Bonner, W. A. *J. Am. Chem. Soc.* **1977,** *99,* 44-50.

[50] Carter, P. W. *Geochim. Cosmochim. Acta* **1978,** *42,* 1239-1242.

[51] Alaeddine, S.; Nygren, H. *Coll. Surf. B* **1996,** *6,* 71–79.

[52] Krohn, J. E.; Tsapatsis, M. *Langmuir* **2006,** *22,* 9350–9356.

[53] Pászti, Z.; Keszthelyi, T.; Hakkel, O.; Guczi, L. *J. Phys. Condens. Matter* **2008,** *20,* 224014.

[54] Thomas, A.; Flavell, W. R.; Chatwin, C.; Kumarasinghe, A.; Rayner, S.; Kirkham, P.; Tsoutsou, D.; Johal, T.; Patel, S. *Surface Science* **2007,** *601,* 3828-3832.

[55] Palit, D.; Moulik, S. P. *J. Colloid Interface Sci.* **2001,** *239,* 20-26.

[56] Wedyan, M.; Preston, M. R. *Environ. Sci. Technol.* **2005,** *39,* 2115-5119.

[57] Lambert, J.-F. *Orig. Life. Evol. Biosph.* **2008,** *38,* 211–242.

[58] Churchill, H.; Tend, H.; Hazen, R. M. *Amer. Mineral.* **2004,** *89,* 1048–1055.

[59] Doulia, D.; Rigas, F.; Gimouhopoulos, C. *J. Chem. Technol. Biotechnol.* **2001,** *76,* 83-89.

[60] Basiuk, V. A.; Gromovoy, T. Y. *Coll. Surf. A* **1996,** *118,* 127–140.

[61] Kusumoto, I. *J. Nutr.* **2001,** *131,* 2552S–2555S.

[62] Bloembergen, N.; Pershan, P. S. *Phys. Rev.* **1962,** *128,* 606–622.

[63] Boyd, R. W. *Nonlinear Optics;* Academic Press: Boston, 1992.

[64] Shen, Y. *IEEE J. Sel. Top. Quan. Elec.* **2000,** *6,* 1375–1379.

[65] Bloembergen, N. *Appl. Phys. B* **1999,** *68,* 289–293.

[66] Franken, P. A.; Hill, A. E.; Peters, C. W.; Weinreich, G. *Phys. Rev. Lett.* **1961,** *7,* 118–120.

[67] Bloembergen, N. *Optica Acta* **1966,** *13,* 311–322.

[68] Chang, R. K.; Ducuing, J.; Bloembergen, N. *Phys. Rev. Lett.* **1965,** *15,* 6–8.

[69] Lee, C. H.; Chang, R. K.; Bloembergen, N. *Phys. Rev. Lett.* **1967,** *18,* 167–170.

[70] Lambert, A. G.; Davies, P. B.; Neivandt, D. J. *Appl. Spectrosc. Rev.* **2005,** *40,* 103–145.

[71] Bain, C. D. *J. Chem. Soc. Faraday Trans.* **1995,** *91,* 1281–1296.

[72] Morita, A.; Ishiyama, T. *Phys. Chem. Chem. Phys.* **2008,** *10,* 5801–5816.

[73] Yamada, S.; Lee, I. S. *Anal. Sci.* **1998,** *14,* 1045–1051.

[74] Salafsky, J. S. *Phys. Chem. Chem. Phys.* **2007,** *9,* 5704–5711.

[75] Zhang, W.-K.; Wang, H.-F.; Zheng, D.-S. *Phys. Chem. Chem. Phys.* **2006,** *8,* 4041–4052.

[76] Hicks, J. M.; Petralli-Mallow, T. *Appl. Phys. B.* **1999,** *68,* 589–593.

[77] Kimura-Suda, H.; Sassa, T.; Wada, T.; Sasabe, H. *J. Phys. Chem. B* **2001,** *105,* 1763–1769.

[78] Buck, M.; Eisert, F.; Grunze, M.; Trager, F. *Appl. Phys. A.* **1995,** *60,* 1–12.

[79] Schwarzberg, E.; Berkovic, G.; Marowsky, G. *Appl. Phys. A* **1994,** *59,* 631–637.

[80] Watry, M. R.; Richmond, G. L. *J. Phys. Chem. B* **2002,** *106,* 12517–12523.

[81] Ji, N.; Shen, Y.-R. *J. Am. Chem. Soc.* **2004,** *126,* 15008–15009.

[82] Ji, N.; Shen, Y.-R. *J. Chem. Phys.* **2004,** *120,* 7107–7112.

[83] Mermut, O.; Phillips, D. C.; York, R. L.; mcCrea, K. R.; robert S. Ward,; Somorgai, G. A. *J. Am. Chem. Soc.* **2006,** *128,* 3598.

[84] Phillips, D. C.; York, R. L.; Mermut, O.; r. McCrea, K.; Ward, R. S.; Somorjai, G. A. *J. Phys. Chem. C* **2007,** *111,* 255-261.

[85] York, R. L.; Browne, W. K.; Geissler, P. L.; Somorjai, G. A. *Isr. J. Chem.* **2007,** *47,* 51-58.

[86] Wang, J.; Chen, X.; Clarke, M.; Chen, Z. *Proc. Nat. Acad. Sci. USA* **2005,** *102,* 4978–4983.

[87] Wang, J.; Even, M. A.; Chen, X.; Chmaier, A. H.; Waite, J. H.; Chen, Z. *J. Am. Chem. Soc.* **2003,** *125,* 9914-9915.

[88] Wang, J.; Buck, S. M.; Even, M. A.; Chen, Z. *J. Am. Chem. Soc.* **2002,** *124,* 13302–13305.

[89] Wang, J.; Chen, X.; Clarke, M. L.; Chen, Z. *J. Phys. Chem. B* **2006,** *110,* 5017–5024.

[90] Wang, J.; Clarke, M. L.; Zhang, Y.; Chen, X.; Chen, Z. *Langmuir* **2003,** *19,* 7862–7866.

[91] Wang, J.; Buck, S.; Chen, Z. *J. Phys. Chem. B* **2002,** *106,* 11666–11672.

[92] Wang, J.; Paszti, Z.; Even, M. A.; Chen, Z. *J. Am. Chem. Soc.* **2002,** *124,* 7016–7023.

[93] Wei, X.; Hong, S.-C.; Zhuang, X.; Goto, T.; Shen, Y. R. *Phys. Rev. E* **2000,** *62,* 5160–5172.

[94] Gan, W.; Wu, D.; Zhang, Z.; Feng, R.-R.; Wang, H.-F. *J. Chem. Phys.* **2006,** *124,* 114705.

[95] Lu, R.; Gan, W.; Wu, B.; Chen, H.; Wang, H. *J. Phys. Chem. B* **2004,** *108,* 7297–7306.

[96] Schrodle, S.; Richmond, G. L. *J. Phys. D: Appl. Phys.* **2008,** *41,* 03301–03319.

[97] Vogel, V.; Shen, Y. R. *Ann. Rev. Mater. Sci.* **1991,** *21,* 515–534.

[98] Chen, X.; Chen, Z. *Biochim. Biophys. Acta* **2996,** *1758,* 1257–1273.

[99] Zhuang, X.; Miranda, P. B.; Kim, D.; Shen, Y. R. *Phys. Rev. B* **1999,** *59,* 12632-12640.

[100] Briggman, K. A.; Stephenson, J. C.; Wallace, W. E.; Richter, L. J. *J. Phys. Chem. B* **2001,** *105,* 2785–2791.

[101] Wilson, P. T.; Richter, L. J.; Wallace, W. E.; Briggman, K. A.; Stephenson, J. C. *Chem. Phys. Lett.* **2002,** *363,* 161–168.

[102] Jellison, G. E. *Thin Solid Films* **2004,** *450,* 42–50.

[103] Ossikovski, R.; Anastasiadou, M.; Hatit, S. B.; Garcia-Caurel, E.; Martino, A. D. *Physica Status Solidi* **2008,** *205,* 720-727.

[104] Williams, M. W. *Appl. Opt.* **1986,** *25,* 3616-3622.

[105] Azzam, R. M. A.; Bashara, N. M. *Ellipsometry and Polarized Light;* North-Holland Publishing Company: 1977.

[106] Tompkins, H. G.; Irene, E. A., Eds.; *Handbook of Ellipsometry;* William Andrew: 2005.

[107] Schubert, M. *Annals of Physics* **2006,** *15,* 480-497.

[108] Chen, C.; An, I.; Ferreira, G. M.; Podraza, N. J.; Zapien, J. A.; Collins, R. W. *Thin Solid Films* **2004,** *455,* 14–23.

[109] Goldstein, D. H. *Appl. Opt.* **1992,** *31,* 6676-6683.

[110] Collins, R. W.; Koh, J. *J. Opt. Soc. Am.* **1999,** *16,* 1997-2006.

[111] Hore, D. K.; Natansohn, A.; Rochon, P. *J. Phys. Chem. B* **2002,** *106,* 9004.

[112] Chipman, R. A. *Appl. Opt.* **2005,** *44,* 2490-2495.

[113] Lu, S.-Y.; Chipman, R. A. *Opt. Comm.* **1998,** *146,* 11-14.

[114] Angelsky, O. V.; Tomka, Y. Y.; Ushenko, A. G.; Ushenko, Y. G.; Ushenko, Y. A. *Journal Of Physics D-Applied Physics* **2005,** *38,* 4227–4235.

[115] Guyot, S.; Vezien, C.; Clairac, B.; Fontas, B. *Opt. Appl.* **2004,** *34,* 219–227.

[116] Yaseen, M.; Salacinski, H. J.; Seifalian, A. M.; Lu, J. R. *Biomedical Materials* **2008,** *3,* 034123.

[117] Lousinian, S.; Logothetidis, S. *Thin Solid Films* **2008,** *516,* 8002-8008.

[118] Malmsten, M. *Coll. Surf. B. Bioint.* **1995,** *3,* 297–308.

[119] Malmsten, M. *J. Coll. Int. Sci.* **1994,** *166,* 333–342.

[120] Pokinski, M.; Arwin, H. *Thin Solid Films* **2004,** *455-456,* 716-721.

[121] Lousinian, S.; Logothetidis, S. *Phys. Stat. Sol. C* **2008,** *5,* 1295–1299.

[122] Guan, W.; Jones, G. A.; Liu, Y. W.; Shen, T. H. *J. Appl. Phys.* **2008,** *103,* 043104.

[123] Mackey, J. R.; Salari, E.; Tin, P. *Optical Engineering* **2003,** *42,* 1460–1466.

[124] Liu, Y. W.; Jones, G. A.; Peng, Y.; Shen, T. H. *Journal Of Applied Physics* **2006,** *100,* 063537.

[125] Kuldkepp, M.; Hawkes, N. C.; Rachlew, E.; Schunke, B. *Appl. Opt.* **2005,** *44,* 5899-5904.

[126] Jellison, G.; Modine, F. *Appl. Opt* **1997,** *36,* 8190–8198.

[127] Jellison, G. E.; Modine, F. A. *Appl. Opt.* **1997,** *36,* 8184–8189.

[128] Anderson, R. *Appl. Opt.* **1992,** *31,* 11–13.

[129] Benecke, C.; Seiberle, H.; Schadt, M. *Japan. J. Appl. Phys.* **2000,** *39,* 525-531.

[130] Hilfiker, J. N.; c. M. Herzinger,; Wagner, T.; Marino, A.; Delgais, G.; Abbate, G. *Thin Solid Films* **2004,** *466-456,* 591-595.

[131] Poksinski, M.; Arwin, H. *Optics Letters* **2007,** *32,* 1308-1310.

[132] Hook, F.; Voros, J.; Rodahl, M.; Kurrat, R.; Boni, P.; Ramsden, J. J.; Textor, M.; Spencer, N. D.; Tengvall, P.; Gold, J.; Kasemo, B. *Coll. Surf. B* **2002,** *24,* 155-170.

[133] Seitz, R.; Brings, R.; Geiger, R. *Appl. Surf. Sci.* **2005,** *252,* 154-157.

[134] Gill, K. J. S.; Isaacson, K.; Dew, S.; Kwok, D. Y. Reversible Protein Detection Method Based on Self-Assembled Monolayers Using Ellipsometry. In *Proceedings of the 2004 International Conference on MEMS, NANO and Smart Systems*; 2004.

[135] Elwig, H. *Biomaterials* **1998,** *19,* 397-406.

[136] Arwin, H. *Thin Solid Films* **1998,** *313–314,* 764–774.

[137] Arwin, H.; Poksinski, M.; Johansen, K. *Appl. Opt.* **2004,** *43,* 3028-3036.

[138] Jellison, G. E. *Thin Solid Films* **1998,** *313,* 33–39.

[139] De Martino, A.; Garcia-Caurel, E.; Laude, B.; Drevillon, B. *Thin Solid Films* **2004,** *455,* 112–119.

[140] Laskarakis, A.; Logothetidis, S.; Pavlopoulou, E.; Gioti, M. *Thin Solid Films* **2004,** *455-456,* 43-49.

[141] Humliček, J. Handbook of Ellipsometry. In ; Tompkins, H. G.; Irene, E. A., Eds.; Springer Science & Business: 2005; Chapter Polarized Light and Ellipsometry, pages 3–93.

[142] Togashi, D. M.; Ryder, A. G.; Heiss, G. *Colloids Surf., B* **2009,** *72,* 219-229.

[143] Lassen, B.; Malmsten, M. *J. Coll. Int. Sci.* **1996,** *179,* 470–477.

[144] Hook, F.; Kasemo, B. *Chem. Sens. Biosens.* **2006,** *5,* 1.

[145] Bieri, M.; Bürgi, T. *Phys. Chem. Chem. Phys.* **2006,** *8,* 513–520.

[146] Brosseau, C. L.; Roscoe, S. G. *Electrochim. Acta* **2006,** *51,* 2145-2152.

[147] Nabok, A. V.; A., T.; Holloway, A.; Staroub, N. F.; Gojster, O. *Biosen. Bioelec.* **2007,** *22,* 885–890.

[148] York, R. L.; Holinga, G. J.; Somorjai, G. A. *Langmuir* **2009,** *25,* 9369–9374.

[149] Mao, Y.; Wi, W.; Peng, H.; Zhang, J. *J. Biotech.* **2001,** *89,* 1–10.

[150] Bieri, M.; Burgi, T. *J. Phys. Chem. B.* **2005,** *109,* 22476–22485.

[151] Chittur, K. K. *Biomaterials* **1998,** *19,* 357-369.

[152] Hind, A. R.; Bhargava, S. K.; McKinnon, A. *Adv. Coll. Inter. Sci.* **2001,** *93,* 91–114.

[153] Imamura, K.; Kawasaki, Y.; Awadzu, T.; Sakiyama, T.; Nakanishi, K. *J. Colloid. Int. Sci.* **2003,** *267,* 294–301.

[154] Herne, T. M.; Ahern, A. M.; Garrell, R. L. *Anal. Chim. Acta.* **1991,** *246,* 75–84.

[155] Das, G.; Mecarini, F.; Gentile, F.; De Angelis, F.; Kumar, M.; Patrizio, C.; Liberale, C.; Cuda, G.; Di Fabrizio, E. *Biosens. Bioelectron.* **2009,** *24,* 1693–1699.

[156] Han, X. X.; Huang, G. G.; Zhao, B.; Ozaki, Y. *Anal. Chem.* **2009,** *81,* 3329–3333.

[157] Iosin, M.; Toderas, F.; Baldeck, P. L.; Astilean, S. *J. Mol. Struc.* **2009,** *924-926,* 196–200.

[158] Pellenc, D.; Bennett, R. A.; Green, R. J.; Sperrin, M.; Mulheran, P. A. *Langmuir* **2008,** *24,* 6949-6955.

[159] Teschke, O.; de Souza, E. F. *Chem. Phys. Lett.* **2003,** *375,* 540–546.

[160] Teschke, O.; de Souza, E. F. *Langmuir* **2003,** *19,* 5357–5365.

[161] Tellier, C. R.; Benmessaouda, D. *J. Mat. Sci.* **1994,** *29,* 3281–32394.

[162] Piao, L.; Liu, Q.; Li, Y.; Wang, C. *J. Phys. Chem. C* **2008,** *112,* 2857-2863.

[163] Pawlukojc, A.; Leciejewicz, J.; Ramirez-Cuesta, A. J.; J., N.-S. *Spectrochim. Acta* **2005,** *61,* 2474–2481.

[164] Ghosal, S.; Hemminger, J. C.; Bluhm, H.; Mun, B. S.; Hebenstreit, E. L. D.; Jetteler, G.; Ogletree, D. F.; Requejo, F. G.; Salmeron, M. *Science* **2005,** *307,* 563–566.

[165] Baas, T.; Gamble, L.; Hauch, K. D.; Castner, D. G.; Sasaki, T. *Langmuir* **2002,** *18,* 4898–4902.

[166] Weidner, T.; Samuel, N. T.; McCrea, K.; Gamble, L. J.; Ward, R. S.; Castner, D. G. *Am. Vac. Soc.* **2010,** *5,* 9–16.

[167] van der Heiden, A. P.; Willems, G. M.; Lindhout, T.; Pijpers, A. P.; Koole, L. H. *J. Biomed. Mater. Res.* **1998,** *40,* 195–203.

[168] Thomas, R. K. *Progr. Colloid. Polym. Sci.* **1997,** *103,* 216–225.

[169] Harding, J. H.; Duffy, D. M. *J. Mat. Chem.* **2006,** *16,* 1105-1115.

[170] Kuo, I-Feng, W.; Mundy, Christopher, J. *Science* **2004,** *303,* 658–660.

[171] Car, R.; Parrinello, M. *Phys. Rev. Lett.* **1985,** *55,* 2471-2474.

[172] Kuhne, T. D.; Krack, M.; Mohamed, F. R.; Parrinello, M. *Phys. Rev. Lett.* **2007,** *98,* 066401.

[173] Mulheran, P.; Kubiak, K. *Mol. Sim.* **2009,** *35,* 561-566.

[174] Choi, Y.; Jung, S. *Carb. Res.* **2004,** *339,* 1961–1966.

[175] Aloisi, G.; Foresti, M. L.; Guidelli, R. *J. Chem. Phys.* **1989,** *91,* 5592–5596.

[176] Perry, A.; Neipert, C.; Space, B.; Moore, P. B. *Chem. Rev.* **2006,** *106,* 1234-1258.

[177] Trudeau, T. G.; Hore, D. K. *Langmuir* **2010,** *26,* A–H.

[178] Trudeau, T. G.; Jena, K. C.; Hore, D. K. *J. Phys. Chem. C* **2009,** *113,* 20002–20008.

[179] Morita, A.; Hynes, J. T. *J. Phys. Chem. B* **2002,** *106,* 673–685.

[180] Morita, A. *J. Phys. Chem. B* **2006,** *110,* 3158–3163.

[181] Wu, H.; Zhang, W.; Gan, W.; Cui, Z.; Wang, H. F. *J. Chem. Phys.* **2006,** *125,* 133203–13324.

[182] Hirose, C.; Yamamoto, H.; Akamatsu, N.; Domen, K. *J. Phys. Chem.* **1993,** *97,* 10064–10069.

[183] Hirose, C.; Akamatsu, N.; Domen, K. *J. Chem. Phys.* **1992,** *96,* 997–1004.

[184] Richter, L. J.; Yang, C. S. C.; Wilson, P. T.; Hacker, C. A.; van Zee, R. D.; Stapleton, J. J.; Allara, D. L.; Yao, Y.; Tour, J. M. *J. Phys. Chem. B* **2004,** *108,* 12547–12559.

[185] Hore, D. K.; Beaman, D. K.; Parks, D. H.; Richmond, G. L. *J. Phys. Chem. B* **2005,** *109,* 16846–16851.

[186] Gautam, K. S.; Schwab, A. D.; Dhinojwala, A.; Zhang, D.; Dougal, S. M.; Yeganeh, M. S. *Phys. Rev. Lett.* **2000,** *85,* 3854–3857.

[187] Schmidt, M. W.; Baldridge, K. K.; Boatz, J. A.; Elbert, S. T.; Gordon, M. S.; Jensen, J. H.; Koseki, S.; Matsunaga, N.; Nguyen, K. A.; Su, S.; Windus, T. L.; Dupuis, M.; Jr, J. A. M. *J. Comput. Chem.* **1993,** *14,* 1347-1363.

[188] Long, D. A. *The Raman Effect: A Unified Treatment of The Theory of Raman Scattering by Molecules;* John Wiley & Sons: 2002.

[189] Kleiman, V. D.; Park, H.; Gordon, Robert, J.; Zare, R. N. *Companion to Angular Momentum;* John Wiley & Sons: 1998.

[190] Yang, C. S.-C.; Wilson, P. T.; Richter, L. J. *Macromolecules* **2004,** *37,* 7742-7746.

[191] Jena, K. C.; Hore, D. K. *J. Phys. Chem. C* **2009,** *113,* 15364–15372.

[192] Byrd, R.; Lu, P.; Nocedal, J. *SIAM J. Sci. Stat. Comp* **1995,** *16,* 1190-1208.

[193] Zhu, C.; Byrd, R.; Nocedal, J. *ACM Trans. Math. Software* **1997,** *23,* 550-560.

[194] Linder, R.; Nispeal, M.; Häber, T.; Kleinermanns, K. *Chem. Phys. Lett.* **2005,** *409,* 260–264.

[195] Merrick, J. R.; Moran, D.; Radom, L. *J. Phys. Chem. A* **2007,** *111,* 11683-11700.

[196] Wilson, P. T.; Briggman, K. A.; Wallace, W. E.; Stephenson, J. C.; Richter, L. J. *Appl. Phys. Lett.* **2002,** *80,* 3084–3086.

[197] Yuzawa, T.; Kubota, J.; Onda, K.; Wada, A.; Domen, K.; Hirose, C. *J. Mol. Struct.* **1997,** *413,* 307–312.

[198] Chen, Z.; Shen, Y. R.; Somorjai, G. A. *Annu. Rev. Phys. Chem.* **2002,** *53,* 437–465.

[199] Wei, X.; Hong, S.-C.; Lvovsky, A. I.; Held, H.; Shen, Y. R. *J. Phys. Chem. B* **2000,** *104,* 3349–3354.

[200] Harp, G. P.; Rangwalla, H.; Yeganeh, M. S.; Dhinojwala, A. *J. Am. Chem. Soc.* **2003,** *125,* 11283–11290.

[201] Miyamae, T.; Akiyama, H.; Yoshida, M.; Tamaoki, N. *Macromolecules* **2007,** *40,* 4601–4606.

[202] Chen, C.; Wang, J.; Chen, Z. *Langmuir* **2004,** *20,* 10186–10193.

[203] Kim, J.; Chou, K. C.; Somorjai, G. A. *J. Phys. Chem. B* **2002,** *106,* 9198–9200.

[204] Chou, K. C.; Kim, J.; Baldelli, S.; Somorjai, G. A. *J. Electroanal. Chem.* **2003,** *554–555,* 253–263.

[205] Shin-ya, K.; Takahaski, O.; Katsumoto, Y.; Ohno, K. *J. Mol. Struct.* **2007,** *827,* 155-164.

[206] Scheiner, S. *J. Phys. Chem. B* **2009,** *113,* 10421-10427.

[207] Morita, S.; Fujii, A.; Mikami, N.; Tsuzuki, S. *J. Phys. Chem. A* **2006,** *110,* 10583-10590.

[208] Hall, S. A.; Hickey, A. D.; Hore, D. K. *J. Phys. Chem. C* **2010,** *114,* 9748–9757.

[209] van der Spoel, D.; Lindahl, E.; Hess, B.; Groenhof, G.; Mark, A. E.; Berendsen, H. J. C. *J. Comp. Chem.* **2005,** *26,* 1701–1718.

[210] Berendsen, H. J. C.; Grigera, J. R.; Straatsma, T. P. *J. Phys. Chem.* **1987,** *91,* 6269–6271.

[211] Stecki, J. *Langmuir* **1997,** *13,* 597–598.

[212] Steele, W. A. *J. Phys. Chem.* **1978,** *82,* 817-821.

[213] Hirvi, J. T.; Pakkanen, T. A. *J. Chem. Phys.* **2006,** *125,* 144712.

[214] Kaminski, G. A.; Friesner, R. A. *J. Phys. Chem. B* **2001,** *105,* 6474–6487.

[215] Berendsen, H. J. C.; Postma, J. P. M.; van Gunsteren, W. F.; Dinola, A.; Haak, J. R. *J. Chem. Phys.* **1984,** *81,* 3684–3690.

[216] Lu, J.; Perumal, S.; Hopkinson, I.; Webster, J.; Penfold, J.; Hwang, W.; Zhang, S. *J. Am. Chem. Soc.* **2004,** *126,* 8940–8947.

[217] Read, M.; Mayes, A.; Burkett, S. *Coll. Surf. A* **2004,** *37,* 113–127.

[218] Pavritha, D.; Doble, M. *Biomed. Mater.* **2008,** *3,* 034003-034003+13.

[219] Wang, M. W.; Chao, Y. F.; Leou, K. C.; Tsai, F. H.; Lin, T. L.; Chen, S. S.; Liu, Y. W. *Japan. J. Appl. Phys. 1* **2004,** *43,* 827–832.

[220] Tumolo, T.; Angnes, L.; Baptista, M. S. *Anal. Biochem.* **2004,** *333,* 273–279.

[221] Lee, S. H.; Rickenstein, E. *J. Coll. Int. Sci.* **1988,** *125,* 365–397.

[222] Kasarova, S. N.; Sultanova, N. G.; Ivanov, C. D.; Nikolov, I. D. *Opt. Mater.* **2007,** *29,* 1481–1490.

[223] Azzam, R. M. A.; Rigby, P. G.; Krueger, J. A. *Phys. Med. Biol.* **1977,** *22,* 422–430.

[224] Bekos, E. J.; Ranieri, J. P.; Aebischer, P.; Jr., J. A. G.; Bright, F. V. *Langmuir* **1995,** *11,* 984–989.

[225] Sapsford, K. E.; Ligler, F. S. *Biosens. Bioelectron.* **2004,** *19,* 1045–1055.

[226] Kwok, K. C.; Yeung, K. M.; Cheung, N. H. *Langmuir* **2007,** *23,* 1948–1952.

[227] McClellan, S. J.; Franses, E. I. *Coll. Surf. A* **2005,** *260,* 265-275.

[228] Chen, X.; Hau, W.; Huang, Z.; Allen, H. *J. Am. Chem. Soc.* **2010,** *132,* 11336–11342.

[229] Ham, S.; Hahn, S.; Lee, C.; Kim, T.-K.; Kwak, K.; Cho, M. *J. Phys. Chem. B* **2004,** *108,* 9333–9345.

[230] Ji, N.; Ostroverkhov, V.; C.S.Tian,; Shen, Y. R. *Phys. Rev. Lett.* **2008,** *100,* 096102.

[231] Leute, S.; Lottermoser, T.; Frölich, D. *Opt. Lett.* **1999,** *24,* 1520–1523.

[232] Golonzka, O.; Khalil, M.; Demirdöven, N.; Tokmakoff, A. *J. Chem. Phys.* **2001,** *115,* 10814–10828.

[233] Golonzka, O.; Khalil, M.; Demirdöven, N.; Tokmakov, A. *Phys. Rev. Lett.* **2001,** *86,* 2154–2157.

[234] Chen, W.; Li, Z.-R.; Wu, D.; Gu, F.-L.; Hao, X.-Y.; Wang, B.-Q.; Li, R.-J.; Sun, C.-C. *J. Chem. Phys.* **2004,** *121,* 10489–10494.

[235] Xia, G.-Q.; Zhang, R.-J.; Chen, Y.-L.; Zhao, H.-B.; Wand, S.-Y.; Zhou, S.-M.; Zheng, Y.-X.; Yang, Y.-M.; Chen, L.-Y. *AIP* **2000,** *71,* 2677–2683.

[236] Bang, K. Y.; An, J. S.; An, I.; Collins, R. W. *J. Korean Phys. Soc.* **2004,** *45,* 185–188.

[237] Beyerlein, D.; Kratzmüller, T.; Eichhorn, K.-J. *Vibrational Spectrosc.* **2002,** *29,* 223–227.

[238] Dura, J. A.; Richter, C. A.; Majkrzak, C. F.; Nguyen, N. V. *Appl. Phys. Lett.* **1998,** *73*, 2131–2133.